

A Geometric Tension Dynamics Model of Epithelial Convergent Extension

Nikolas H. Claussen,¹ Fridtjof Brauns,^{2,*} and Boris I. Shraiman^{1,2,†}

¹*Department of Physics, University of California Santa Barbara, Santa Barbara, California 93106, USA*

²*Kavli Institute for Theoretical Physics, University of California Santa Barbara, Santa Barbara, California 93106, USA*

Epithelial tissue elongation by convergent extension is a key motif of animal morphogenesis. On a coarse scale, cell motion resembles laminar fluid flow; yet in contrast to a fluid, epithelial cells adhere to each other and maintain the tissue layer under actively generated internal tension. To resolve this apparent paradox, we formulate a model in which tissue flow in the tension-dominated regime occurs through adiabatic remodeling of force balance in the network of adherens junctions. We propose that the slow dynamics within the manifold of force-balanced configurations is driven by positive feedback on myosin-generated cytoskeletal tension. Shifting force balance within a tension network causes active cell rearrangements (T1 transitions) resulting in net tissue deformation oriented by initial tension anisotropy. Strikingly, we find that the total extent of tissue deformation depends on the initial cellular packing order. T1s degrade this order so that tissue flow is self-limiting. We explain these findings by showing that coordination of T1s depends on coherence in local tension configurations, quantified by a geometric order parameter in tension space. Our model reproduces the salient tissue- and cell-scale features of germ band elongation during *Drosophila* gastrulation, in particular the slowdown of tissue flow after approximately twofold elongation concomitant with a loss of order in tension configurations. This suggests local cell geometry contains morphogenetic information and yields experimentally testable predictions. Furthermore, defining biologically controlled active tension dynamics on the manifold of force-balanced states may provide a general approach to the description of morphogenetic flow.

Significance. Animal development requires large numbers of cells to choreograph their force generation in order to sculpt tissues and organs. Leveraging the fact that cellular forces equilibrate rapidly compared to the speed of development, we formulate a geometrical model for the network of balanced active tensions in an epithelial sheet. Within this framework, we can investigate how cells remodel the tension network to change tissue shape. A simple “winner-takes-all” mechanical feedback loop can self-organize complex cell movement, matching experimental data on the cell and tissue scale. We find that the ability to self-organize depends on initial order in the cellular packing. Our model explains how genetic patterning, embryo geometry, and cellular packing geometry combine to determine tissue shape change.

Shape changes of epithelia during animal development involve major cell rearrangements, often manifested as a “convergent extension” of cell sheets. On the coarse scale, convergent extension looks much like the laminar shear flow of an incompressible fluid in the vicinity of a hyperbolic fixed point (see Fig. 1A). Indeed, previous work has combined hydrodynamic equations for the mesoscale cell velocity field with active stress fields to model morphogenetic tissue flow [1–4]. Yet in contrast to a fluid, epithelia are under internally gener-

ated tension – revealed by laser ablation [5] – and, like solids, maintain their shape against external forces. Tissue flow is achieved through local cell intercalation (T1 neighbor exchange processes, see Fig. 1B) driven by the concerted mechanical activity of individual cells. Cells generate forces via actomyosin contractility in the cortical cytoskeleton at the adherens junctions between cells (Fig. 1C). Moreover, the adherens junctions can remodel through the turnover of its constituent molecules. Taken together, this implies that interfaces in the cell array can change their length and tension independently. This behavior is fundamentally different from (Hookean) springs, where tension and length are related by a constitutive relationship. Instead, one can imagine cellular interfaces as “microscopic muscles” which are controlled by the recruitment and release of myosin motors.

Vertex models generally describe epithelial tissue as a polygonal tiling of cells where the vertex positions are the dynamical variables [6, 7]. The forces that drive the vertex motion are commonly derived from passive area and perimeter elasticity supplemented with additional active tensions [8–10]. However, the muscle metaphor for cellular interfaces suggests that *active tension* is central to the mechanical network underlying an epithelial tissue (Fig. 1D). This network rapidly equilibrates to a force balanced state [5, 11, 12], stabilized by mechanical feedback loops [13, 14]. In such an active tension network, passive elasticity plays a subdominant role. The need for stabilizing feedback loops arises because active tensions are untethered from interface lengths. Indeed, on an abstract level, these feedback loops are not unlike the regulatory mechanisms that control and stabilize skeletal musculature [15].

NHC and FB contributed equally.

* fbrauns@kitp.ucsb.edu

† shraiman@kitp.ucsb.edu

Here, we propose that tissue flow can be understood in the terms of an adiabatic remodeling of internal active force balance. Force balance in the cortical tension network defines a manifold of cellular tiling geometries on which tissue deformation unfolds. We propose that dynamics in the force-balance manifold is driven by positive feedback on the cortical tensions. This view is supported by analysis of high quality live imaging data [16] from *Drosophila* gastrulation presented in the companion paper [17]. Specifically, a geometric active-passive decomposition as well as mutant analysis were used to show that tissue flow is driven by internally generated tension dynamics, rather than external forces. Tension inference has provided evidence for the role of positive tension feedback during active T1 events. Numerical simulations of cell quartets show that such a feedback mechanism is sufficient to drive the T1 process. However, the question of coordination of T1s across the tissue – required to drive coherent tissue flow – has remained unanswered. To address this question, we develop a model of tissue mechanics in the tension-dominated regime and demonstrate via numerical simulations how positive feedback drives convergent extension. We show that order of the cell packing is necessary for coordinating T1 processes, and hence efficient convergent extension. T1s destroy this order such that the extent of tissue flow is self limiting. Thereby, our model reproduces the experimentally observed elongation of the germband where the arrest of flow is concomitant with a transition from an ordered to a disordered cell packing [17].

METHODS

A minimal model based on force balance and cell geometry

Our model is based on the assumption that on the timescales relevant to morphogenetic dynamics, the dominant active forces in the epithelium (generated by contractile myosin-2 motors in the adherens junctions, see Fig. 1C) are approximately balanced. In particular, we assume that adhesion forces between the epithelial layer and its substrate (the fluid yolk and perivitelline fluid [18] in the case of the *Drosophila* embryo) caused by the relatively slow morphogenetic motion, are negligible. Hence, all forces must be balanced within the transcellular network of cellular junctions. We model the tissue in the general framework of vertex models (see e.g. [7]) as a polygonal tiling of the plane with tri-cellular vertices \mathbf{r}_{ijk} , where each polygon represents a cell i (see Fig 1D). We focus on a setting where active cortical tensions dominate over passive elasticity. We write the elastic energy differential of this network as

$$dE(\{\mathbf{r}_{ijk}\}|\{T_{ij}\}) = \sum_{ij} T_{ij} d\ell_{ij} - p \sum_i dA_i + \varepsilon \sum_i dE_C(S_i), \quad (1)$$

where ε is a small parameter that separates the scale of active and passive mechanical contributions. $E_C(S_i)$ accounts for the passive elasticity of the cells and will be specified below; $\ell_{ij} = \|\mathbf{r}_{ij}\|$ is the length of the interface between adjacent cells i and j and T_{ij} is the cortical tension at that interface. Importantly, in contrast with the standard vertex model, where edge tension is defined by a constitutive relation corresponding to a passive Hookean perimeter spring, we take cortical tensions to be controlled independently of the interface lengths. The tension dynamics is described in the next section. The second term in Eq. (1) accounts for the effective in-plane pressure p of the cells that, by maintaining the total surface area (sum over individual cell areas A_i), ensures that the tissue as a whole does not collapse. In the *Drosophila* embryo, this is a consequence of the fact that the closed epithelial sheet encloses the yolk, which is under pressure, balancing the cortical tensions. Other epithelia are kept under tension via traction forces at the boundary [19]. We assume that pressure differences between cells are small and therefore absorb them into $E_C(S_i)$. In experimental data, the assumption of small pressure differentials can be verified by inspecting the curvature of cell-cell interfaces: Due to the Laplace law, significant forces due to pressure differences would manifest through curved cell-cell interfaces which are not observed in the early *Drosophila* embryo prior to the onset of cell divisions [12, 16, 17, 20].

We further assume a separation of scales between the timescale on which the elastic energy relaxes and the timescale on which the tissue deforms macroscopically. In other words, we assume relaxational dynamics $\gamma \partial_t \mathbf{r}_{ijk} = -\frac{\partial E}{\partial \mathbf{r}_{ijk}}$, with a relaxation rate – set by the coefficient of friction γ – much faster than all other timescales in the system. (Rather than frictional dissipation, one could equally use viscous dissipation here). Quasi-static force balance then implies

$$\frac{\partial E}{\partial \mathbf{r}_{ijk}} = 0. \quad (2)$$

Solving this equation to zeroth order in ε yields a force-balance constraints at each vertex. These constraints imply that the tension vectors $\mathbf{T}_{ij} = T_{ij} \mathbf{e}_{ij}$ at each vertex sum to zero and hence form a triangle as illustrated in 1D. Since neighboring vertices share the interface that connects them, the corresponding tension triangles share an edge. Therefore, all tension triangles have to fit together to tile the plane: they form a triangulation that is dual to the cell tiling [13, 21, 22]. This tension triangulation is a geometric manifestation of global force balance in the tissue, where angles at real-space vertices are complementary to the corresponding angles in the tension triangle angles. One pair of such angles is highlighted in Fig. 1D.

Importantly, fixing the angles at vertices *does not* fully determine the cell tessellation, i.e. the \mathbf{r}_{ijk} remain underdetermined, as this leaves the freedom to change the interface lengths ℓ_{ij} while preserving all angles. The re-

sulting *isogonal soft modes*¹ thus account for interface length changes under constant tension [13], which is possible thanks to the turnover of cytoskeletal elements.

The isogonal modes can dilate and shear cells as illustrated in Fig. 1F. They are soft modes of the leading order force balance constraints and thus force us to take into account subleading contributions to the elastic energy to arrive at a complete model of tissue mechanics. Cells resist shape distortions due to rigid cell-internal structures such as microtubules, the nucleus [23, 24], and intermediate filaments [25]. To account for this passive cell elasticity, we propose an energy

$$E_C(S) = \lambda[\text{Tr}(S - S_0)]^2 + \mu\text{Tr}[(S - S_0)^2], \quad (3)$$

in terms of the cell shape tensor

$$S_i = \sum_{k \in \mathcal{N}_i} \frac{\mathbf{r}_{ik} \otimes \mathbf{r}_{ik}}{\ell_{ik}}, \quad (4)$$

where \mathcal{N}_i is the set neighbors of cell i . This shape energy effectively models the cell interior as a homogeneous elastic material [26]. (In SI Sec. 4, we compare this elastic energy with the often-used “area-perimeter” elastic energy which we find produces qualitatively different behavior that is incompatible with experimental observations.) The shape tensor is defined so that it is invariant under subdivision of interfaces. The reference tensor S_0 controls the target cell shape and is given by $S_0 = 3\ell_0 \mathbb{I}$ for an isotropic hexagonal cell with side length ℓ_0 . External forces will deform the cell tessellation by acting on the isogonal modes. We can therefore relate cell elasticity and tissue elasticity by analyzing the energy spectrum of isogonal modes for a given tension triangulation (see SI Sec. 3). The two isogonal modes with the lowest energy correspond to uniform shear (see Fig. S13A). From these eigenmodes, we find a linear relationship between the cell and tissue shear moduli (see Fig. S13B).

For sufficiently small values of the scale-separation parameter ε , minimization of the elastic energy Eq. (1) can be performed in two separate steps: First, force balance of the dominant cortical tensions T_{ij} fixes the angles at vertices thus setting geometric constraints, but leaving isogonal modes undetermined. Second, the sub-leading term $\sum_i E_C(S_i)$ is minimized to fix these soft modes. Importantly, in this limiting case, the value of ε is immaterial as long as it is small enough (see SI Sec. 2). Figure 1G and Movie 1 illustrate the minimization of the cell shape energy under the angle constraints imposed by junctional force balance for the minimal setting of a

symmetric, regular cell array. The geometry is characterized by two interface lengths, ℓ_0 , ℓ_1 , and single angle ϕ . Incompressibility fixes ℓ_1 as a function of ℓ_0 and ϕ such that only a single isogonal degree of freedom ℓ_0 remains. We can plot the cell shape energy E_C in a two-dimensional energy landscape with the horizontal axis representing the tension-imposed angle constraint and the vertical axis representing the isogonal degrees of freedom. Force balance of the tensions T_0 , T_1 constrains the angle $\phi = 2 \arccos(T_0/2T_1)$ and relaxation of E_C takes place in the isogonal subspace (illustrated by the vertical white line in Fig. 1G), thus fully determining the cell geometry (purple dot). Changing the tensions T_0 , T_1 shifts the angle constraint and therefore forces the cell shape energy to relax to a new cell geometry. This changing of constraints mechanism is how dynamic remodeling of the tension configuration drives tissue flow. When the tensions reach the critical ratio $T_0/T_1 = \sqrt{2}$ such that $\phi = \pi/2$, the length of the vertical interface, ℓ_0 , vanishes causing a T1 transition as discussed in the companion paper [17]. To complete the model, we need to specify the dynamics governing the active tensions.

Positive feedback and adiabatic dynamics

On the timescale of morphogenetic flow, tensions change due to the recruitment and release of molecular motors, driving the remodeling of the force balance geometry encoded in the tension triangulation. To complete the model, we need to specify the dynamics that governs the tensions on this slow timescale.

Based on previous experiments [27] and models [10, 28], we propose a positive feedback mechanism where tension leads to further recruitment of myosin and thus further increase in tension. This self-amplifying accumulation of myosin on individual interfaces is limited by the competition for a limited pool of myosin within each cell. To mimic this local competition for myosin in a computationally simple way, we constrain tension dynamics to conserve the perimeter of each tension triangle, i.e. the sum of tensions at each vertex (ijk) . For an individual triangle with tensions $\tilde{T}_1, \tilde{T}_2, \tilde{T}_3$, we consider the dynamics

$$\tau_T \partial_t \tilde{T}_\alpha = \tilde{T}_\alpha^n - \frac{1}{3} \sum_{\beta=1}^3 \tilde{T}_\beta^n, \quad \text{with } \alpha = \{1, 2, 3\}, \quad (5)$$

where n is an exponent that determines the nonlinearity of the feedback. Note that each cell-cell interface is composed of two cortices on the two sides of the interface, and only one of the two is part of each local pool (see SI Sec. 4 for details). This feedback mechanism has a “winner-takes-all” character, where the longest edge in the tension triangle always outgrows the other two. In our model framework we can consider a variety of possible local tension dynamics. Below we will also investigate a form of positive tension feedback that saturates, and

¹ A simple counting of degrees of freedom shows that there is one isogonal degree of freedom per cell [13]. Therefore, the isogonal modes can be parametrized by an “isogonal function” that takes a scalar value in each cell. The isogonal displacement of a vertex is defined in terms of the values of this isogonal function in the three adjacent cells (see Eq. (S7)).

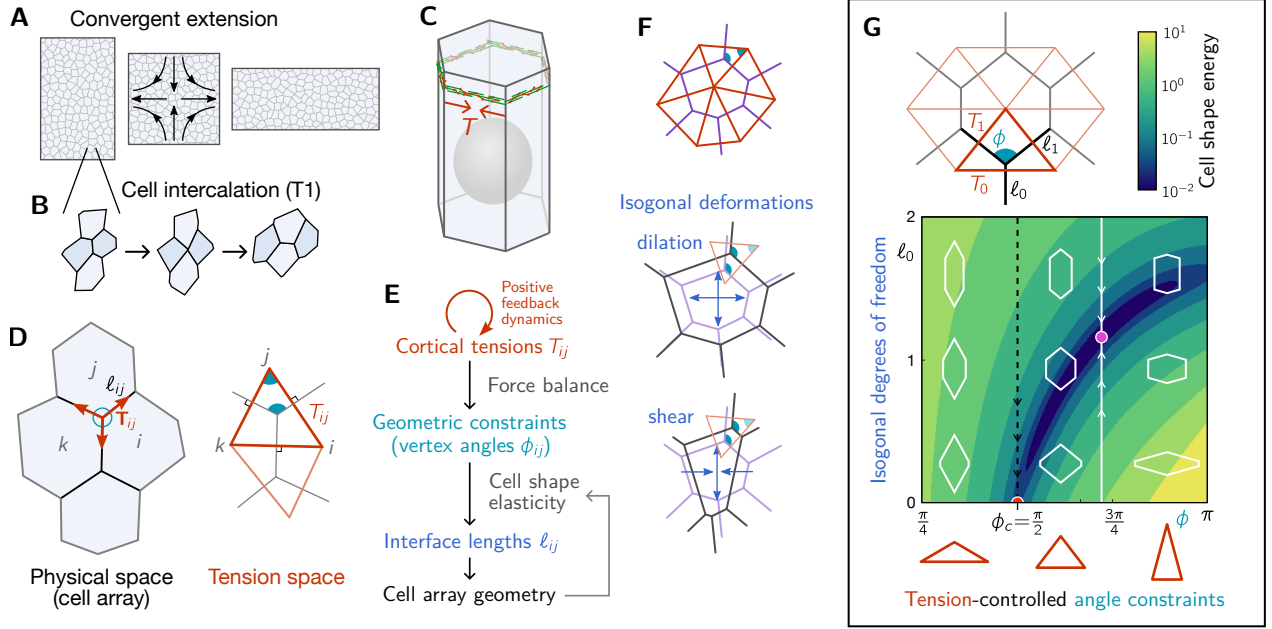


FIG. 1. A model for tissue mechanics dominated by cortical tension. **A** Convergent extension of epithelial tissue by cell intercalations (T1 processes, **B**). **C** A single cell from a columnar epithelium with the actomyosin cortex at the adherens junction belt generating tension T along cell-cell interfaces. Gray sphere represents the nucleus. **D** In force balance, the tensile forces \mathbf{T}_{ij} at each vertex must sum to zero, thus linking the tensions to the angles at which the interfaces meet. Force balance implies that the tensile force vectors at each vertex form a triangle. Triangles at neighboring vertices share an edge and thus form a triangulation that tiles the plane (i.e. they have to fit together without gaps or overlaps). This defines a “tension space” that is dual to physical space. The angles in the tension triangulation are complementary to the angles in the cell array, thus linking tension space to physical space. **E** Outline of our tissue model with mechanics dominated by actively regulated cortical tensions. Tension dynamics in adiabatic force balance are formulated as a geometric model of the tension triangulation which determines the angles at vertices. The remaining soft modes define isogonal (angle-preserving) degrees of freedom that are governed by cell-shape elastic energy, which accounts for (passive) non-cortical elasticity and penalizes dilation and shearing. **F** Illustration of isogonal deformations of a reference geometry (purple) that is dual to the tension triangulation (red). **G** Implementation of the model for a symmetric, regular cell array, characterized by one angle ϕ , determined by the tensions T_0, T_1 , and two lengths, ℓ_0 and ℓ_1 , parametrizing the soft isogonal modes. The contour plot shows the cell shape energy E_C in the incompressible limit where ℓ_1 is determined uniquely by ℓ_0 and ϕ . Relaxation of the sub-dominant cell shape energy E_C is constrained to the isogonal subspace (white line) determined by tension force balance. For the critical tension ratio $T_0/T_1 = \sqrt{2}$, constraining the angle to $\phi_c = \pi/2$ (black dashed line), the interface length minimizing E_C vanishes (red half-disk). See Movie 1 for an animated version.

identify the qualitative features of local tension dynamics key to the tissue dynamics.

Force balance requires that all tension triangles fit together to form a flat triangulation [13]. The triangulation is parameterized by a set of 2D tension vertex positions \mathbf{t}_i , so that the tension on edge (ij) is given by $T_{ij} = \|\mathbf{t}_i - \mathbf{t}_j\|$. In each iteration of the simulation, the tension vertices \mathbf{t}_i are determined by fitting the balanced tensions T_{ij} to the intrinsic tensions \tilde{T}_{ij} using a least squares method. In addition, the intrinsic tensions \tilde{T}_{ij} relax to the balanced tensions T_{ij} with a rate $\tau_{\text{balance}}^{-1}$ (see SI Sec. 4 for details). This “balancing” of the tension triangulation effectively accounts for small pressure differentials and additional feedback mechanisms (such as the strain rate feedback [13, 14]) which maintain the tension network in a state of force balance. In particular, this ensures that cortical tensions do not lead to build-up of pressure differentials. The rate at which these mech-

anisms act is controlled by the timescale τ_{balance} which we assume to be much smaller than the timescale τ_T on which tension evolve due to positive feedback. All quantifications presented here refer to the flat tensions T_{ij} .

The above dynamics is autonomous in tension space until an edge in the cell tessellation reaches length zero. At this point, a cell neighbor exchange (T1 transition) occurs, corresponding to an edge flip in the tension triangulation. After this topological modification, the tension dynamics continues autonomously again until the next T1 event. To determine the active tension (i.e. myosin level) on the new interface formed during the cell neighbor exchange, we assume continuity of myosin concentration at vertices as described in the companion paper [17] and in SI Sec. 4. The active tension is not sufficient to balance the total tension on the new interface, such that passive elements of the cortex (e.g. crosslinkers) are transiently loaded. The resulting passive ten-

sion relaxes due to remodeling with timescale τ_p (see SI Sec. 4 for details). This relaxation causes the elongation of the new interface as it transiently counteracts positive tension feedback and thereby prevents the new interface from immediately re-collapsing after a T1.

This concludes the description of the computational model. A brief overview over the parameters and their effects, several of which will be discussed in detail below, is given in SI Table I and Fig. S8. Fig. S15 provides a flow chart of the simulation algorithm.

RESULTS

Cell packing order facilitates self-organized convergent-extension flow

In the companion paper [17], we have shown that positive tension feedback can drive an active T1 transition in a cell quartet where the inner interface is initially under slightly higher tension than its neighbors. The simulations were performed in a quartet of identical cells, representing a perfectly regular lattice of cells. However, any real tissue will exhibit some degree of irregularity. Investigating the effect of this disorder is key to understand convergent extension on the tissue scale. To this end, we perform simulations of irregular cell arrays. All parameters are set to the same values as in the companion paper, where the time scale τ_T was calibrated to fit the tension and interface length dynamics of active T1s during *Drosophila* gastrulation. The local T1-dynamics of the tissue-scale simulations are quantified in Fig. S5, and match the experimental data quite well. We start with simulations of a freely suspended patch of tissue to investigate the role of initial tension anisotropy and order in the cell packing. Further below, we will present simulations that combine active with passive tissue regions, mimicking the *Drosophila* germ band and the adjacent amnioserosa tissue.

We define a tension anisotropy tensor $Q = \frac{2}{3} \sum_{\alpha=1}^3 \mathbf{T}_\alpha \otimes \mathbf{T}_\alpha$ for each triangle directly from the tension geometry. Averaging its deviatoric part $\tilde{Q} = Q - \frac{1}{2} \text{Tr} Q$ over the cell array, provides a measure of global tension anisotropy $\|\langle \sqrt{2} \tilde{Q} \rangle\|$. The normalization factor $\sqrt{2}$ is chosen such that this measure takes values in the interval $[0, 1]$, and $\langle \cdot \rangle$ indicates the average over all triangles in the triangulation. Starting with a slightly perturbed hexagonal cell packing and an initial anisotropy of 0.175, the tissue patch undergoes convergent extension elongating the tissue perpendicular to the initial orientation of global tension anisotropy (Fig. 2A).

The tissue flow is driven by self-organized cell rearrangements (active T1 transitions) whose rate rapidly increases, reaching a maximum, and then decreases to a lower, but non-zero, value (Fig. 2D). Large-scale tissue deformation stalls after approximately 2-fold convergent extension (as measured by the square root of the

aspect ratio $a = \text{width}/\text{height}$, Fig. 2C) while cells continue rearranging. This suggests that T1s at this stage are no longer coherently oriented and therefore do not contribute to net tissue deformation. Indeed, the efficiency of T1s at driving convergent extension drops after the T1 rate has peaked (Fig. 2D).

As cells rearrange, the tissue becomes increasingly disordered, as indicated by the loss of global tension anisotropy and the decreasing fraction of cells with six neighbors, p_6 (Fig. 2E). The peak of tension anisotropy in the ordered initial condition coincides with the onset of T1 transitions and the decay of p_6 (Fig. S8).

To test the role of initial order in the cell packing, we initialize the simulation from a random Voronoi tessellation but an identical tension anisotropy of 0.175, which results in slower convergent-extension flow and arrest of flow at a smaller amount of total tissue-scale deformation (Figs. 2B and 2C and Movie 2). Notably, tension anisotropy rapidly vanishes without the transient increase observed in the simulation starting with a more ordered cell packing (Fig. 2E). While the early dynamics depends sensitively on the initial condition, we find rapid convergence toward a common disordered steady state.

A common measure for the degree of order in a polygonal tiling is the cell shape index ($s = P/\sqrt{A}$, with cell perimeter P and area A), shown in Fig. 2F. This shape index is high when cell shapes are elongated or irregular and approaches the minimal value $s \approx 3.72$ for a regular hexagon. The shape index has a particular relevance in vertex models employing an area-perimeter based elastic energy [7, 30]. In these models, the *target* shape index is a control parameter that drives a solid to fluid transition [29]: a high target shape index ($s_0 > s_0^* \approx 3.81$) is associated with tissue fluidity since it allows for cell rearrangements, while a low cell target shape index gives rise to a solid state. In both cases, the observed shape index is controlled by the target shape index. In contrast, in our simulations with actively driven T1s, disorder, and thus a high observed shape index, is the consequence of cell rearrangements, rather than their cause. Notably, we find more tissue flow when the observed shape index is initially low (Fig. 2F). The question of the solid vs fluid character of tissue will be addressed in more detail in the last part of the results section and in the discussion.

To systematically investigate the role of tension anisotropy and cell packing order on self-organized convergent extension, we generated initial tension triangulations from random hard disk packings at different packing fractions ρ [31, 32]. Specifically, we sample the positions of the tension vertices \mathbf{t}_i from a hard disk process, and then construct the corresponding Delaunay triangulation. At low packing fraction, the hard disk process generates highly irregular triangulations with broadly distributed coordination numbers (see Fig. 2B). In contrast, at sufficiently high packing fraction $\rho \gtrsim 0.72$, the disks adopt a crystalline hexagonal packing such that $p_6 \approx 1$. The plot at the bottom of Figure 3A shows how the degree of order continuously varies with ρ between these

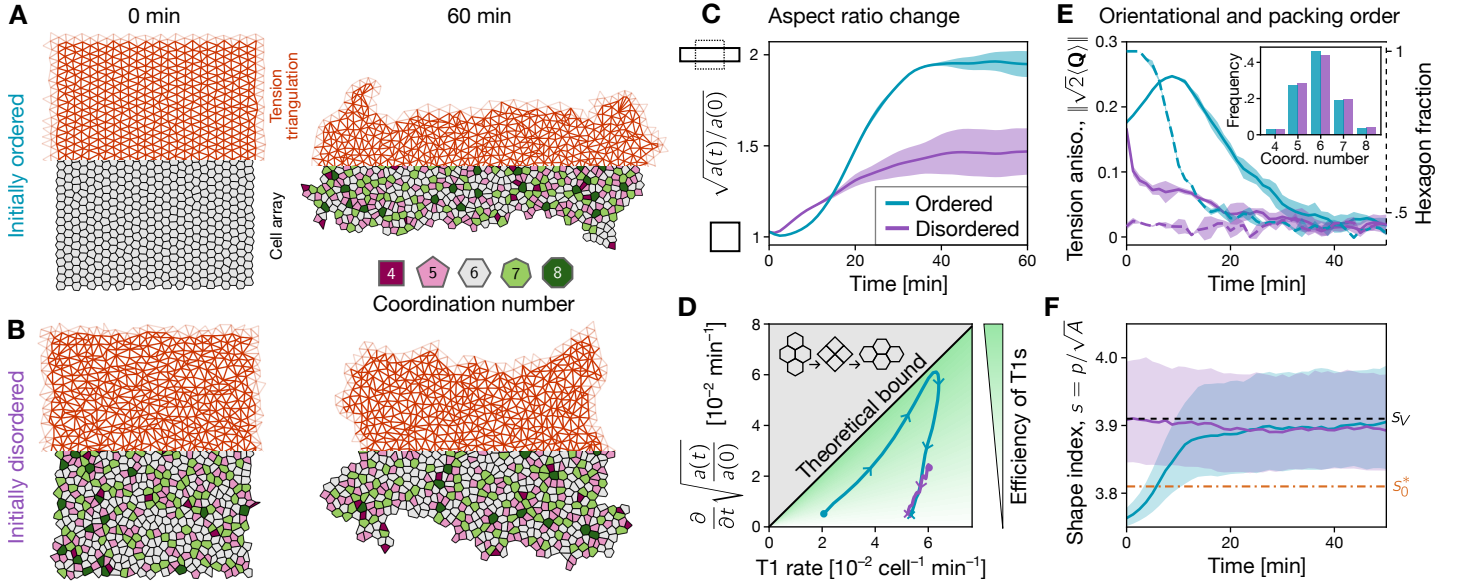


FIG. 2. Extent of tissue flow depends on initial cell-scale order and tension anisotropy. **A, B** Simulation snapshots of tissue patches with free boundaries starting from an (irregular) hexagonal cell array (**A**) and a disordered cell array (**B**) generated from a random Voronoi tessellation. The net deformation is significantly smaller in the latter case. In both cases the final configuration is disordered. Each snapshot shows the top half of the tension triangulation and the bottom half of the corresponding cell array. Note the initial tension triangulation is stretched along the x direction and compressed along the y direction as a result of the prescribed initial tension anisotropy. **C** Convergent extension (measured by the tissue aspect ratio $a(t)$) is slower and ceases at a smaller net deformation for a disordered initial condition (cyan line) compared to the initially ordered case (purple line). Shaded bands indicate standard deviation over $N = 3$ simulation runs with $N_{\text{cells}} \approx 10^3$ cells each. **D** Plotting the rate of tissue convergent extension against the T1 rate provides a measure for the efficiency of T1 transitions. For the initially ordered tissue, the efficiency of T1s starts out near the theoretical optimum but drops to zero as the tissue becomes disordered. For the disordered initial condition, T1s are inefficient from the beginning. The theoretical bound (for cells retaining isotropic shape) is a factor of $\sqrt{3}$ elongation for one T1 per cell (i.e. each cell participates in two T1s) as illustrated in the inset cartoon. **E** Decreasing hexagon fraction (solid lines) and global tension anisotropy (dashed lines) indicate the decay of order in the cell arrays. Notably, in the initially ordered cell array, tension anisotropy transiently increases due to positive tension feedback (solid purple line). At late times both simulations converge to zero global tension anisotropy and identical coordination number statistics (inset). **F** As order is lost, the cell-shape index s converges to that of a random Voronoi tessellation s_V (dashed black line). Note that the critical shape index for the rigidity transition in the “classical” vertex model [29], $s_0^* \approx 3.81$ (dot-dashed orange line), does not feature in our results. Lines show the median, shaded bands indicates quartiles.

two extremes. To introduce a specified initial tension anisotropy, the triangulation is sheared with magnitude s (displacing vertices by $\mathbf{t}_i \mapsto \text{diag}(\sqrt{1+s}, 1/\sqrt{1+s}) \mathbf{t}_i$).

The heatmap in Fig. 3A (top) shows the dependence of convergent extension on the initial configuration controlled by ρ and s . The total extent of convergent extension, quantified by the net change in aspect ratio $\sqrt{a_{\text{final}}/a_{\text{initial}}}$ increases continuously with both the initial order and the magnitude of tension anisotropy. As we have seen above, both these quantities decrease as cells rearrange (cf. Fig. 2E). In fact, when plotting the remaining extent of convergent extension $\sqrt{a_{\text{final}}/a(t)}$ against $p_6(t)$ and $\|\langle\sqrt{2}\tilde{Q}(t)\rangle\|$, we find trajectories that approximately lie in a common plane and converge to a fixed point at vanishing anisotropy $\|\langle\sqrt{2}\tilde{Q}\rangle\| \approx 0$ and $p_6 \approx 0.4$ (Fig. 3B). Based on these results, we hypothesize an empirical law for feedback-driven convergent extension, based on the instantaneous hexagon fraction and tension

anisotropy:

$$\sqrt{\frac{a_{\text{final}}}{a(t)}} \approx c_Q \|\langle\sqrt{2}\tilde{Q}(t)\rangle\| + c_6 p_6(t) \quad (6)$$

With the coefficients determined by a linear fit, Eq. (6) predicts the remaining extent of convergent extension with less than 10% mean absolute error (Fig. 3C). The empirical relation Eq. (6) is specific to the particular choice of microscopic tension dynamics employed in the simulations: a systematic search for a more general relation linking microscopic ($p_6, \|\langle\sqrt{2}\tilde{Q}(t)\rangle\|$) and macroscopic ($a(t)$) quantities is beyond the scope of the present work. Note further that we have focused on degree of order in the topology (i.e. coordination numbers) of the triangulation, quantified by p_6 . A different manner of introducing disorder is via random displacements of the triangulation vertices while keeping the topology fixed, which we study in (see Fig. S8). This form of disorder

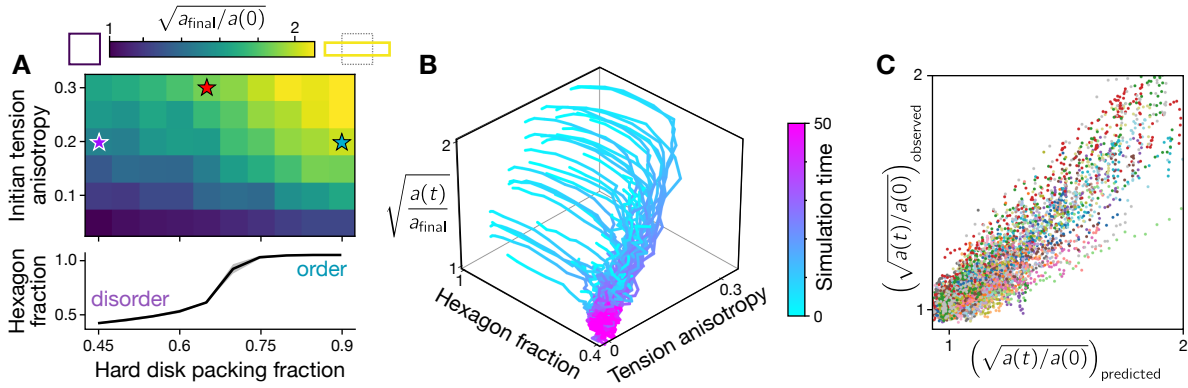


FIG. 3. Hexagon fraction and tension anisotropy predict tissue flow. **A** The total amount of convergent-extension (overall tissue aspect ratio change $a_{\text{final}}/a(0)$) increases as a function of cell packing order (controlled by hard disk packing fraction ρ used to generate the Voronoi seed points) and initial tension anisotropy (controlled by a strain s applied to the tension triangulation). The hard disk packing fraction ρ controls the fraction of hexagonal cells (bottom). The purple and green stars indicate the initial condition parameters used for Fig. 2A and Fig. 2B respectively. The red star indicates the approximate state of the *Drosophila* germ band at the onset of germ band extension (cf. Fig. S1B). **B** Hexagon fraction, p_6 , and tension anisotropy $||\langle\sqrt{2}\tilde{Q}\rangle||$ decrease as cells rearrange and eventually converge to a fixed point where anisotropy vanishes and the hexagon fraction matches a random Voronoi tessellation (~ 0.4). At this point, convergent-extension flow, as measured by the remaining change in tissue aspect ratio $a_{\text{final}}/a(t)$, stalls (cf. Fig. 2C, E). The trajectories approximately collapse onto a plane, suggesting that a linear relationship can predict the convergent-extension in terms of p_6 and $||\langle\sqrt{2}\tilde{Q}\rangle||$; see Eq. (6). **C** Correlation between predicted and observed change in aspect ratio. Data points are from simulations with initial conditions, spanning the entire parameter diagram in (A), showing that the prediction works across many different initial conditions. Points with the same color indicate different time point from the same simulation.

also decreases convergence-extension flow.

The model introduced above implements a specific form of positive tension feedback, Eq. (5), in such a way that total tension is conserved locally. We find qualitatively similar results for tension dynamics with different local conservation laws. Notably, positive feedback conserving areas of tension triangle instead of their perimeters produces slightly more convergent extension and exhibits an even stronger dependence of tissue flow on the initial degree of order (see SI Sec. 2). How tissue dynamics depends on the parameters $\tau_{\text{balance}}, \mu, \lambda, n$ is summarized in SI Table I and Fig. S8. We will return to the effect of specific parameters throughout the following sections.

Taken together, our model reproduces several salient features of germ-band extension in the *Drosophila* embryo. We find that convergent extension driven by positive tension feedback is self-limiting and naturally explains the transition from the fast to the slow phase of germ-band extension [17]. It also reproduces that the slowdown of convergent extension is concomitant with an increase in cell-scale disorder, approaching a maximally disordered state [17, 33]. Our model suggests that the transient fast phase of flow is facilitated by an initial near-hexagonal packing of the cells. In the *Drosophila* embryo, this packing results from physical interactions of the spindle apparatuses during the syncytial cell division cycles that precede cellularization [34, 35]. Quantification of hexagonal order in the experimental data are shown in Fig. S1. We predict that disrupting the ini-

tial cell packing will cause GBE to become slower. The experimental data analysis in Ref. [17] demonstrates the presence of large-scale tension anisotropy before the onset of convergent extension, which in the model is required to orient tissue flow. More precisely, Ref. [17] as well as Figs. S1, S2, and S3 suggest that the *Drosophila* germ band corresponds, approximately, to a hard disk packing fraction 0.65 and an initial anisotropy of 0.3 on the convergent extension heat map Fig. 3A. This predicts an ca. 1.85-fold extension. We attribute the additional elongation observed in the experimental data to external pulling forces [8] and ventral furrow invagination, which provides an external source of tension anisotropy via strain-rate feedback [14]. Both factors are not present in the simulations Fig. 3A. More broadly, our results suggest that convergence extension via positive tension feedback may generally be self-limiting, as also noted in a recent model by Sknepnek *et al.*[10].

Order in local tension configurations

So far, we have focused on the role of anisotropy and initial topological order in the cell packing. In the *Drosophila* germ band, we additionally observed a more subtle form of geometric order – a particular pattern of alternating high and low tensions [17] – that precedes the onset of cell rearrangements. This cell-scale tension pattern is not apparent initially but arises dynamically in conjunction with an increase in overall tension anisotropy.

ropy which suggests that this tension pattern arises from the positive tension feedback. As we show in the following, systematically quantifying the local configurations of cortical tensions provides a method to constrain physical models of cell rearrangements in epithelia.

The elementary motifs of a cell-scale tension pattern are the tension configurations at individual vertices. In force balance, the tension vectors at each vertex form a triangle. This allows one to characterize the tension configuration based on the shape of the tension triangle: acute triangles correspond to tension cables (adjacent high tension interfaces) while obtuse triangles correspond to an isolated high tension interface which we refer to as a tension “bridge”. The latter configuration is the elementary motif of an alternating pattern of high and low tensions as illustrated in Fig. 4A.

To quantify the relative abundance of these motifs, we define a local tension configuration (LTC) parameter that measures how anisotropic and how acute vs obtuse the tension triangle is. We order the three tension vectors $\mathbf{T}_\alpha, \alpha = 1, 2, 3$ that form the tension triangle by increasing length, i.e. $T_1 \leq T_2 \leq T_3$. We then use the force-balance condition $\sum_\alpha \mathbf{T}_\alpha = 0$ to define the reduced barycentric vectors, combined into a 2×2 matrix

$$\mathfrak{T} = \begin{pmatrix} \tau_1 \\ \tau_2 \end{pmatrix} = \frac{1}{\sqrt{2}\mathcal{N}} \begin{pmatrix} T_1^x - T_2^x & T_1^y - T_2^y \\ \sqrt{3}T_3^x & \sqrt{3}T_3^y \end{pmatrix}. \quad (7)$$

where the normalization factor \mathcal{N} ensures $\|\mathfrak{T}\|^2 = \text{Tr}[\mathfrak{T}\mathfrak{T}^T] = 1$. This normalization fixes the arbitrary overall tension scale. Note that \mathfrak{T} is not a symmetric matrix and that its indices belong to different spaces: the first labels the barycentric component and the second the Cartesian coordinate. The triangle anisotropy tensor Q defined above is given by $Q = \mathfrak{T}^T \mathfrak{T}$. We now carry out a singular value decomposition (SVD):²

$$\mathfrak{T} = R(\psi) \cdot M \cdot \begin{pmatrix} \sqrt{s_1} & 0 \\ 0 & \sqrt{s_2} \end{pmatrix} \cdot R^T(\phi), \quad (8)$$

where $R(\alpha)$ is the rotation matrix with angle α , M is a reflection matrix, the singular values $s_1 > s_2 > 0$ by convention, and $s_1 + s_2 = 1$ because we have normalized the tension vectors. Because of triangle symmetries, we can always choose $\psi \in [0, \pi/3]$ (see below). We now introduce the complex order parameter

$$\tilde{s} e^{i\tilde{\psi}} \text{ with } \tilde{s} = (s_1 - s_2) \in [0, 1], \tilde{\psi} = 3\psi \in [0, \pi] \quad (9)$$

which provides a complete description of the triangle’s *intrinsic* shape. The magnitude $\tilde{s} = s_2 - s_1$ measures the triangle’s anisotropy, and the “LTC phase” $\tilde{\psi}$ measures the triangle’s degree of acuteness vs obtuseness. Applied

to tension triangles, the thus-defined LTC *order parameter* informs about the configuration of tensions at a vertex. We note that $\det M = \pm 1$ indicates the chirality of the triangle’s shape, which might be useful to detect chiral symmetry breaking on the cellular scale, e.g. in the *Drosophila* hindgut [37].

Geometrically, the SVD of \mathfrak{T} can be understood as a sequence of transformations that map an equilateral reference triangle (with one edge parallel to the x -axis) to the target triangle (Fig. 4B). The reference triangle is first rotated by an angle ψ , then stretched along the x - and y -axis with factors s_1 and s_2 , and finally rotated again by an angle $-\phi$ (the minus sign results from the convention in defining SVD). ϕ therefore determines the triangle’s axis of anisotropy while ψ determines the orientation of the shear axis to one of the edges of the original equilateral triangle. For $\psi = 0$, the shear is orthogonal to a triangle side, yielding an isosceles obtuse triangle. Increasing ψ makes the resulting triangle more acute, until maximal acuteness is reached at $\psi = \pi/3$. For an illustration of how $\tilde{s}, \tilde{\psi}$ relate to the internal triangle angles, see Fig. S4.

A generalized Delaunay condition defines the locus of T1 events in LTC space

Before we use the LTC parameter to quantify the tension space dynamics from simulations and experiments, we define a condition in the LTC space for when a T1 transitions will happen. This T1 threshold puts a constraint on the local tension configurations that we expect to observe. Moreover, it will allow us to quantify how tension dynamics causes active T1s by driving the local tension configurations towards the T1 threshold.

Let us for a moment neglect the isogonal modes. From the tension triangulation we construct the corresponding Voronoi tessellation whose vertices are the circumcircle centers of the triangles as illustrated in Fig. 4D. The edges of the Voronoi tessellation are orthogonal to those of the triangulation, which implies that it obeys the force balance constraints, and can be used as a reference for the family of cell arrays compatible with the tension triangulation. The length of a Voronoi edge corresponding to a pair of adjacent triangles is given by

$$\ell_{\text{ref}} = \frac{\sqrt{3}\ell_0 T}{2} (\cot \beta + \cot \beta'), \quad (10)$$

where T length of the shared triangle edge interface and ℓ_0 fixes the length scale such that ℓ_0 is the edge length of a regular hexagonal cell, corresponding to equilateral tension triangles with $T = 1$. ℓ_{ref} changes sign at $\beta + \beta' = \pi$, which gives the “Delaunay condition” $\beta + \beta' < \pi$. In the absence of isogonal strain, a cell neighbor exchange (corresponding to an edge flip in the triangulation) occurs at this threshold. In Fig. 4C, the gray line indicates this threshold for a pair of identical triangles (i.e. $\beta = \beta' = \pi/2$). Notably, the threshold is at a much

² This decomposition was used in Ref. [36] to quantify tissue strain rates from a cell-centroid-based triangulation. However, the information contained in the “LTC phase” ψ was not utilized there.

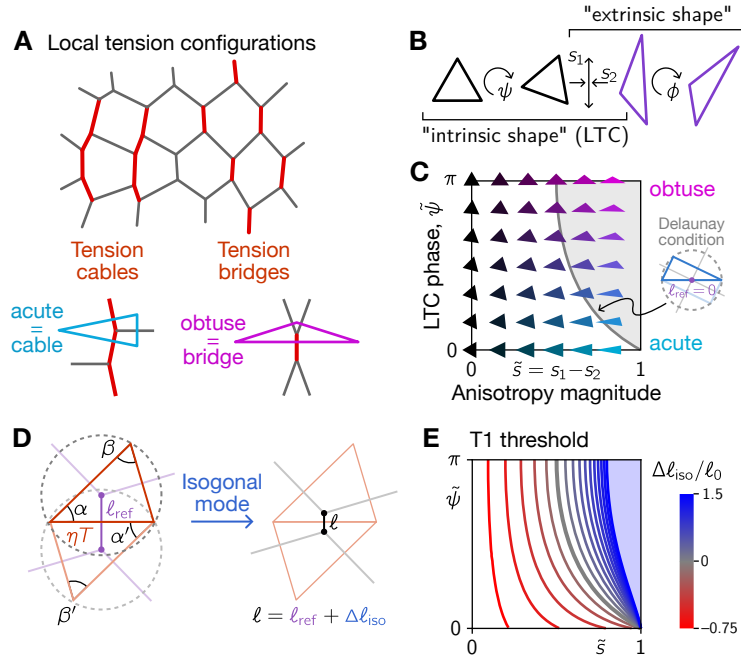


FIG. 4. Triangle shape space characterises the local tension motifs that underlie cell rearrangements. **A** We distinguish two tension patterns, “cables” and “bridges”, by their elementary motifs of tension configuration at individual vertices. These configurations can be quantified in terms of the tension triangle shapes which we use to define a local tension configuration (LTC) parameter. **B** Shape decomposition of a triangle into a sequence of three transformations acting on an equilateral reference triangle. The angle ψ and the shear factors $s_{1,2}$ determine the intrinsic shape of the triangle while the angle ϕ determines its orientation in space. **C** The intrinsic shape of triangles can be quantified by a complex order parameter $\tilde{s} e^{i\tilde{\psi}}$, where the LTC magnitude \tilde{s} is proportional to the triangle’s anisotropy and the LTC phase $\tilde{\psi}$ distinguishes obtuse and acute triangles. The gray line indicates the Delaunay condition for a pair of identical triangles. Along this line, the circumcenters of the two triangles coincide, corresponding to a fourfold vertex in the Voronoi tessellation. This line therefore defines a threshold for T1 events in the case of vanishing isogonal strain. **D** Circumcircle construction of the Voronoi edge length (purple) from a pair of adjacent (tension) triangles (red). Circumcircles are indicated by gray dashed lines. The actual physical length ℓ is the sum of the Voronoi reference length ℓ_{ref} and a contribution from isogonal strain $\Delta\ell_{\text{iso}}$. In the illustration, $\Delta\ell_{\text{iso}}/\ell_0$ is negative. **E** T1 threshold as a function of the isogonal strain $\Delta\ell_{\text{iso}}/\ell_0$. Positive isogonal strain shifts the threshold to higher tension anisotropy.

smaller anisotropy magnitude \tilde{s} for tension cables (small $\tilde{\psi}$) than for bridges (large $\tilde{\psi}$), implying that tension cables are less efficient at driving intercalations than tension bridges.

How does the Delaunay condition generalize in the presence of isogonal strain? The length of the central interface, ℓ , can be decomposed into two contributions

$$\ell = \ell_{\text{ref}} + \Delta\ell_{\text{iso}}, \quad (11)$$

where the isogonal contribution $\Delta\ell_{\text{iso}}$ accounts for isogonal modes while the (Voronoi) reference length is given by Eq. (10). Note that $\Delta\ell_{\text{iso}}$ is not an edge-autonomous quantity but depends on the isogonal mode (parametrized by the isogonal function) in the four cells surrounding the interface. In practice, $\Delta\ell_{\text{iso}}$ can be estimated from the average isogonal strain tensor in a local tissue patch [17]. Now an interface collapses if the *physical* length reaches zero: $\ell_{\text{ref}} + \Delta\ell_{\text{iso}} = 0$. This generalizes the Delaunay condition.

To find the resulting T1 threshold in the LTC space,

we need to express the tension T on the cell quartet’s inner interface in terms of the angles $\alpha, \alpha', \beta, \beta'$. Reasoning that on average the two tension triangles in a quartet will be similar, we consider the simplified case $\alpha = \alpha', \beta = \beta'$. Normalizing by the average tension we find $T = 3 \sin(\beta) / (\sin \alpha + \sin \beta + \sin(\alpha + \beta))$. Since the problem is now reduced to the shape of one triangle, the T1 condition $\ell_{\text{ref}}(\alpha, \beta) + \Delta\ell_{\text{iso}} = 0$ defines a threshold line in the LTC space. Figure 4E shows the T1 threshold as a function of the isogonal strain $\Delta\ell_{\text{iso}}/\ell_0$. The critical tension anisotropy drops to zero as $\Delta\ell_{\text{iso}}/\ell_0$ approaches -1 , the critical isogonal strain for purely passive T1s which takes place for isotropic tension (i.e. equilateral tension triangles). Vice versa, positive isogonal strain shifts the T1 threshold to higher magnitude of tension anisotropy. In principle, the above geometric reasoning can be generalized to an arbitrary tension “kite” composed of two different tension triangles. However, the shape space of such kites is four dimensional (since there are four independent angles $\alpha, \alpha', \beta, \beta'$) which precludes the intuitive

visualization that the single-triangle LTC space provides.

Winner-takes-all feedback drives coherent T1s through formation of tension bridges

With the LTC order parameter and the T1 threshold in hand, we can now quantify the dynamics of tensions in the simulations (see Fig. 5A) and experiments (see companion paper Ref. [17] and Fig. S2). Because isogonal strain shifts the T1 threshold, it will have a significant effect on the LTC order parameter distribution. We therefore performed simulations where we impose the isogonal strain observed in the *Drosophila* germ band [17] (see SI Sec. 2 for details). The initial tension triangulations were taken to be perturbed lattices with tension anisotropy 0.175. The germ band is stretched by the invagination of the adjacent mesoderm tissue causing isogonal strain along the axis of tension anisotropy (dorsal-ventral). This shifts the T1 threshold towards stronger tension anisotropy \tilde{s} (cf. Fig. 4E).

At the beginning of the simulation, the local tension anisotropy \tilde{s} is small and there is no bias towards cables or bridges. Positive tension feedback amplifies local anisotropy and thus drives the tension configurations towards the T1 threshold (Fig. 5A). At the onset of T1s, we observe an increased fraction of tension bridges, in agreement with the experimental observations (8 min in Fig. 5A). At late times, where the tissue becomes highly disordered, the distribution in LTC space shifts more towards tension cables (30 min). As we will see below, this late time distribution is reproduced by a random Delaunay triangulation. Time traces of the median anisotropy \tilde{s} and (weighted) median LTC phase $\tilde{\psi}$ show qualitative agreement with data from the *Drosophila* germ band [17], see Fig. 5B. In fact, a quantitative agreement can be achieved by shifting the median anisotropy and LTC phase by constant offsets, as indicated by the dashed lines in Fig. 5B. These offsets may be a consequence of noise in the experimental data, which we support in Fig. S8 with simulations that incorporate Langevin noise in the tension dynamics.

To understand how tension bridges emerge transiently, consider the shape dynamics of a single, isolated tension triangle governed by winner-takes-all feedback Eq. (5). Starting from a configuration with nearly equal tensions, i.e. a nearly equilateral tension triangle, winner-takes-all feedback causes the highest tension (longest edge in the triangle) to grow at the expense of the other two. The triangle is thus driven towards an increasingly obtuse shape, as illustrated in Fig. 5C. Visualizing this dynamics as a flow in LTC space, shows that it drives the tension configurations towards the T1 threshold and thereby causes the cell rearrangements. The single-triangle simulation successfully predicts early dynamics of the LTC distribution until the onset of cell rearrangements (see Fig. 5B, C'). While positive tension feedback explains the emergence of tension bridges at the single-vertex level, it

is not enough to produce an alternating pattern of tensions across cells. This pattern requires that the elementary tension configuration motifs (bridges) fit together coherently, i.e. their tension anisotropy is aligned across cells. This requires that the coordination number of a majority of cells is 6, i.e. that most cells are hexagons. This explains why hexagonal packing order is required to drive coherent T1s that underlie rapid convergent extension.

For a highly ordered initial packing, i.e. a nearly hexagonal lattice of cells, the lattice orientation relative to the axis of mean tension anisotropy determines the initial fraction of tension bridges. It is maximal when one side of the hexagonal cells is parallel to the orientation of tension anisotropy and minimal when one side is perpendicular (see Fig. S7). In simulations we find that this initial bias only weakly affects the initial rate of tissue extension and has no significant effect at later times.

In the simulation discussed above we imposed isogonal strain to account for the transient stretching of the germ band by the invaginating mesoderm. In simulations without imposed isogonal strain, the bridge fraction does not transiently increase (see Fig. S8). This is because the T1 threshold is at a significantly lower anisotropy for tension bridges than for tension cables and this difference is more pronounced for vanishing isogonal strain, causing tension bridges to be rapidly eliminated by T1s (see gray line in Fig. 5C). We therefore predict that T1s will happen at a lower tension anisotropy (and lower tension-bridge fraction) in a tissue with no isogonal strain, e.g. in a *twist* mutant embryo where mesoderm invagination is abolished.

Loss of order in local tension configurations. Above, we have seen that the cell array becomes disordered as cells rearrange. The coordination number statistics and average shape index approach a random Voronoi tessellation (cf. Fig. 2E, F). This suggests that we can characterize the corresponding tension triangulations as random Delaunay triangulations. Their statistics of such a triangulation depend on the underlying stochastic point process. We use the same hard disk sampling method as above, controlled by the packing fraction ρ to generate a family of Delaunay triangulations. The triangle shape statistics (characterized by the LTC parameter) found at late times both in simulations and in the *Drosophila* germ band are reasonably well reproduced by a random Delaunay triangulation seeded from a hard disks with $\rho \approx 0.2$ (Fig. 5D, D' and Fig. S3). This observed "randomization" in tension space suggests that the triangle edge flips can be statistically understood as a random "mixing". Notably, the late-time distribution exhibits a bias towards tension cables. The loss of tension bridges causes active T1s to become incoherent and incompatible between adjacent cells, contributing to a slowdown of tissue extension found in tissue scale simulations and in the germ band [17].

Taken together, we find that the time course of LTC distribution agrees between the model and the experi-

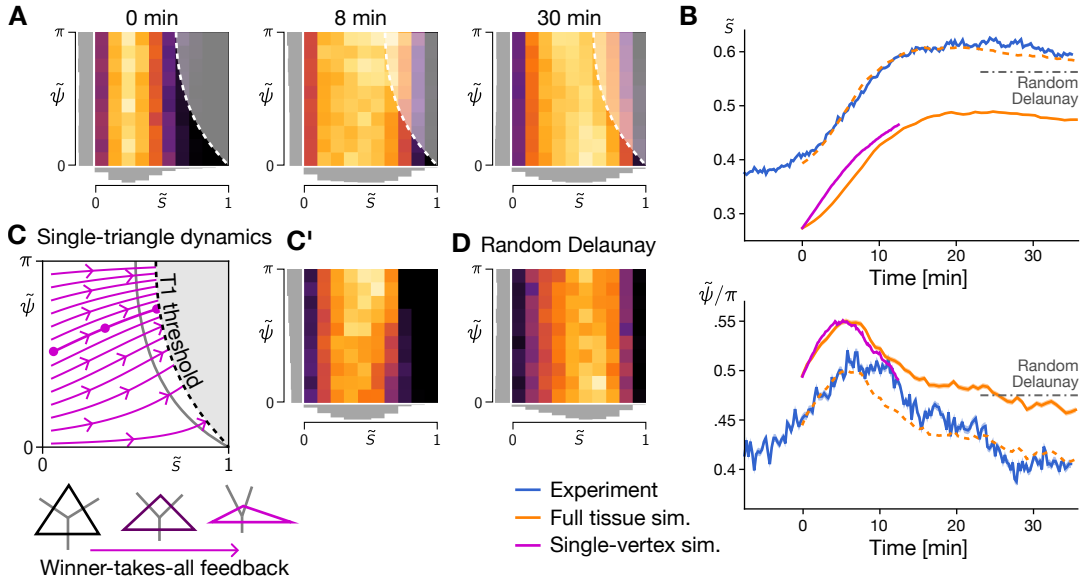


FIG. 5. **Dynamics of LTC order in simulations and the *Drosophila* germ band.** **A** Heat maps showing the distribution of local tension configurations in a simulation with imposed isogonal strain matching the experimental observations. Data aggregated from $N = 6$ simulation runs of $\sim 10^3$ cells each. **B** Driven by winner-takes-all feedback, the magnitude of tension anisotropy magnitude \tilde{s} (top) and the tension bridge fraction (measured by the LTC phase $\tilde{\psi}$; bottom) increase. The bridge fraction decreases as the tissue becomes disordered due to cell rearrangements. Solid lines show the median of the LTC distributions where the phase $\tilde{\psi}$ is weighted with the magnitude \tilde{s} . The width of bands showing the standard error is comparable to the line width. Shifting the median from simulations by a constant offset (see dashed orange lines) yields a quantitative match to the experimental data. **C** Shape dynamics of a single tension triangle driven by winner-takes-all feedback rapidly drives the tensions towards the T1 threshold with a slight bias towards tension bridges. **C'** LTC distribution predicted by single-triangle simulation reproduces the LTC distribution at the onset of cell rearrangements in full tissue simulations (cf. distribution at 8 min in A). **D** A random Delaunay triangulation seeded from hard disks with a packing fraction $\rho = 0.2$ reproduces the late-time distribution in simulations.

mental data. Next, we show how changing various aspects of the model affects the LTC distribution, highlighting that the LTC parameter can be used to distinguish different tension dynamics based on *statistical* signatures of cell-scale observations.

Saturating tension feedback causes tension cable formation and reduced convergence extension

So far, we used a “winner-takes-all” local tension feedback mechanism, Eq. (5), which drives the formation of tension bridges as illustrated in Fig. 5C. In contrast, when positive feedback rapidly saturates, adjacent high tension interfaces no longer compete, thus leading to the formation of tension cables (Fig. 6A; see SI Sec. 2 for details). The trajectories in LTC space obtained from single-triangle simulations show that saturating feedback is less efficient at driving the local tension configuration towards the T1 threshold. Indeed, tissue scale simulations with such feedback produce very little convergent extension (see Fig. 6B, D and Movie 3). The rate of T1 transitions is significantly reduced (Fig. 6E), and in contrast to “winner-takes-all” feedback, a significant fraction of T1 transitions (approximately 20%) are reversible, i.e.

the newly formed edge rapidly re-collapses (see SI Sec. 2). Saturating tension feedback might therefore explain the reversible T1s observed in certain *Drosophila* mutants [38]. Furthermore, the LTC distribution develops a significant bias towards tension cables as shown in Fig. 6C and Fig. 6F. Such persistent tension cables are observed in *Drosophila abl* mutants, suggesting that knockout of *abl* might impair positive tension feedback (see Discussion). Taken together, the above findings show that flow in LTC parameter space obtained from single-triangle simulations serves as a simple tool to predict the cell scale behavior (efficiency of active T1s, emergence of tension cables vs bridges) for a given tension-feedback law.

Tension-triangulation model reproduces *Drosophila* axis elongation in a simplified geometry

So far we have considered a patch of active cells with free boundary conditions. However, the epithelium of the early *Drosophila* embryo forms a closed surface that is approximately an elongated ellipsoid. Therefore, deformation of one tissue region has to be compensated by an opposite deformation of another region. For example, on the *Drosophila* embryo, the dorsal amnioserosa

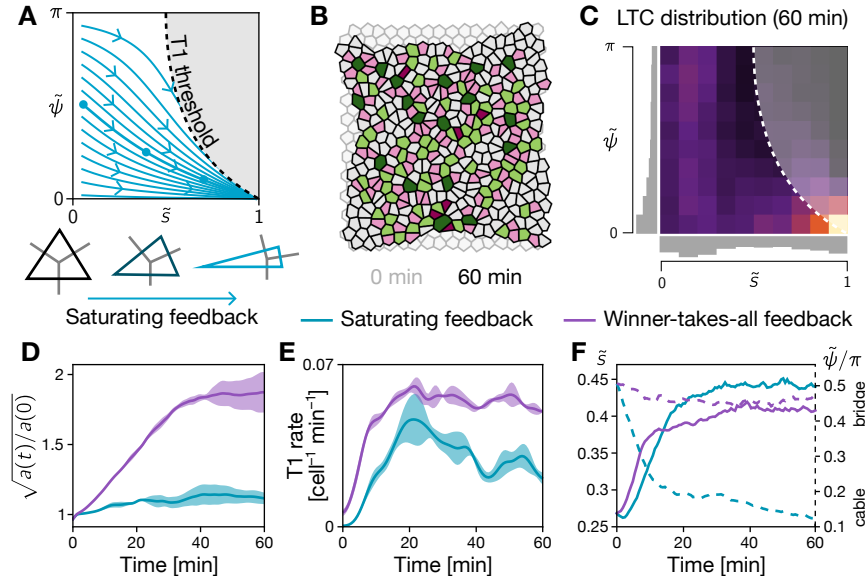


FIG. 6. Saturating tension feedback causes tension cable formation and, hence, fails to drive convergent extension. **A** Local tension configurations are driven towards tension cables due to saturation of positive feedback. Compared to winner-takes-all feedback, this resulting tension dynamics is significantly less efficient at the local configuration towards the T1 threshold (cf. Fig. 5C). **B** In a tissue simulation, saturating feedback generates only little convergent extension (quantification in D). The initial configuration is shown semi-transparent in the background. Cell color indicates coordination number (cf. Fig. 2A). **C** The late-time LTC distribution shows a strong cable bias and differs significantly from the random Delaunay distribution emerging in simulations with winner-takes-all feedback (cf. Fig. 5D). **D–F** Time series quantification showing that saturating feedback (teal), compared to winner-takes-all feedback (purple), yields very little aspect ratio change (D), a significantly reduced T1 rate (E) and a strongly increased fraction of tension cables (F). Note that in contrast to Fig. 5, the simulations were performed without an imposed isogonal strain such that no significant formation of tension bridges is observed for winner-takes-all feedback.

is passively stretched along the dorso-ventral (DV) axis and compressed along the anterior-posterior (AP) axis to compensate the convergence extension of the germ band. In the following, we investigate the interplay of active and passive tissue deformations.

To mimic the cylindrical geometry of the embryo’s trunk (Fig. 7A) we simulated a rectangular tissue patch with “slip walls” at the top and bottom boundary (Fig. 7B). Along the slip walls, cell centroids, marked by black disks, are restricted to move along the wall. These boundary conditions fix the DV extent of the tissue, corresponding to the fixed circumference of the embryo. We divide the tissue into active and passive regions to account for the different mechanical properties of the lateral ectoderm and the dorsal tissue which becomes the amnioserosa [2, 17]. (The simulation domain is symmetric with respect to reflection across the x -axis, corresponding to the left-right symmetry of the embryo.) Cortical tensions are governed by positive feedback in the active region and by tension homeostasis in the passive region. Further, passive cells (subscript p) are taken to be soft $\mu_p = 0.2\mu_a$, $\lambda_p = 0.2\lambda_a$ compared to active cells [39]. In addition, we allow interface angles in the passive region to slightly deviate from those imposed by the tension triangulation, reflecting the fact that the overall scale of cortical tensions is lower in the passive tissue [2]. We

initialize the simulation with a slightly perturbed hexagonal packing of cells (motivated by the experimental observations, see Fig. S1) and the experimentally observed tension anisotropy aligned along the DV axis [17].

Starting from this initial condition, the simulation reproduces salient features of the tissue-scale dynamics in the embryo (see Fig. 7C and Movie 4). In the active region (“lateral ectoderm”) active cell rearrangements drive tissue extension along the AP axis and contraction along the DV axis. The passive region (“amnioserosa”) is stretched along the DV axis, accommodating the fixed circumference of the embryo. Notably, this stretching leads to T1s in the passive region as is visible from the highlighted cells in Fig. 7C. On the tissue level, the coupling of active and passive regions gives rise to the tissue flow pattern characteristic of *Drosophila* germ-band elongation [2] as shown in Fig. 7E.

Tissue extension by active T1s requires large-scale mechanical patterning and cell shape elasticity

The total tissue extension found in the simulations that combine active and passive tissue regions is smaller than the extension of active tissue patches with free boundaries (compare Fig. 7D and Fig. 2C). This suggests that

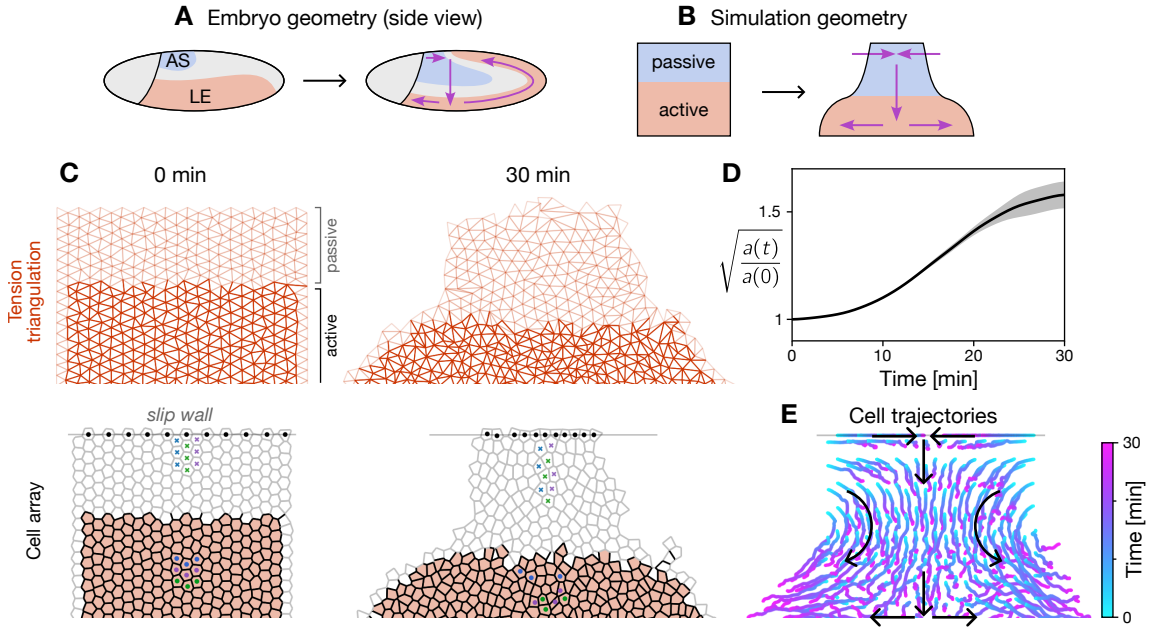


FIG. 7. Combining active and passive tissue regions. **A, B** The ellipsoidal geometry of the *Drosophila* embryo (**A**) is mimicked by a simplified simulation geometry corresponding to an unrolled cylinder (**B**), whose azimuthal axis corresponds to the dorso-ventral (vertical) axis of the embryo. The different behaviour of the dorsal amnioserosa (AS) and the lateral ectoderm (LE) tissue is represented by the passive and active region in the simulation domain respectively. **C** Positive feedback in the active region amplifies an initial DV anisotropy of tension and thus drives extension along the AP axis. Since the embryo's circumference is fixed (implemented via a slip wall at the dorsal boundary), the passive region is stretched along the DV axis. Only half of the simulation domain is shown, corresponding to one lateral side of the left-right symmetric embryo. Three-by-three patches of cells are highlighted to show cell rearrangements (cf. Movie 4). **D** Tissue deformation, as measured by the change in aspect ratio of the active region, $a(t)/a(0)$, stalls after an elongation (and perpendicular contraction) by a factor ~ 1.6 . Shading indicates standard deviation over $N = 3$ simulation runs of $N_{\text{cells}} \approx 750$ cells. **E** Trajectories of cell centroids showing the tissue scale flow, resembling the characteristic flow of *Drosophila* germ-band extension [2].

the passive tissue resists deformation. Indeed, cells in the active region are slightly elongated along the DV axis, indicating that the passive tissue pulls on them. In the following, we further investigate the role of the spatial modulation of the cells' mechanical properties along the DV axis. Figure 8A' shows a simulation without DV modulation where all cells are active. Positive tension feedback drives active T1s everywhere, as is manifest in the deformation of the tension triangulation (Fig. 8A', right). However, because of the slip-wall boundary conditions, the tissue cannot contract along the DV axis so that T1s do not result in convergence extension (see Movie 5; quantification in Fig. 8D). Instead, cell rearrangements are compensated by isogonal deformations resulting in elongated cell shapes (as quantified in Fig. 8E). We predict that this scenario will be realized in *Toll[RM9]* mutant embryos where all cells around the embryo's circumference adopt a ventro-lateral fate [33], as illustrated in the cartoon in Fig. 8A.

The stretching of cells leads to a buildup of elastic energy (see Fig. S10) which eventually leads to convergence issues in the numerical simulation for $t \gtrsim 20$ min. In *Toll[RM9]* mutant embryos, some of this elastic energy is released by the formation of folds (buckling) [33] which

our 2D simulations cannot capture. A partial compensation of cell rearrangements by cell shape changes might be observed in the germ band of mutants where the soft amnioserosa is abolished (e.g. in *dpp[hin46]* mutants).

An interesting observation from the above simulations is that the length dynamics of collapsing and emerging interfaces is not significantly affected by the lack of tissue-scale mechanical patterning (Fig. 8B), even though there is no tissue extension. Interface elongation in the absence of tissue elongation has previously been observed in experiments where germ band extension has been blocked by cauterization near the posterior pole [8, 40]. We mimic the experiments of Ref. [8] by adding slip walls to the anterior and posterior boundary of the simulated tissue (Fig. S9) to block tissue extension. In this scenario, we also observe that newly formed interfaces extend, but with a slightly different dynamics than in WT. In further agreement with experimental observations, we find that the orientation of extending interfaces is no longer biased along the AP axis when tissue extension is blocked (see Fig. 8C). Since interface extension in our model is a purely passive process, we conclude that no active mechanisms – such as medial myosin pulses [8] – are necessary for the elongation of new interfaces. Instead, interface

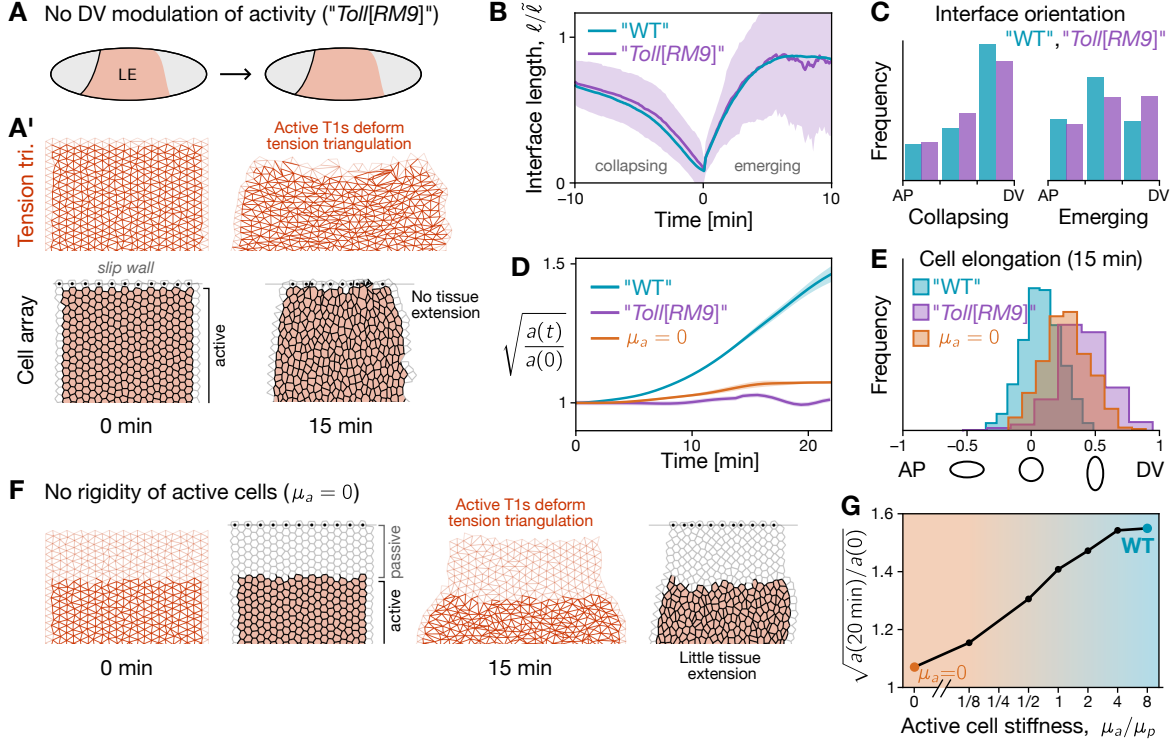


FIG. 8. Tissue flow requires cell rigidity and large-scale genetic patterning. **A** Cartoon of an embryo without dorso-ventral mechanical patterning, such as a *Toll/[[RM9]]* mutant where cells all around the circumference adopt a lateral ectoderm (LE) fate. **A'** Simulation of a tissue patch without a passive region. While active T1s deform the tension triangulation (top), the cell array (bottom) is blocked from elongating by the fixed DV “circumference” (implemented via slip walls). Instead, cell rearrangements are compensated by isogonal cell elongation (quantified in E), leading to a build-up of elastic energy. **B** The length dynamics of collapsing and emerging interfaces do not significantly depend on whether the tissue as a whole deforms (WT) or is blocked from undergoing convergent extension (no DV modulation). Purple band shows one standard deviation. Time 0 is the moment of interface collapse. **C** Orientation of collapsing and emerging interfaces showing that only the orientation of the latter is qualitatively affected by tissue-scale modulation of activity. The orientation of emerging interfaces is slightly biased along the DV direction in the absence of a passive tissue, while it is biased in AP direction in the WT case. **D** Convergent extension is strongly suppressed in absence of DV modulation of activity (“No DV”) and when active cells have vanishing shear modulus ($\mu_a = 0$; see F and G). $a(t)$ measures the aspect ratio of the active tissue region. **E** Histograms of cell shape elongation measured by relative difference, $(S_{DV,DV} - S_{AP,AP})/(S_{DV,DV} + S_{AP,AP})$, of the AP-AP and DV-DV components of the shape tensor S . In the WT case (cf. Fig. 7), cells remain nearly isotropic while they become significantly oriented along the DV axis when DV modulation of activity or rigidity of active cells are abolished. **F** When the active cells have no shear rigidity ($\mu_a = 0$), cell rearrangements are compensated by isogonal cell elongation (quantified in E) without incurring an elastic energy build-up. Thus, almost no tissue scale convergent-extension takes place. **G** Net amount of convergent extension as a function of the shear modulus of active cells shows that active cells need to be stiffer than the surrounding passive tissue for active T1s to drive efficient convergent extension.

elongation results from the fundamental temporal asymmetry of the intercalation process, i.e. the low level of active tension on the new interface (see companion paper [17]).

Rather than abolishing the DV modulation of activity, one can also change the passive elastic properties of the cells. Recall that in the model, the resistance of cells against deformations is described by the cell-shape elastic energy, Eq. (3) parameterized by the Lamé coefficients λ (resistance to area changes) and μ (resistance to shear deformation). Fig. 8F shows a simulation where the shear modulus μ_a of active cells is set to zero, so that the cells do not resist (area-preserving) elongation. Active T1s can therefore be fully compensated by cell elongation through isogonal deformations without incurring an elastic energy. As a result, there is no net tissue deformation (see Movie 5). In other words, cell-shape rigidity is required to maintain rotund cell shapes (i.e. resist isogonal shear deformations) and thus translate active T1s into net tissue deformation. The tissue deformation by isogonal modes is determined by a balance of external forces and internal resistance of cells the shape changes. Here, the external forces acting on the active tissue result from the passive tissue’s resistance to deformation, which is in turn set by shear modulus μ_p . The ratio of the shear moduli in the active vs the passive region, μ_a/μ_p , determines how much the active region deforms (see Fig. 8G). Only when the cells in the active tissue are more rigid than those in the passive region ($\mu_a/\mu_p > 1$), is it energetically favorable to isogonally deform the passive region rather than the active region. This predicts that GBE can be impaired by stiffening the dorsal tissue (amnioserosa).

DISCUSSION

We formulated a cell-scale model for epithelial tissue dynamics based on the assumptions of adiabatic force balance in the regime of dominant cortical tensions. Experimental evidence [17, 27, 41] suggests that the cortical cytoskeleton which generates this tension behaves more like a muscle, where the tension level is set by active regulation, rather than a spring, where tension is a function of length. Subscribing to these assumptions has two important consequences: First, feedback loops are required to achieve and stabilize a force-balanced configuration [13]. This is in contrast to a network of springs where the relation between length and tension (the constitutive relationship) ensures that force balance is reached by minimization of the elastic energy. Second, force balance of cortical tensions does not fully constrain the tissue as it allows for isogonal (angle-preserving) deformations which change the lengths of interfaces without changing the angles at which they meet in vertices [13]. These isogonal degrees of freedom of the cortical network are governed by non-cortical mechanical stresses, arising e.g. from passive cell elasticity, representing cell-

internal structures such as the nucleus [23, 24], microtubules, and intermediate filaments [25]. We find that this internal rigidity is essential to transduce cell intercalations into tissue-scale deformation. In the absence of cell resistance against deformation, intercalations are compensated by cell shape changes. However, if cell-internal elasticity becomes stronger than cortical tensions, it can resist changes in vertex angles and impede T1s and tissue flow (Fig. S11). Such a scenario may occur in certain genetic mutants, like the “kugelkern” (*kuk*) mutant of *Drosophila*, where the nucleus is stiffer [42]). Our findings suggest that epithelial tissue flows not like a fluid (where the shear modulus vanishes) but rather as a plastically deforming solid, whose remodeling is driven internally while resisting external forces. Epithelial tissue can thus be regarded as an *active solid*.

Our model formulates a theory of active elasticity where the dominant (cortical) stresses are not governed by constitutive relationships. It builds explicitly on the geometric relation (duality) between tension space and real space afforded by the force balance condition. Stabilizing feedback mechanisms that maintain adiabatic force balance are implicit in our model as we constrain the tension dynamics to the space of force-balanced configurations (flat tension triangulations). Dynamics in tension space is formulated in terms of the tension triangulation geometry driven by local positive feedback. This feedback amplifies a weak initial tension anisotropy and thus drives cell shape dynamics that result in cell intercalations (T1 processes). Force balance provides the non-local coupling that allows for coordination of forces and cellular behaviors across the tissue. On the tissue scale, self-organized active T1s are oriented by global tension anisotropy and thus drive convergent-extension flow. As T1s drastically remodel tension geometry, they gradually degrade the orientational cue provided by initial tension anisotropy. Thus, the locally self-organized tissue flow is generically self-limiting. It arrests after a finite extent of convergent extension that depends on the initial degree of order in the cellular packing and the magnitude of initial tension anisotropy. This central finding suggests that cell geometry is a repository of morphogenetic information that may encode the final tissue shape.

In the companion paper [17], we showed that *Drosophila* germ-band extension is driven by internally generated forces (rather than by external pulling forces). The tissue-scale model presented here – describing local mechanical self-organization of cells – provides an elegant explanation of a range of experimental observations. Supplied with the experimentally observed initial packing order and tension anisotropy our model predicts the ca. two-fold elongation two-fold elongation of the germ band. In addition, our geometrically formulated tension dynamics model can be directly compared with experimental data on the cell scale [17]. To this end, we have introduced the LTC order parameter for the local configuration of tensions. Comparing the LTC time courses between experiments and simulations, we

find excellent agreement, suggesting that our model reproduces the dynamics of germ band extension also on the cell scale. Specifically, our order parameter distinguishes two motifs of local tension configurations “tension cables” where multiple high tension interfaces meet in a vertex and “tension bridges”: high tension interfaces surrounded by low tension interfaces. Tension bridges are the elementary motif of the alternating pattern of tensions that choreographs active T1s across the tissue.

The dynamics in tension configuration space depends on the character of the positive tension feedback. Winner-takes-all feedback efficiently drives the local tension configuration toward the T1-threshold via the formation of tension bridges. By contrast, when feedback saturates at too low relative tension, it causes formation of tension cables, which have previously been suggested as a driver for convergent extension. However, our simulations and analysis of local tension configurations show that tension cables are inefficient at driving convergent extension, as adjacent interfaces “compete” to contract. Indeed, arrest of convergent extension due to the formation of tension cables is also observed in recent computational studies [10, 43]. Indeed, tension cables are often found to form at boundaries between distinct tissues and at segment boundaries where they prevent mixing between the adjacent tissues, i.e. prevent cell rearrangements [44–47].

When tension cables contract, they lead to formation of “rosettes” where five or more cells meet in a single vertex. While it has been suggested that rosettes are important for epithelial convergent extension [41, 48], recent quantitative analysis of *Drosophila* gastrulation [16, 17, 20] shows that rosettes contribute significantly less to tissue extension than T1s and appear in conjunction with disorder which causes arrest of tissue flow. Our simulations corroborate these empirical findings. In a *Drosophila* mutant for *abl*, contraction of tension cables is impaired resulting in a reduction of rosette formation [49]. By contrast, T1s appear unaffected in these mutants, suggesting that isolated high-tension junctions contract normally. Our model offers a possible explanation of this puzzling finding: Deletion of *abl* might cause the positive tension feedback to saturate earlier thus leading to the formation of persistent tension cables. This hypothesis may guide future research into the molecular role of *abl* on the regulation of the junctional cytoskeleton.

Taken together, the findings discussed above show that tension bridges are key to drive efficient convergent-extension flow. In contrast to tension cables, which clearly stand out in microscopy images (e.g. of fluorescently labelled myosin), tension bridges are hard to spot as they rapidly contract. This might be a reason why the role of tension bridges has not been appreciated before. The tension configuration parameter introduced here facilitates a statistical analysis across many cells and allows one to distinguish different local tension dynamics (e.g. winner-takes-all vs saturating feedback).

Our scenario for GBE is based on local self-organization driven by mechanical feedback. Self-organized T1s are facilitated by the initial order in the cell packing and are oriented by an initial global tension anisotropy but do not require cell-scale genetic instructions [33, 50]. We expect that the initial tension anisotropy, whose presence we confirmed experimentally in Ref. [17], is set up early on by anisotropic static “hoop” tension resulting from the internal turgor pressure in the embryo, and further reinforced by the dynamic effects of ventral furrow formation [14]. To create global tissue flow, local self-organization must be modulated by large-scale pre-patterning of cell behaviors. In the early *Drosophila* embryo, this is manifested in the dorso-ventral patterning system that specifies the tissues with different mechanical properties and modulates mechanical feedback loops [14].

In simulations on a cylindrical geometry without dorso-ventral patterning, mimicking a *Toll/RM9* mutant, active T1s occur in the absence of tissue flow. Instead, the cell rearrangements are compensated by cell shape deformations. Notably, these simulations also show that T1 resolution does not require external pulling forces or contractions of the cells’ apical area by “medial” myosin pulses [8]. Taken together, our model provides unified picture for *Drosophila* GBE that bridges the cell and tissue scales. The integration of bottom-up self-organization and top down genetic control emerges as a common theme in development [51].

Our model predicts that disrupting the hexagonal packing of nuclei prior to cellularization will cause slower GBE. Interesting candidates to test this prediction are “nuclear fallout” mutants where some nuclei leave the blastoderm surface and thus introduce defects in the cellular packing [52]. Another option might be the transient and partial disruption of microtubule organization with small molecule inhibitors [53]. We expect that these experiments can be used to challenge and subsequently refine the model.

An important challenge for future work is to identify the (molecular) mechanisms that stabilize the force-balanced configuration on short timescales while driving controlled remodeling on long timescales. In our model, maintenance of force balance implicitly enforced by maintaining a flat tension triangulation (the geometric manifestation of global force balance). This subsumes the complex regulatory feedback loops operating in the cortical cytoskeleton. The underlying mechanics of the interplay of actin fibers, myosin motors, passive crosslinkers (such as spectrins [54]) and mechanical feedback mediators (such as α -catenin [55]) remain poorly understood. We hope that the insights from the geometrical model and the quantification of local tension configurations [17] will help develop more fine-grained models that explicitly account for these details.

On the continuum level tissue flow can be described as a Stokes flow driven by an active stress field that captures the coarse grained distribution of myosin mo-

tors [1, 2, 56, 57]. Coupling of the active stress fields to the flow (by advection and flow alignment) generically gives rise to long-wavelength spontaneous flow instabilities [58–60] and active nematic turbulence [61]. Notably, we do not observe such an instability in our model. Instead, we find that tissue flow driven by local mechanical self-organization of cells is generically self-limiting due to the rapid loss of cell-scale order as cells rearrange. A similar “short-wavelength instability” is found in another recently model for self-organized T1s [10]. It is not captured by existing continuum models, suggesting that additional order parameters (such as the hexagon fraction and the LTC order parameter introduced here) will need to be taken into account. Interestingly, several biological systems exhibit persistent convergence–extension flows [62, 63] that appear to overcome the self-limiting nature of a locally self-organized mechanism. Such persistent flows may be accounted for by coupling tension

dynamics to external fields [64] representing guiding cues such as planar cell polarity [65]. Overall, we anticipate that translating the intimate geometric relation between tension space triangulation and physical cell-array to the continuum level will be a fruitful direction for future research.

ACKNOWLEDGMENTS

We thank Arthur Hernandez, Matthew Lefebvre, Noah Mitchell, Sebastian Streichan, and Eric Wieschaus for stimulating discussions and careful reading of the manuscript. We further thank Dinah Loerke and Jennifer Zallen for insightful feedback. FB acknowledges support of the GBMF post-doctoral fellowship (under grant #2919). NHC was supported by NIGMS R35-GM138203 and NSF PHY:1707973. BIS acknowledges support via NSF PHY:1707973 and NSF PHY:2210612.

-
- [1] G. F. Oster, J. D. Murray, and A. K. Harris, Mechanical aspects of mesenchymal morphogenesis, *Development* **78**, 83 (1983).
 - [2] S. J. Streichan, M. F. Lefebvre, N. Noll, E. F. Wieschaus, and B. I. Shraiman, Global morphogenetic flow is accurately predicted by the spatial distribution of myosin motors, *eLife* **7**, e27454 (2018).
 - [3] M. Saadaoui, D. Rocancourt, J. Roussel, F. Corson, and J. Gros, A tensile ring drives tissue flows to shape the gastrulating amniote embryo, *Science* **367**, 453 (2020).
 - [4] A. Iorati-Uba, T. B. Liverpool, and S. Henkes, Mechano-chemical active feedback generates convergence extension in epithelial tissue, *arXiv*, arXiv:2303.02109 (2023).
 - [5] W. Kong, O. Loison, P. Chavadimane Shivakumar, E. H. Chan, M. Saadaoui, C. Collinet, P.-F. Lenne, and R. Clément, Experimental validation of force inference in epithelia from cell to tissue scale, *Scientific Reports* **9**, 14647 (2019).
 - [6] M. Weliky and G. Oster, The mechanical basis of cell rearrangement I. Epithelial morphogenesis during *Fundulus* epiboly, *Development* **109**, 373 (1990).
 - [7] R. Farhadifar, J.-C. Röper, B. Aigouy, S. Eaton, and F. Jülicher, The Influence of Cell Mechanics, Cell-Cell Interactions, and Proliferation on Epithelial Packing, *Current Biology* **17**, 2095 (2007).
 - [8] C. Collinet, M. Rauzi, P.-F. Lenne, and T. Lecuit, Local and tissue-scale forces drive oriented junction growth during tissue extension, *Nature Cell Biology* **17**, 1247 (2015).
 - [9] C. Duclut, J. Pajmans, M. M. Inamdar, C. D. Modes, and F. Jülicher, Active T1 transitions in cellular networks, *The European Physical Journal E* **45**, 29 (2022).
 - [10] R. Sknepnek, I. Djafer-Cherif, M. Chuai, C. Weijer, and S. Henkes, Generating active T1 transitions through mechanochemical feedback, *eLife* **12**, e79862 (2023).
 - [11] I. Bonnet, P. Marcq, F. Bosveld, L. Fetler, Y. Bellaïche, and F. Graner, Mechanical state, material properties and continuous description of an epithelial tissue, *Journal of The Royal Society Interface* **9**, 2614 (2012).
 - [12] N. Noll, S. J. Streichan, and B. I. Shraiman, Variational Method for Image-Based Inference of Internal Stress in Epithelial Tissues, *Physical Review X* **10**, 011072 (2020).
 - [13] N. Noll, M. Mani, I. Heemskerk, S. J. Streichan, and B. I. Shraiman, Active tension network model suggests an exotic mechanical state realized in epithelial tissues, *Nature Physics* **13**, 1221 (2017).
 - [14] H. J. Gustafson, N. Claussen, S. De Renzis, and S. J. Streichan, Patterned mechanical feedback establishes a global myosin gradient, *bioRxiv*, doi:10.1101/2021.12.06.471321 (2021).
 - [15] J. Byrne, *Neuroscience Online: An Electronic Textbook for the Neurosciences* (Department of Neurobiology and Anatomy McGovern Medical School at The University of Texas Health Science Center at Houston, Houston, TX, 1997).
 - [16] T. Stern, S. Y. Shvartsman, and E. F. Wieschaus, Deconstructing gastrulation at single-cell resolution, *Current Biology* **32**, 1861 (2022).
 - [17] F. Brauns, N. H. Claussen, E. F. Wieschaus, and B. I. Shraiman, The Geometric Basis of Epithelial Convergent Extension, *eLife* **10.7554/eLife.95521.1** (2024).
 - [18] S. Münster, A. Jain, A. Mietke, A. Pavlopoulos, S. W. Grill, and P. Tomancak, Attachment of the blastoderm to the vitelline envelope affects gastrulation of insects, *Nature* **568**, 395 (2019).
 - [19] D. Kunz, A. Wang, C. U. Chan, R. H. Pritchard, W. Wang, F. Gallo, C. R. Bradshaw, E. Terenzani, K. H. Müller, Y. Y. S. Huang, and F. Xiong, Downregulation of extraembryonic tension controls body axis formation in avian embryos, *Nature Communications* **14**, 3266 (2023).
 - [20] D. L. Farrell, O. Weitz, M. O. Magnasco, and J. A. Zallen, SEGGA: A toolset for rapid automated analysis of epithelial cell polarity and dynamics, *Development* **144**, 1725 (2017).
 - [21] O. E. Jensen, E. Johns, and S. Woolner, Force networks, torque balance and Airy stress in the planar vertex model of a confluent epithelium, *Proceedings of the Royal Soci-*

- ety A: Mathematical, Physical and Engineering Sciences **476**, 20190716 (2020).
- [22] J. C. Maxwell, On reciprocal figures and diagrams of forces, *The London, Edinburgh, and Dublin Philosophical Magazine and Journal of Science* **27**, 250 (1864).
 - [23] S. Grosser, J. Lippoldt, L. Oswald, M. Merkel, D. M. Sussman, F. Renner, P. Gottheil, E. W. Morawetz, T. Fuhs, X. Xie, S. Pawlizak, A. W. Fritsch, B. Wolf, L.-C. Horn, S. Briest, B. Aktas, M. L. Manning, and J. A. Käs, Cell and Nucleus Shape as an Indicator of Tissue Fluidity in Carcinoma, *Physical Review X* **11**, 011033 (2021).
 - [24] S. Kim, R. Amini, and O. Campàs, *A nuclear jamming transition in vertebrate organogenesis* (2022).
 - [25] M. Pensalfini, T. Golde, X. Trepát, and M. Arroyo, Nonaffine Mechanics of Entangled Networks Inspired by Intermediate Filaments, *Physical Review Letters* **131**, 058101 (2023).
 - [26] S. Wohlrab, S. Mueller, and S. Gekle, Mechanical complexity of living cells can be mapped onto simple homogeneous equivalents, *Biomechanics and Modeling in Mechanobiology* [10.1007/s10237-024-01823-9](https://doi.org/10.1007/s10237-024-01823-9) (2024).
 - [27] R. Fernandez-Gonzalez, S. d. M. Simoes, J.-C. Röper, S. Eaton, and J. A. Zallen, Myosin II Dynamics Are Regulated by Tension in Intercalating Cells, *Developmental Cell* **17**, 736 (2009).
 - [28] G. Odell, G. Oster, P. Alberch, and B. Burnside, The mechanical basis of morphogenesis, *Developmental Biology* **85**, 446 (1981).
 - [29] D. Bi, J. H. Lopez, J. M. Schwarz, and M. L. Manning, A density-independent rigidity transition in biological tissues, *Nature Physics* **11**, 1074 (2015).
 - [30] L. Hufnagel, A. A. Teleman, H. Rouault, S. M. Cohen, and B. I. Shraiman, On the mechanism of wing size determination in fly development, *Proceedings of the National Academy of Sciences* **104**, 3835 (2007).
 - [31] E. P. Bernard, W. Krauth, and D. B. Wilson, Event-chain Monte Carlo algorithms for hard-sphere systems, *Physical Review E* **80**, 056704 (2009).
 - [32] B. Li, Y. Nishikawa, P. Höllmer, L. Carillo, A. C. Maggs, and W. Krauth, Hard-disk pressure computations—a historic perspective, *The Journal of Chemical Physics* **157**, 234111 (2022).
 - [33] K. Irvine and E. Wieschaus, Cell intercalation during *Drosophila* germband extension and its regulation by pair-rule segmentation genes, *Development* **120**, 827 (1994).
 - [34] B. He, A. Martin, and E. Wieschaus, Flow-dependent myosin recruitment during *Drosophila* cellularization requires zygotic *dunk* activity, *Development*, dev.131334 (2016).
 - [35] S. Dutta, N. J.-V. Djabrayan, S. Torquato, S. Y. Shvartsman, and M. Krajnc, Self-Similar Dynamics of Nuclear Packing in the Early *Drosophila* Embryo, *Biophysical Journal* **117**, 743 (2019).
 - [36] M. Merkel, R. Etournay, M. Popović, G. Salbreux, S. Eaton, and F. Jülicher, Triangles bridge the scales: Quantifying cellular contributions to tissue deformation, *Physical Review E* **95**, 032401 (2017).
 - [37] K. Taniguchi, R. Maeda, T. Ando, T. Okumura, N. Nakazawa, R. Hatori, M. Nakamura, S. Hozumi, H. Fujiwara, and K. Matsuno, Chirality in Planar Cell Shape Contributes to Left-Right Asymmetric Epithelial Morphogenesis, *Science* **333**, 339 (2011).
 - [38] P.-L. Bardet, B. Guirao, C. Paoletti, F. Serman, V. Léopold, F. Bosveld, Y. Goya, V. Mirouse, F. Graner, and Y. Bellaïche, PTEN Controls Junction Lengthening and Stability during Cell Rearrangement in Epithelial Tissue, *Developmental Cell* **25**, 534 (2013).
 - [39] M. Rauzi, U. Krzic, T. E. Saunders, M. Krajnc, P. Ziherl, L. Hufnagel, and M. Leptin, Embryo-scale tissue mechanics during *Drosophila* gastrulation movements, *Nature Communications* **6**, 8677 (2015).
 - [40] M. Rauzi, Probing tissue interaction with laser-based cauterization in the early developing *Drosophila* embryo, in *Methods in Cell Biology*, Vol. 139 (Elsevier, 2017) pp. 153–165.
 - [41] J. T. Blankenship, S. T. Backovic, J. S. Sanny, O. Weitz, and J. A. Zallen, Multicellular Rosette Formation Links Planar Cell Polarity to Tissue Morphogenesis, *Developmental Cell* **11**, 459 (2006).
 - [42] A. Brandt, F. Papagiannouli, N. Wagner, M. Wilsch-Bräuninger, M. Braun, E. E. Furlong, S. Loserth, C. Wenzl, F. Pilot, N. Vogt, T. Lecuit, G. Krohne, and J. Großhans, Developmental Control of Nuclear Size and Shape by kugelkern and kurzern, *Current Biology* **16**, 543 (2006).
 - [43] J. Rozman, J. M. Yeomans, and R. Sknepnek, Shape-Tension Coupling Produces Nematic Order in an Epithelium Vertex Model, *Physical Review Letters* **131**, 228301 (2023).
 - [44] K. P. Landsberg, R. Farhadifar, J. Ranft, D. Umetzu, T. J. Widmann, T. Bittig, A. Said, F. Jülicher, and C. Dahmann, Increased Cell Bond Tension Governs Cell Sorting at the *Drosophila* Anteroposterior Compartment Boundary, *Current Biology* **19**, 1950 (2009).
 - [45] S. Calzolari, J. Terriente, and C. Pujades, Cell segregation in the vertebrate hindbrain relies on actomyosin cables located at the interhombomeric boundaries, *The EMBO Journal* **33**, 686 (2014).
 - [46] J. C. Yu, N. Balaghi, G. Erdemci-Tandogan, V. Castle, and R. Fernandez-Gonzalez, Myosin cables control the timing of tissue internalization in the *Drosophila* embryo, *Cells & Development* **168**, 203721 (2021).
 - [47] D. J. Ashour, C. H. Durney, V. J. Planelles-Herrero, T. J. Stevens, J. J. Feng, and K. Röper, Zasp52 strengthens whole embryo tissue integrity through supracellular actomyosin networks, *Development* **150**, dev201238 (2023).
 - [48] S. S. Lienkamp, K. Liu, C. M. Karner, T. J. Carroll, O. Ronneberger, J. B. Wallingford, and G. Walz, Vertebrate kidney tubules elongate using a planar cell polarity-dependent, rosette-based mechanism of convergent extension, *Nature Genetics* **44**, 1382 (2012).
 - [49] M. Tamada, D. L. Farrell, and J. A. Zallen, Abl Regulates Planar Polarized Junctional Dynamics through β -Catenin Tyrosine Phosphorylation, *Developmental Cell* **22**, 309 (2012).
 - [50] A. C. Paré, A. Vichas, C. T. Fincher, Z. Mirman, D. L. Farrell, A. Mainieri, and J. A. Zallen, A positional Toll receptor code directs convergent extension in *Drosophila*, *Nature* **515**, 523 (2014).
 - [51] F. Schweisguth and F. Corson, Self-Organization in Pattern Formation, *Developmental Cell* **49**, 659 (2019).
 - [52] W. F. Rothwell, P. Fogarty, C. M. Field, and W. Sullivan, Nuclear-fallout, a *Drosophila* protein that cycles from the cytoplasm to the centrosomes, regulates cortical microfilament organization, *Development* **125**, 1295 (1998).

- [53] T. Kanesaki, C. M. Edwards, U. S. Schwarz, and J. Grosshans, Dynamic ordering of nuclei in syncytial embryos: A quantitative analysis of the role of cytoskeletal networks, *Integrative Biology* **3**, 1112 (2011).
- [54] D. Krueger, C. Pallares Cartes, T. Makaske, and S. De Renzis, β H-spectrin is required for ratcheting apical pulsatile constrictions during tissue invagination, *EMBO reports* **21**, e49858 (2020).
- [55] C. Rauskolb, E. Cervantes, F. Madere, and K. D. Irvine, Organization and function of tension-dependent complexes at adherens junctions, *Journal of Cell Science*, jcs.224063 (2019).
- [56] P. Caldarelli, A. Chamolly, O. Alegria-Prévot, J. Gros, and F. Corson, Self-organized tissue mechanics underlie embryonic regulation, *bioRxiv*, doi:10.1101/2021.10.08.463661 (2021).
- [57] M. Serra, G. Serrano Nájera, M. Chuai, A. M. Plum, S. Santhosh, V. Spandan, C. J. Weijer, and L. Mahadevan, A mechanochemical model recapitulates distinct vertebrate gastrulation modes, *Science Advances* **9**, eadh8152 (2023).
- [58] R. Aditi Simha and S. Ramaswamy, Hydrodynamic Fluctuations and Instabilities in Ordered Suspensions of Self-Propelled Particles, *Physical Review Letters* **89**, 058101 (2002).
- [59] R. Voituriez, J. F. Joanny, and J. Prost, Spontaneous flow transition in active polar gels, *Europhysics Letters (EPL)* **70**, 404 (2005).
- [60] M. C. Marchetti, J. F. Joanny, S. Ramaswamy, T. B. Liverpool, J. Prost, M. Rao, and R. A. Simha, Hydrodynamics of soft active matter, *Reviews of Modern Physics* **85**, 1143 (2013).
- [61] R. Alert, J. Casademunt, and J.-F. Joanny, Active Turbulence, *Annual Review of Condensed Matter Physics* **13**, 143 (2022).
- [62] O. Voiculescu, F. Bertocchini, L. Wolpert, R. E. Keller, and C. D. Stern, The amniote primitive streak is defined by epithelial cell intercalation before gastrulation, *Nature* **449**, 1049 (2007).
- [63] R. J. Huebner and J. B. Wallingford, Coming to Consensus: A Unifying Model Emerges for Convergent Extension, *Developmental Cell* **46**, 389 (2018).
- [64] M. Ibrahimi and M. Merkel, Deforming polar active matter in a scalar field gradient, *New Journal of Physics* **25**, 013022 (2023).
- [65] R. J. Huebner and J. B. Wallingford, Coming to Consensus: A Unifying Model Emerges for Convergent Extension, *Developmental Cell* **46**, 389 (2018).
- [66] J. Feder, Random sequential adsorption, *Journal of Theoretical Biology* **87**, 237 (1980).
- [67] J. Ginibre, Statistical Ensembles of Complex, Quaternion, and Real Matrices, *Journal of Mathematical Physics* **6**, 440 (1965).
- [68] B. I. Halperin and D. R. Nelson, Theory of Two-Dimensional Melting, *Physical Review Letters* **41**, 121 (1978).
- [69] J. A. Zallen and R. Zallen, Cell-pattern disordering during convergent extension in *Drosophila*, *Journal of Physics: Condensed Matter* **16**, S5073 (2004).
- [70] J.-M. Armengol-Collado, L. N. Carenza, J. Eckert, D. Krommydas, and L. Giomi, Epithelia are multiscale active liquid crystals, *arXiv*, arXiv:2202.00668 (2022).
- [71] M. F. Lefebvre, N. H. Claussen, N. P. Mitchell, H. J. Gustafson, and S. J. Streichan, Geometric control of myosin II orientation during axis elongation, *eLife* **12**, e78787 (2023).
- [72] P. Virtanen et al., SciPy 1.0: Fundamental algorithms for scientific computing in Python, *Nature Methods* **17**, 261 (2020).
- [73] G. R. Kale, X. Yang, J.-M. Philippe, M. Mani, P.-F. Lenne, and T. Lecuit, Distinct contributions of tensile and shear stress on E-cadherin levels during morphogenesis, *Nature Communications* **9**, 5021 (2018).
- [74] S. Marschner and P. Shirley, *Fundamentals of Computer Graphics*, 4th ed. (A K Peters/CRC Press, 2018).
- [75] N. Van Kampen, Elimination of fast variables, *Physics Reports* **124**, 69 (1985).
- [76] J. Bradbury, R. Frostig, P. Hawkins, M. J. Johnson, C. Leary, D. Maclaurin, G. Necula, A. Paszke, J. VanderPlas, S. Wanderman-Milne, and Q. Zhang, *JAX: Composable transformations of Python+NumPy programs* (2018).

SUPPLEMENTARY MATERIAL

1. ANALYSIS OF EXPERIMENTAL DATA

1.1. Experimental data source

Whole embryo cell segmentation and tracking data was obtained from the repository [DOI:10.6084/m9.figshare.18551420.v3](https://doi.org/10.6084/m9.figshare.18551420.v3) deposited with Ref. [16]. We analyzed the dataset with ID number 1620 since it had the highest time resolution (15 s) and covered the longest time period (50 min), starting ca. 7 min before the onset of ventral furrow invagination.

1.2. Hexagonal packing and hexatic order

We quantify order of the cell arrangement in the tissue by two measures: (i) the fraction of six-sided cells, that one might loosely call “hexagonal packing order” and (ii) the hexatic order parameter measuring bond-orientational order. Hexagonal packing order is a topological quantity: it depends only on the neighborhood relations between cells but not on their exact shape. In contrast, hexatic order (defined below) is a geometric measure, that is sensitive to the cell shapes. Initially, the majority of cells have six neighbors (Fig. S1A, 0 min), and the density of topological defects, manifested as non-hexagonal cells, is relatively low. During VF invagination, the number of defects increases only slightly (25 min) since there are only very few intercalations [17]. During GBE, the number of defects increases significantly as a consequence of T1s. Towards the end of GBE, the distribution of cell-coordination number approaches that of a random Voronoi tessellation seeded with a Ginibre random point process (see Fig. S1B and B’).

Hexatic order. The hexatic order parameter (also called “bond orientational order parameter” [68]) for a cell with n vertices is defined as

$$\psi_6 = \frac{1}{n} \sum_{k=1}^n \exp(6i\theta_k), \quad (\text{S1})$$

where θ_k is the angle between the DV axis and the vector pointing from the cell’s centroid to vertex k . For a cell with regular hexagonal shape the magnitude of ψ_6 reaches its maximum $|\psi_6| = 1$. The phase $\arg \psi_6$ indicates the orientation of the hexagon. In contrast to the coordination number, which is a purely topological measure, the hexatic order parameter depends on the cell shape. In line with previous findings from confocal microscopy of the *Drosophila* germ band [69], we find that the hexatic order parameter to be low in magnitude and exhibit no long-range correlations as is apparent from Fig. S1C. Effectively, the presence of non-hexagonal cells act as obstructions to long range correlations of geometric order. We quantify the range of correlations in hexatic order by coarse graining over patches of cells with different radii (measured in the by the neighborhood degree). Before the onset of GBE, the coarse grained order parameter decays as a power law of the patch radius law with an exponent that close to -0.75 , a value found also for MDCK cells and in simulations using multiphase-field models [70]. (We find the same result using the distance-weighted hexatic order parameter introduced in Ref. [70].) At the end of GBE, the decay exponent is smaller than -1 , indicating a complete lack of correlations in hexatic order between neighboring cells. This is expected from the high number of non-hexagonal cells at this stage (Fig. S1B, 50 min).

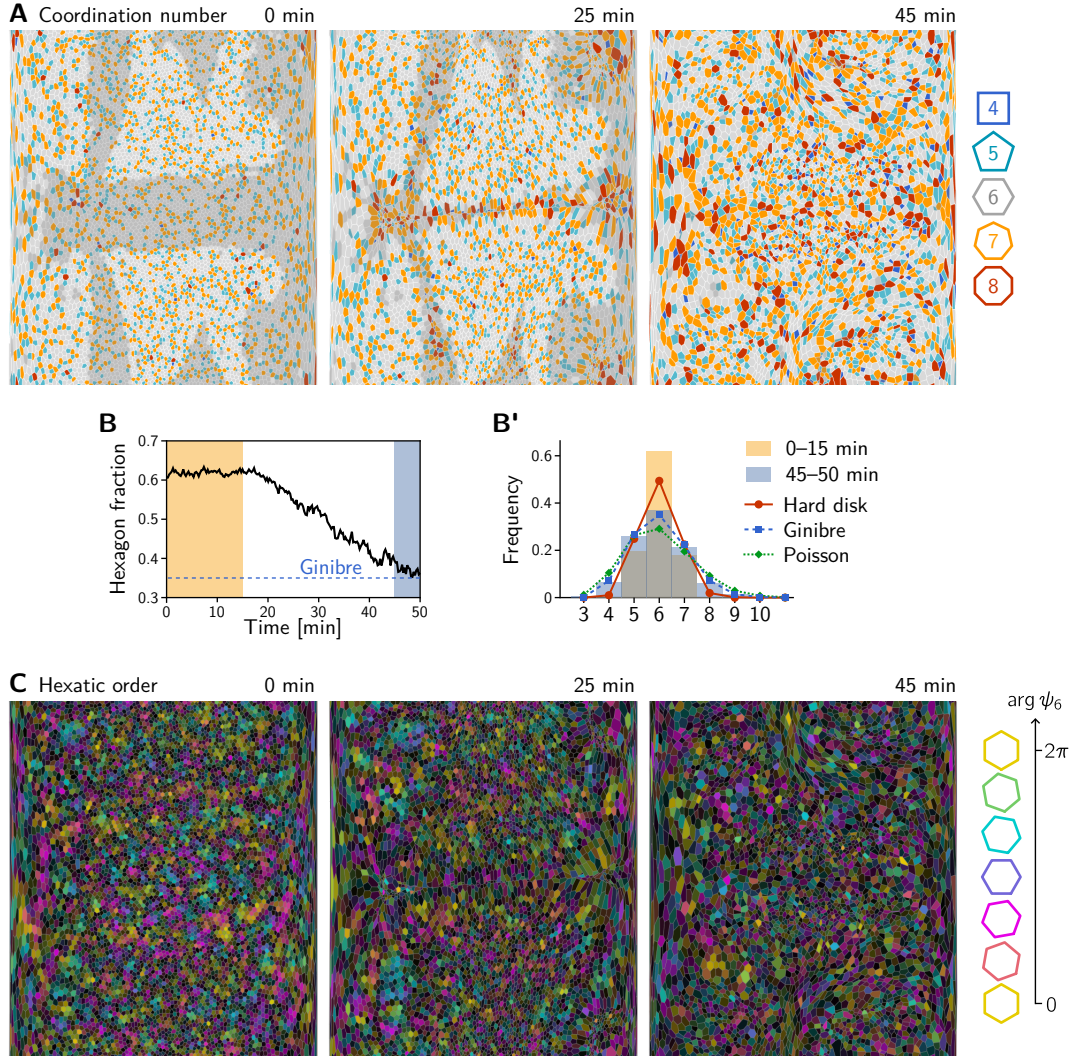


FIG. S1. Coordination number and hexatic order of cells. **A** Initially (0 min), the majority of cells are hexagonal (light gray). During GBE (25–50 min), topological defects proliferate, resulting in increasing numbers of non-hexagonal cells. Semitransparent gray overlay marks cells that invaginate. **B** and **B'** Fraction of hexagonal cells as a function of time (**B**) and histogram of cell-coordination number (**B'**) in the lateral ectoderm. The histograms show pooled data from the time periods 0–15 min and 45–50 min highlighted in **B**. Lines indicate the coordination number distributions for Voronoi tessellations generated from three different random point processes: hard disk (packing fraction 0.54 near the theoretical maximum for sequential placement [66]), Ginibre [67], and Poisson. **C** Hexatic order is low, and shows no long-range correlation. It further decreases as GBE progresses. Hue and brightness code for the phase ($\arg \psi_6$) and magnitude ($|\psi_6|$) of the hexatic order parameter, respectively.

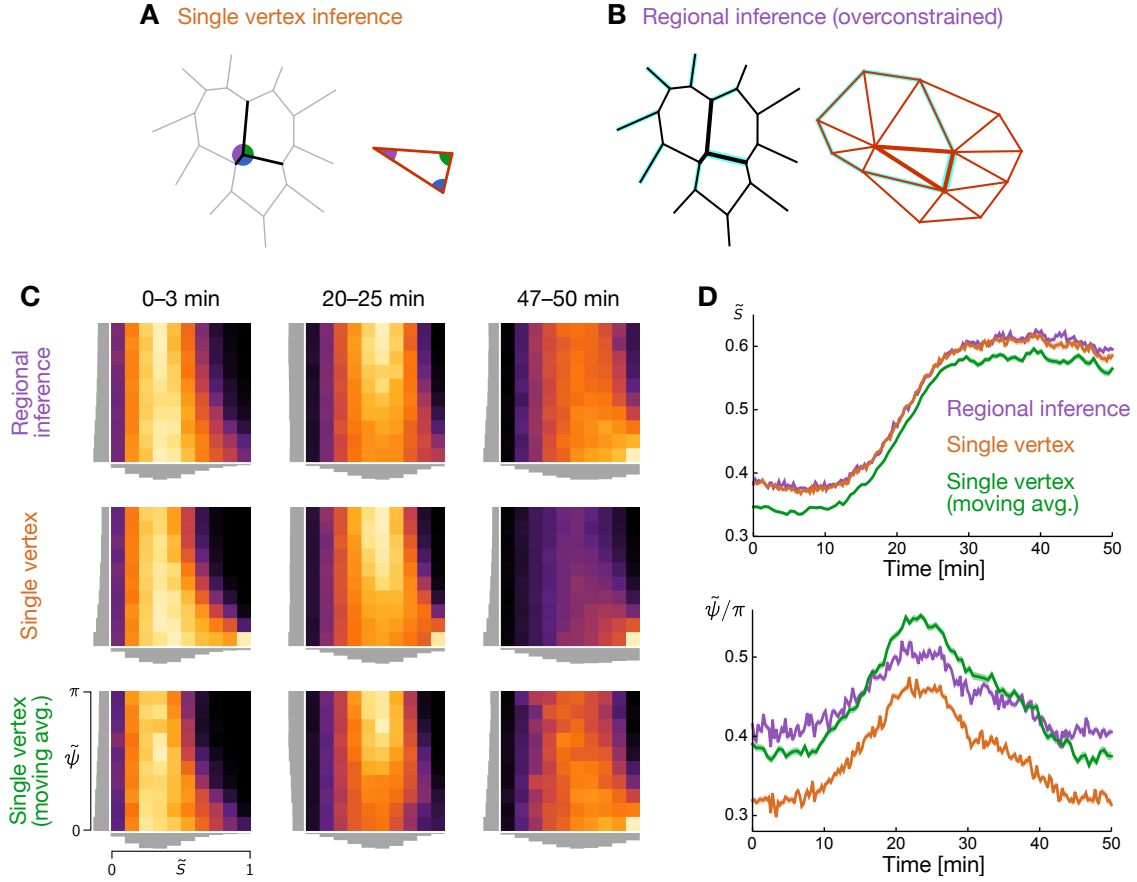


FIG. S2. Comparison of local vs regional tension inference. **A** Local tension inference at a single vertex through complementarity of angles at a single vertex (left) and in the corresponding tension triangle (right). The relative tensions (edge lengths of the tension triangle) are found via the law of sines. **B** Regional tension inference for a patch of three cells. The interfaces (and corresponding tensions) shared between them are highlighted by bold lines. The triangulation property of the tensions yields one additional constraint for each cell because for each cell there is a loop in the tension triangulation which has to close. One such loop is highlighted. These additional constraints make the regional inference more robust. **C** Comparison of the LTC distributions for regional and local tension inference in the *Drosophila* germ band. Distributions are from data collected over the indicated time intervals. Germ band elongation starts at ca. 25 min. The last row shows single-vertex inference based on vertex positions smoothed using a moving average (1.25 min interval). **D** Mean anisotropy magnitude (top) and LTC phase (bottom) for the three inference variants. Note the systematically lower LTC phase, i.e. lower fraction of tension bridges, found using single-vertex inference.

1.3. Local and regional tension inference

To quantify the local tension configurations in experimental data from the *Drosophila* germ band, we performed tension inference based on segmented cell outlines. In the companion paper [17], tension inference was done locally, directly relating the angles at each vertex to the relative cortical

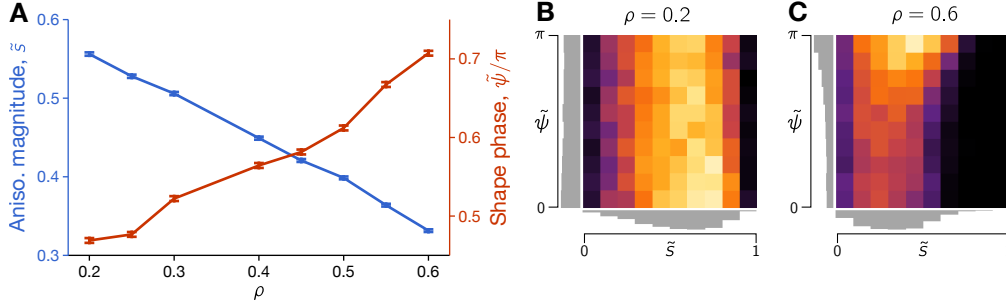


FIG. S3. LTC distribution for the hard-disk Delaunay family of random triangulation. **A** Median LTC parameter magnitude and phase vs hard disk packing fraction. **B**, **C** LTC histograms for two different packing fractions shows significant differences in the LTC distribution for different ρ . Note that topological statistics such as coordination numbers are much less sensitive to ρ . LTC distributions computed from cell arrays with 4000 cells.

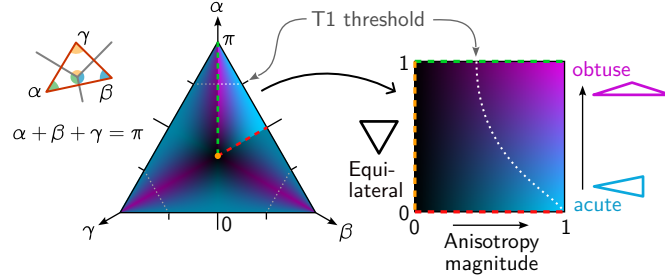


FIG. S4. Illustration of LTC parameters as a function of internal triangle angles. The three angles α, β, γ of a triangle lie in a simplex defined by $\alpha, \beta, \gamma \geq 0$ and $\alpha + \beta + \gamma = \pi$. The simplex has a 6-fold symmetry due to permutations of the angles; its fundamental domain is mapped into the LTC space formed by $\tilde{s}, \tilde{\psi}$ defined in Eq. (8). The Delaunay threshold $\max\{\alpha, \beta, \gamma\} \leq \pi$ is indicated in gray.

tension via the law of sines (see Fig. S2A). While this method is conceptually and computationally simple, it is sensitive to observational and dynamical noise in the angles. A more robust approach is to perform tension inference in an extended region, which makes the inference problem overconstrained [13]. In particular, there is one additional constraint per cell because the tension triangles for each cell have to fit together in force balance as illustrated in Fig. S2B. The overconstrained inference returns tensions for the closest force-balanced configuration compatible with the observed angles and thus removes small deviations from tensional force balance due to pressure differentials, short-time fluctuations, and observational noise. (An alternative method to remove observational noise is to apply a moving average on the vertex positions before inferring tensions.) Since in our model cortical tensions are always in exact tensional force balance, we use this overconstrained inference to compare to simulations. Specifically, we use tension inference on all interfaces of the three cells which meet at a given vertex to determine the local tension configuration parameter at that vertex. Figure S2C shows the LTC distributions obtained from local and regional inference. The LTC distributions are qualitatively very similar but they differ quantitatively. In particular, the LTC phase $\tilde{\psi}$ has the same qualitative trend with a transient increase before the onset of T1s but is systematically lower for regional inference.

2. ADDITIONAL SIMULATION RESULTS

In this section we report additional results from the tissue scale simulations and/or explain implementation details.

2.1. Influence of isogonal stretching on the LTC distribution

Here, we consider the influence of the reference cell shape S_0 which determines the isogonal potential via the elastic energy. As discussed in the main text, isogonally stretching or compressing cells along the axis of tension anisotropy can delay or accelerate TIs by moving the T1-threshold in LTC space. As reported in the main text, if we implement isogonal stretching by choosing an anisotropic S_0 , i.e. $S_0 = 3\ell_0 \text{diag}(1-t, 1+t)$, $t \in [0, 1]$, we find that a higher bridge bias emerges at the early phase of convergent extension (Fig. 5). We chose an anisotropic reference shape $t = 1/3$ to model the isogonal stretching caused by the ventral furrow before onset of GBE. In the experimental data, this isogonal stretch decays; analogously, we linearly ramp the reference shape anisotropy down so that $t = 0$ at 50 minutes simulation time. We note that our modelling of isogonal stretching is limited, since it is encoded in a model parameter (S_0) instead of being created dynamically, for example by external forces applied to the boundary. Time traces of the LTC parameter in the absence of isogonal stretching are shown in Fig. S8) below.

2.2. Alternative forms of positive tension feedback

We now turn to discussing two variants of the triangle-intrinsic tension dynamics. In the main text, we discussed two types of positive feedback, saturating and winner-takes-all. In both cases, the overall scale of tensions was determined by keeping the triangle perimeter $P = \sum_{\alpha \in I_{ijk}} \tilde{T}_\alpha$ constant. This corresponds to a fixed amount of total active tension that is only redistributed across edges. We can also consider a model where the triangle area remains fixed. This can be implemented using the gradient $(J_A)_{ij} = \partial_{\tilde{T}_{ij}} A_{I_{ijk}}$ of the triangle area with respect to the triangle side lengths:

$$\partial_t \tilde{T}_{ij} = \tau_T^{-1} \left(\tilde{T}_{ij}^n - \frac{1}{\sqrt{\sum_{\alpha \in I_{ijk}} (\partial_{\tilde{T}_\alpha} A_{I_{ijk}})^2}} \sum_{\alpha \in I_{ijk}} (\partial_{\tilde{T}_\alpha} A_{I_{ijk}} \tilde{T}_\alpha^n) \right) \quad (\text{S2})$$

The overall dynamics of this model is very similar to Eq. (5) considered in the main text. However, the tension feedback is “more aggressive” since now the total tension (triangle perimeter) increases as the tension triangle becomes more anisotropic. This mirrors a situation where in addition to the anisotropy also the total myosin levels increase during GBE [71]. Therefore, one observes slightly larger amounts of convergent extension for identical initial conditions.

Next, we considered adding small amounts of i.i.d. Gaussian noise to the cortical tension dynamics, i.e. a stochastic, Langevin tension evolution

$$\tau_T \partial_t \tilde{T}_{ij} = \tilde{T}_{ij}^n - \frac{1}{3} \sum_{\alpha \in I_{ijk}} \tilde{T}_\alpha^n + \eta_{ij}, \quad (\text{S3})$$

$$\text{with } \eta_{ij} \sim \text{i.i.d. Normal}(0, \sigma^2) \text{ and } \langle \eta_{ij}(t) \eta_{kl}(t') \rangle = \sigma^2 \delta(t - t') \delta_{ij,kl} \quad (\text{S4})$$

To integrate Eq. (S3), we use the explicit Euler-Maruyama scheme. We find that the convergent extension phenomenology is robust to low to moderate levels of noise (i.e. $\sigma < T_{ij}^n$). However, higher

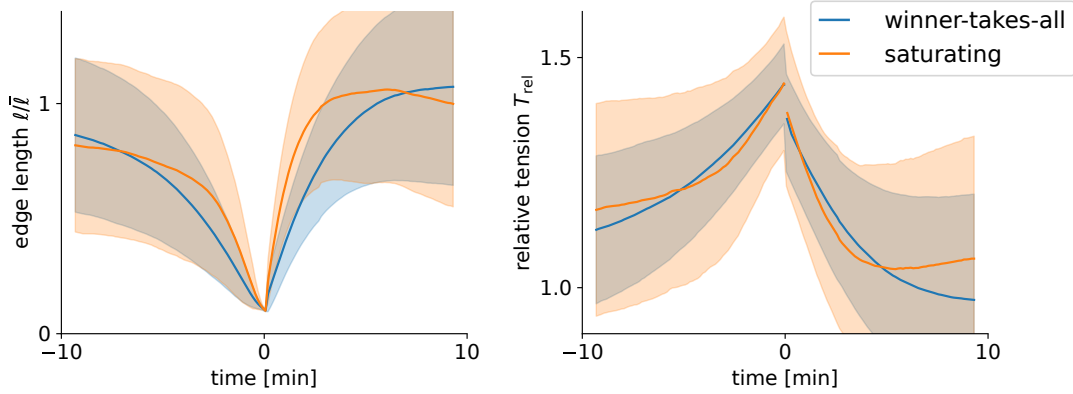


FIG. S5. Tension and length dynamics of of intercalating interface for T1 events in winner-takes-all and saturating feedback simulations. Shaded area indicates standard deviations. Time $t = 0$ min indicates the moment of T1 transition. Winner-takes-all feedback matches the corresponding experimental data well (see the companion paper [17]), while saturating feedback does not, featuring a rapid instead of gradual collapse and reemergence of interfaces. Interface length is measured relative to the average interface length \bar{l} . T1s occur at a non-zero length due to a numerical cutoff.

σ leads to a final LTC distribution with somewhat more anisotropic triangles, indicating larger disorder, and reduces the amount of total convergent extension.

Cell arrays from a Langevin simulation and from a simulation with an area-based myosin pool mechanism are shown in Fig. S6. A quantitative analysis is shown in Fig. S8.

2.3. Saturating tension feedback

Here, we present the details for the simulations of saturating tension feedback in main text Fig. 5. We consider bistable tension dynamics of the form

$$\tau_T \frac{d}{dt} \dot{T} = -(T - T_-)(T - T_c)(T - T_+) \quad (\text{S5})$$

where $T_- < T_c < T_+$ are the low, unstable, and high tension fixed point, respectively. We set $T_- = 0$, $T_c = 1$ matching the fixed points of the main feedback model Eq. (5) we consider in this manuscript. The simulations with saturating feedback correspond to $T_+ = 1.2$, the control simulations are $T_+ = 3.33$. Note that we adjusted the time step and all other rate parameters of the simulation so that \dot{T} is similar across different choices of T_+ .

Irreversible and reversible T1 transitions. We note that in the case of saturating tension feedback, a relevant fraction of T1s (approx. 20%) are reversible, i.e. the newly formed junction re-collapses, which occurs in less than 1% of cases for non-saturating feedback. Only irreversible T1s are counted in Fig. 6E. Because saturating feedback only very rarely produces reversible T1s, all quantifications other than Fig. 6 show the total T1 count without any filtering.

Reversible T1s are defined as follows. Consider an edge ij between cells i and j , the central edge in a quartet of cells $ikjl$ (in clockwise order). The collapse of edge ij creates an edge kl . This T1 is considered reversible if kl collapses in turn to give rise to a connection ij again, i.e. kl re-collapses before any of the outer edges il , lj , ik , or ki , of the quartet have collapsed. In this case, the

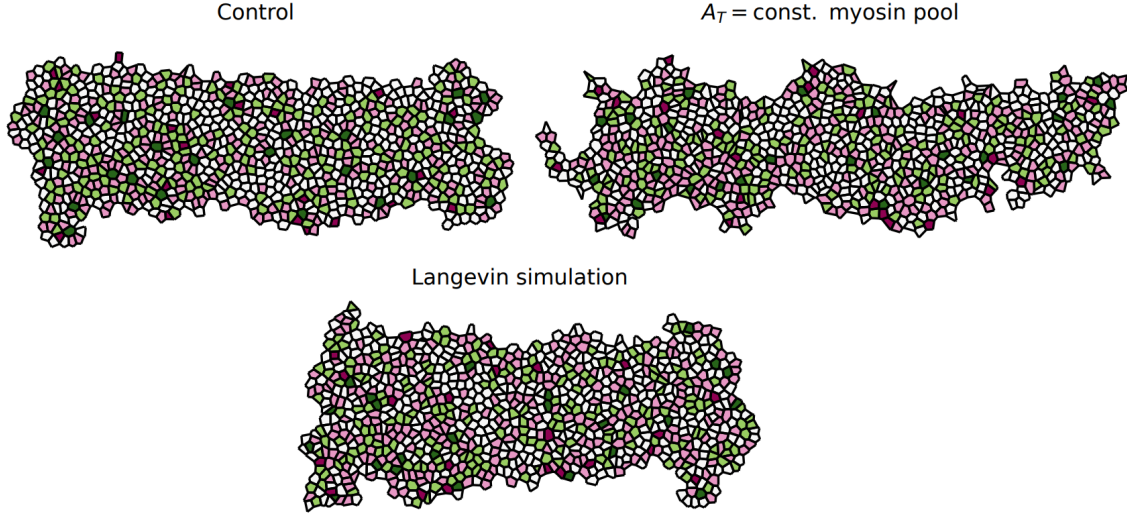


FIG. S6. Final tissue shapes (40 min simulation time) for the alternative tissue dynamics models discussed in the SI. Simulations were initialized with an “ordered” tension triangulation and initial anisotropy $s = 0.2$. Cells are colored by coordination number (same color code as in Fig. 2A).

local quartet topology returns to its original state. We also filter out nested sequences of multiple reversible T1s, but such events are extremely rare.

2.4. Effect of hexatic order orientation

When carrying out simulations in which the tissue is initially ordered, the initial tension triangulation corresponds to a (rectangular) patch of a triangular lattice. We can choose two possible orientations of the lattice plane with respect to the tension anisotropy – one creating initially mainly tension cables, one mainly bridges. This corresponds to the orientation of the hexatic order Ψ_6 w.r.t. the axis of tension anisotropy, and we refer to these orientations as “bridge” and “cable” initial conditions. We find that the qualitative behavior of the model is independent of this choice, and positive tension feedback is capable of creating coherently ordered T1s even if future collapsing edges are not singled out in the initial condition. To underline this point, Fig. 2 uses “cable” initial conditions. For the determination of LTC distribution dynamics in main text Fig. 5, as well as the heat map Fig. 3A, we pool simulations from cable and bridge initial conditions. When showing snapshots from a simulation, the “parallel” initial condition most easily creates the recognizable pattern of alternating high and low tensions reported in the companion paper.

A quantitative comparison is shown in Fig. S7. We see that an initial bridge bias leads to higher bridge fraction later on, and somewhat larger amounts of convergent extension.

2.5. Interface extension is independent of tissue extension

As argued in the main text, interface extension after active T1s is not driven by external forces (e.g. due to tissue elongation) but locally by cortical tensions. Active T1s are fundamentally asymmetric in time: the collapsing interface has high myosin levels, and the newly formed interface has very low

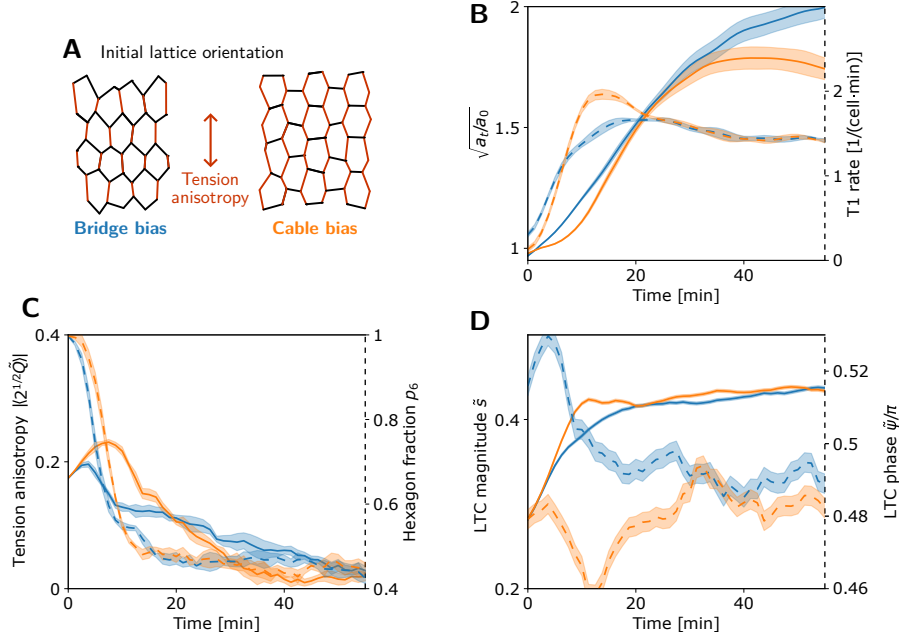


FIG. S7. Dependence of tissue dynamics on initial tension bridge vs tension cable bias. **A** The orientation of a hexagonal array of cells relative to the axis of tension anisotropy determines whether the anisotropic tensions manifest primarily as tension bridges (left) or tension cables (right). **B–D** Quantification of simulations initialized with hexagonal cell arrays with bridge bias (blue curves) and cable bias (orange curves). **B** Change of tissue aspect ratio (solid lines, left axis) and T1 rate (dashed lines, right axis) show that convergent extension is faster and more efficient (fewer T1s are required for the same shape change) for an initial bridge bias. Shaded bands indicate standard deviation. **C** Magnitude of mean tension anisotropy (solid lines, left axis) and hexagon fraction (dashed lines, right axis). Shaded bands indicate standard deviation. **D** Mean local tension anisotropy magnitude (solid lines, left axis) and median LTC phase (dashed lines, right axis) showing the initial bridge/cable bias and eventual convergence of the LTC phase. Shaded bands indicate standard error. Initial tension anisotropy magnitude $s = 0.2$.

levels. Since these low levels are insufficient to balance the tensions of the surrounding interfaces, the new interface extends.

Our simulations support the notion that interface extension does not depend on tissue extension, even though our simulations contain no additional active mechanisms to elongate new interfaces. In the main text, we showed simulations of a tissue geometry without a soft, passive region to compensate the convergence of the active tissue (analogous to a *Toll*/*RM9* mutant). Because of incompressibility, the active tissue also does not extend. Nevertheless, new interfaces elongate at rates very similar to control simulations (Fig. 8). We now support this conclusion with an additional simulation. Mimicking experiments where tissue extension is blocked by a cauterization fence [8], we block tissue extension by adding slip walls along the AP boundaries of the tissue patch (Fig. S9A). For numerical reasons, we add a small passive zone in front of these additional boundaries, and enforce the slip-wall condition with a softer penalty than for the dorsal slip walls. This is done to avoid direct conflicts between the boundary conditions and the angle constraints from the triangulation. In these simulations, the active tissue does not extend, and cells deform to compensate T1s (Fig. S9A). In a control simulations (Fig. 8), by 15 minutes, the tissue has elongated

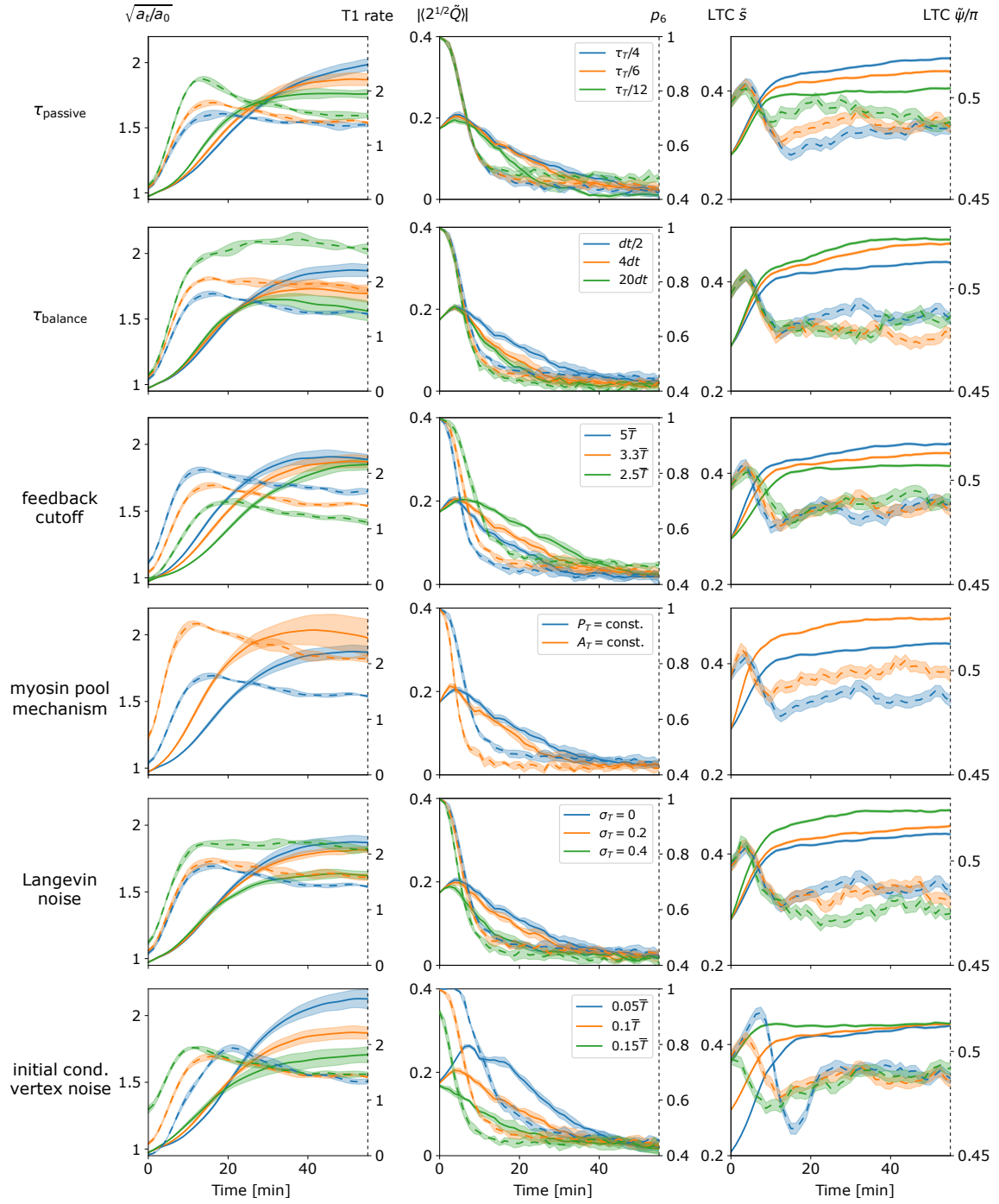


FIG. S8. Dependence of model behavior on parameters. Each row of plots shows the dependence on one parameter or modelling choice. The three columns follow the same convention as Fig. S7B–D. The passive relaxation time τ_p , the balancing time τ_{balance} , the feedback cutoff, and the initial condition vertex noise are explained in more detail in SI Sec. 4.

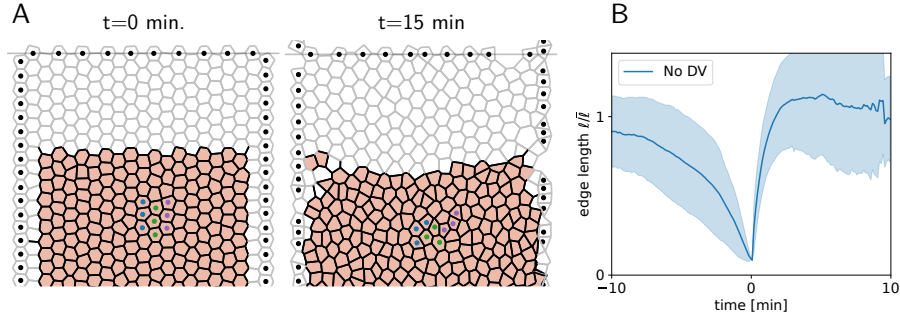


FIG. S9. Interfaces extend even if tissue extension is blocked. **A** Snapshots from a simulation where tissue extension is blocked by slip walls along the AP boundaries of the tissue patch. This mimics experiments where the germ band is blocked from extending via cauterization of the ventral tissue close to the posterior pole, or mutations in the posterior midgut [8]. **B** Even though net tissue deformation is blocked, the interface length during active T1s is qualitatively similar to simulations of freely deforming tissues (cf. “WT” in Fig. 8B).

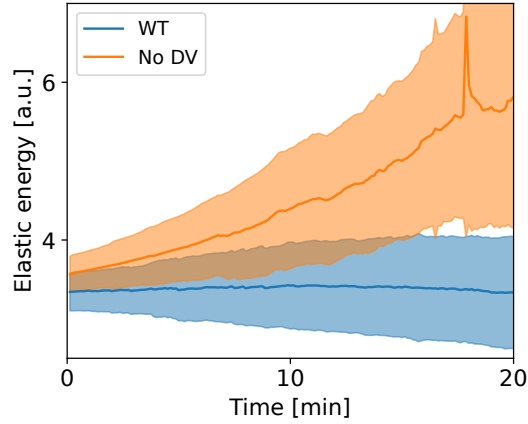


FIG. S10. Elastic energy in germ-band simulations tissue-scale simulations (Fig. 7). Note that in “WT” simulations, the elastic energy does not increase over time. If no passive tissue exists to compensate the extension of the germ band, cell elongate and elastic energy builds up.

by 30% by the time shown. However, new interfaces still successfully extend (Fig. S9B), like in the *Toll*[*RM9*] simulations shown in Fig. 8. The overall speed of intercalations is slightly reduced because of the additional slip walls. Note that occasionally, we observe rupture of the simulated tissue from the simulation boundary because of the internal forces generated by T1 transitions. Similar rupture events are seen in experiment.

2.6. Scale separation between cortical tensions and cell shape elastic energy

As discussed in the main text, we have formulated a model of epithelial tissue mechanics in the limit where the cortical tensions are the dominant source of stress. This separation of scales is

encoded by the small parameter ε in Eq. (1). To lowest order in ε , force balance of the cortical tensions impose geometric constraints on angles under which the subdominant “cell-shape energy” is relaxed. In other words, the tension-driven and isogonal degrees of freedom are clearly separated. To higher order in ε , the cell-shape energy changes the angles, thus mixing the tension-driven and isogonal modes. How small does ε have to be such that we can ignore this higher order effect?

To answer this question, we need to compare the tension force balance to the force on vertex angles exerted by the cell-shape energy $\varepsilon \sum_i E_C(\{\mathbf{r}_{ijk}\})$ (defined in Eq. (3)). This force is given by the elastic energy gradient $\nabla E_C = \partial_{\mathbf{r}_{ijk}} \sum_i E_C(\{\mathbf{r}_{ijk}\})$ at the vertex positions $\mathbf{r}_{ijk}^* = \text{argmin}_{\mathbf{r}_{ij} \perp \mathbf{t}_{ij}} \sum_i E_C(\{\mathbf{r}_{ijk}\})$ which minimize the elastic energy under the angle constraints imposed by the tension triangulation (i.e. the tension triangulation edges \mathbf{t}_{ij} and the cell edges \mathbf{r}_{ij} are orthogonal). At this minimum, a displacement $\delta \mathbf{r}_{ijk} = -h \nabla E_C(\mathbf{r}^*)$ for a small $h > 0$ has no isogonal component and acts purely on angles. We impose this displacement and calculate the tension- and cell-elasticity energy cost via the non-dimensional ratio

$$f = \frac{\sum_i E_C(\{\mathbf{r}_{ijk}^* + \delta \mathbf{r}_{ijk}\}) - E_C(\{\mathbf{r}_{ijk}^*\})}{\sum_{ij} T_{ij} [\ell_{ij}(\{\mathbf{r}_{ijk}^* + \delta \mathbf{r}_{ijk}\}) - \ell_{ij}(\{\mathbf{r}_{ijk}^*\})]}. \quad (\text{S6})$$

This expression on data from the simulation shown in Fig. 2A, we find $f \approx -3\mu\bar{\ell}/\bar{T}$, where $\bar{\ell}$ and \bar{T} are the average interface length and tension, respectively. They set the basic units of length and force. In our simulations, we set $\bar{T} = 1$ and $\bar{\ell} = 1/\sqrt{3}$ (this ensures that the cell sizes are compatible with the Voronoi dual of the tension triangulation [17]). f is negative because the cell-shape energy can relax further by changing the angles, compared to when it is constraint to the isogonal (fixed-angle) subspace. Notably, only the shear modulus μ of the cells contributes, indicating that the effect of bulk elasticity on the angles is negligible. The numerical factor of 3 is a consequence of the particular way we have defined the elastic energy and not fundamental. Given our choice of units, the parameter setting $\mu = 1$, we must have $\varepsilon \lesssim 0.2$ for the separation of tension-driven and isogonal modes to be valid.

To test this, we numerically ran simulations with different values of ε , 0.001 (our default value), 0.01, 0.1, and 1. As shown in Fig. S11, we find almost identical behavior of the simulations for $\varepsilon = 0.001$ and $\varepsilon = 0.1$. By contrast, for $\varepsilon = 1$ tissue shape change is impaired since the tensions are insufficient to overcome the tendency of the cell-shape energy to drive cells to regular hexagon shapes. In other words, the cell-shape energy imposes energy barriers that prevent T1 transitions. In particular, we find that at $\varepsilon = 1$, more than half of T1 transitions reverse, and are hence ineffective, while this is the case for less than 2% of T1s at $\varepsilon = 0.001$. Without explicit saturation of the positive tension feedback, this suppression of T1s leads to buildup of extreme tension anisotropy, eventually leading to numerical problems.

3. ISOGONAL SHEAR AND TISSUE SHEAR MODULUS

As discussed in the main text, and shown in Fig. 8 our simulations show that a non-zero cell-level shear modulus is required for extension via active T1s. Here, we analyze the relation of cell-level and tissue-level shear modulus. Crucially, because of the dominance of cortical tensions, a tissue patch in our model will respond to externally applied forces via an isogonal deformation. We first show that an isogonal deformation can create tissue-scale shear (on the level of cell centroid displacement – the transformation of cell vertices is necessarily non-affine to preserve angles). Then we show that these shear modes correspond to the response of the tissue to external force by computing the Hessian of our cell elastic energy in the subspace spanned by isogonal deformations, and measure the shear modulus.

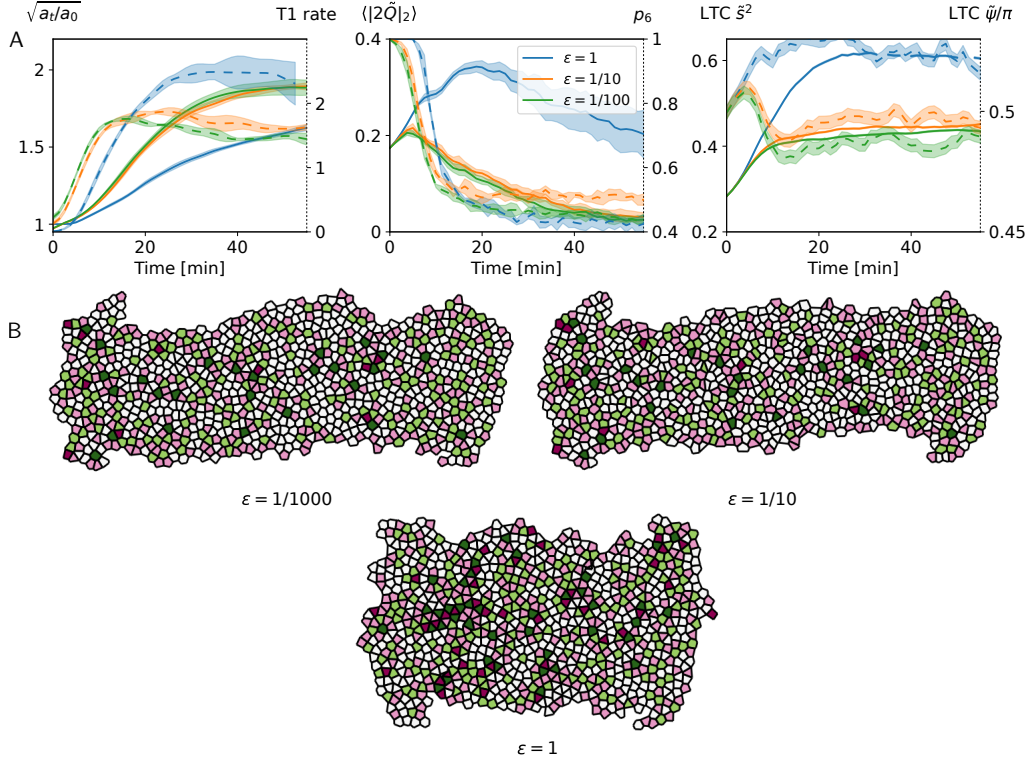


FIG. S11. Simulations for different values of the tension-isogonal scale-separation parameter ε . **A** Quantification of tissue deformation and order parameters. Note that the change of aspect ratio is nearly identical for $\varepsilon = 0.001, 0.1$ and 1 . **B** Snapshots at time $t = 30\text{min}$ for $\varepsilon = 0.001, \varepsilon = 0.1$, and $\varepsilon = 1$.

3.1. Quadratic isogonal mode profile creates shear deformation

To show that isogonal modes can cause shear deformations, not just dilation/contraction of cells, we make use of the isogonal mode parametrization introduced in Ref. [13]. It assigns an isogonal “potential” Θ_i to each cell, and calculates the cell displacements from the Θ_i and the edge tension vectors. In the following, we will show that a constant gradient in the isogonal potential generates a uniform translation in real space. By integration, this implies that a quadratic spatial profile of the isogonal potential creates a shear.

Let us identify the real space edge unit vectors by the two adjacent cells $\mathbf{e}_{ij} = -\mathbf{e}_{ji}$ and denote the corresponding tensions as T_{ij} . Then the tension vectors $\hat{\mathbf{T}}_{ij} = T_{ij}\hat{\mathbf{e}}_{ij}$ form a triangulation, where $\hat{\mathbf{a}}$ denotes the normal vector to \mathbf{a} , i.e. $\hat{\mathbf{a}} \cdot \mathbf{a} = 0$ and $||\hat{\mathbf{a}}|| = ||\mathbf{a}||$.

The isogonal displacement \mathbf{u}_{ijk} of the real space vertices \mathbf{r}_{ijk} (identified by the three adjacent cells) is given by

$$\mathbf{r}_{ijk} \rightarrow \mathbf{r}_{ijk} + \mathbf{u}_{ijk} = \mathbf{r}_{ijk} + \frac{1}{S_{ijk}} [\Theta_i \mathbf{T}_{jk} + (\text{cyc.})] \quad (\text{S7})$$

where $S_{ijk} = \hat{\mathbf{T}}_{ij} \cdot \mathbf{T}_{ik}$ is the area of the tension triangle (ijk) .

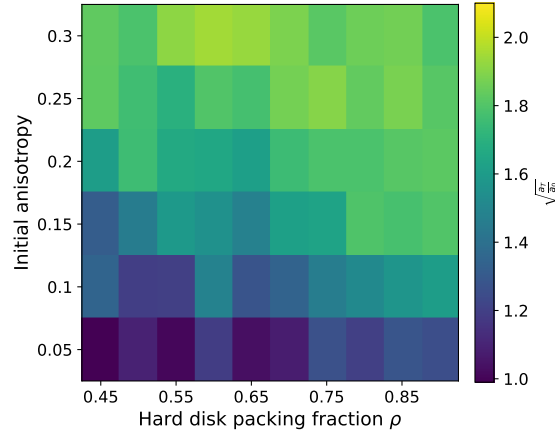


FIG. S12. Dependence of convergent extension on initial order and anisotropy for vanishing shear rigidity. Heatmap of elongation (square root of aspect ratio change) as in main text Fig. 3A, for $\mu = 0$ (low shear rigidity). In Fig. 3A, we used $\mu = 1$, the default value in this paper. For lower shear rigidity, less convergent extension takes place, as discussed in Fig. 8G. The overall structure of the phase diagram remains similar, with weaker dependence on initial order. Note that the simulation was performed with free boundary conditions, i.e. there is no external resistance to tissue deformation. An adjacent passive tissue with non-zero shear modulus would suppress convergent extension further (cf. Fig. 8F). For this supplementary figure, we only carried out 3 replicate simulations.

First, observe that the uniform isogonal mode $\Theta_i = \text{const.}$ has no effect on the vertex positions because

$$\mathbf{T}_{jk} + \mathbf{T}_{ki} + \mathbf{T}_{jk} = 0 \quad (\text{force balance}). \quad (\text{S8})$$

Now we aim to show that a constant gradient in Θ_i drives a uniform displacement of the \mathbf{r}_{ijk} . Specifically, by uniform gradient we mean $\Theta_i = \mathbf{t}_i \cdot \mathbf{a}$, i.e. a linear gradient in the tension space (\mathbf{t}_i is the position of the tension triangulation vertex corresponding to cell i , such that $\hat{\mathbf{T}}_{ij} = \mathbf{t}_j - \mathbf{t}_i$). To show that the displacement in real space is uniform, it is enough to show that two adjacent vertices are displaced identically. By induction, this implies that all displacements are identical. It is therefore sufficient to consider a quartet of cells ($i = 1-4$), corresponding to a “kite” in tension space (note that $\hat{\mathbf{a}} \cdot \mathbf{b}$ is identical to the wedge product $\mathbf{a} \wedge \mathbf{b}$.)

Because a constant can be arbitrarily added to all Θ_i , we can set $\Theta_1 = 0$ and thus have $\Theta_i = \hat{\mathbf{T}}_{ij} \cdot \mathbf{a}$ for $i = 2, 3, 4$. The displacements now read

$$\mathbf{u}_{123} = \frac{1}{S_{123}} (\hat{\mathbf{T}}_{12} \cdot \mathbf{a} \mathbf{T}_{31} + \hat{\mathbf{T}}_{13} \cdot \mathbf{a} \mathbf{T}_{12}) \quad (\text{S9})$$

$$\mathbf{u}_{134} = \frac{1}{S_{134}} (\hat{\mathbf{T}}_{13} \cdot \mathbf{a} \mathbf{T}_{41} + \hat{\mathbf{T}}_{14} \cdot \mathbf{a} \mathbf{T}_{13}) \quad (\text{S10})$$

To show that these displacements are identical, we project them onto two conveniently chosen,

linearly independent vectors, namely $\hat{\mathbf{T}}_{12}$ and $\hat{\mathbf{T}}_{13}$. For the latter we find

$$\hat{\mathbf{T}}_{13} \cdot \mathbf{u}_{123} = \frac{1}{S_{123}} \hat{\mathbf{T}}_{13} \cdot \mathbf{a} \hat{\mathbf{T}}_{13} \cdot \mathbf{T}_{12} = -\hat{\mathbf{T}}_{13} \cdot \mathbf{a}, \quad (\text{S11})$$

$$\hat{\mathbf{T}}_{13} \cdot \mathbf{u}_{134} = \frac{1}{S_{134}} - \hat{\mathbf{T}}_{13} \cdot \mathbf{a} \hat{\mathbf{T}}_{13} \cdot \mathbf{T}_{14} = -\hat{\mathbf{T}}_{13} \cdot \mathbf{a}, \quad (\text{S12})$$

where we used that $\hat{\mathbf{T}}_{ij} \cdot \mathbf{T}_{ij} = 0$ and applied the definition of S_{ijk} .

Projecting (S9) and (S10) onto $\hat{\mathbf{T}}_{12}$ gives

$$\hat{\mathbf{T}}_{12} \cdot \mathbf{u}_{123} = \frac{1}{S_{123}} \hat{\mathbf{T}}_{12} \cdot \mathbf{a} \hat{\mathbf{T}}_{12} \cdot \mathbf{T}_{31} = -\hat{\mathbf{T}}_{12} \cdot \mathbf{a} \quad (\text{S13})$$

$$\hat{\mathbf{T}}_{12} \cdot \mathbf{u}_{134} = \frac{1}{S_{134}} (\hat{\mathbf{T}}_{13} \cdot \mathbf{a} \hat{\mathbf{T}}_{12} \cdot \mathbf{T}_{41} + \hat{\mathbf{T}}_{14} \cdot \mathbf{a} \hat{\mathbf{T}}_{12} \cdot \mathbf{T}_{13}) \quad (\text{S14})$$

To show equality of these two right-hand sides, we use that given $\hat{\mathbf{T}}_{13} \cdot \mathbf{a}$ and $\hat{\mathbf{T}}_{14} \cdot \mathbf{a}$ we can find \mathbf{a} and substitute the result into $\hat{\mathbf{T}}_{12} \cdot \mathbf{a}$. We start by “expanding the identity”

$$\begin{pmatrix} -\hat{\mathbf{T}}_{13} \\ -\hat{\mathbf{T}}_{14} \end{pmatrix} \mathbf{a} = \begin{pmatrix} \hat{\mathbf{T}}_{13} \cdot \mathbf{a} \\ \hat{\mathbf{T}}_{14} \cdot \mathbf{a} \end{pmatrix} \Rightarrow \mathbf{a} = \begin{pmatrix} -\hat{\mathbf{T}}_{13} \\ -\hat{\mathbf{T}}_{14} \end{pmatrix}^{-1} \begin{pmatrix} \hat{\mathbf{T}}_{13} \cdot \mathbf{a} \\ \hat{\mathbf{T}}_{14} \cdot \mathbf{a} \end{pmatrix} \quad (\text{S15})$$

Explicitly writing out the inverse matrix then gives

$$\mathbf{a} = \frac{1}{\hat{\mathbf{T}}_{13} \cdot \mathbf{T}_{14}} \begin{pmatrix} | & | \\ \mathbf{T}_{14} & -\mathbf{T}_{13} \\ | & | \end{pmatrix} \begin{pmatrix} \hat{\mathbf{T}}_{13} \cdot \mathbf{a} \\ \hat{\mathbf{T}}_{14} \cdot \mathbf{a} \end{pmatrix} \quad (\text{S16})$$

With this, we find the relation

$$\hat{\mathbf{T}}_{12} \cdot \mathbf{a} = -\frac{1}{S_{134}} (\hat{\mathbf{T}}_{12} \cdot \mathbf{T}_{41} \hat{\mathbf{T}}_{13} \cdot \mathbf{a} + \hat{\mathbf{T}}_{12} \cdot \mathbf{T}_{13} \hat{\mathbf{T}}_{14} \cdot \mathbf{a}) \quad (\text{S17})$$

where we used $\mathbf{T}_{ij} = -\mathbf{T}_{jk}$ to flip the indices on \mathbf{T}_{14} . Comparing to (S13) and (S14) now shows the identity of their RHSs.

Taken together, we have shown that

$$\hat{\mathbf{T}}_{12} \cdot \mathbf{u}_{123} = \hat{\mathbf{T}}_{12} \cdot \mathbf{u}_{134} \quad \text{and} \quad \hat{\mathbf{T}}_{13} \cdot \mathbf{u}_{123} = \hat{\mathbf{T}}_{13} \cdot \mathbf{u}_{134}, \quad (\text{S18})$$

Because $\hat{\mathbf{T}}_{12}$ and $\hat{\mathbf{T}}_{13}$ are linearly independent, it follows that $\mathbf{u}_{123} = \mathbf{u}_{134}$. QED.

We just showed that a constant gradient in Θ_i corresponds to a uniform displacement of the real space vertices \mathbf{r}_{ijk} . We can therefore think of $\Theta(\mathbf{t})$ as a “potential” for the isogonal displacement field: $\mathbf{u} \approx \nabla_{\mathbf{t}} \Theta$, where the approximation is valid for slowly varying gradients and exact for constant gradients. The gradient $\nabla_{\mathbf{t}}$ is taken in *tension space* because the function $\Theta(\mathbf{t}_i) = \Theta_i$ is defined on the vertices of the tension triangulation \mathbf{t}_i .

A pure shear aligned with the coordinate axes is given by a displacement field $\mathbf{u}(\mathbf{r}) = \varepsilon \text{diag}(1, -1) \cdot \mathbf{r}$ and is therefore generated (approximately) by a quadratic isogonal potential $\Theta_i = \varepsilon \mathbf{t}_i^T \cdot \text{diag}(-1, 1) \cdot \mathbf{t}_i = \varepsilon [(t_i^1)^2 - (t_i^2)^2]$.

3.2. Isogonal Hessian and tissue-scale isogonal shear modulus

Above we have shown that isogonal modes can create a shear (on the level of cell centroids). We now show (a) that shear transformations are the lowest-energy isogonal modes and hence will dominate the response of the tissue to external forces, and (b) that shear transformations incur a finite energy cost, implying a finite shear modulus – the tissue is not a fluid. To do this, we assume that the tissue is initially at the elastic energy minimum under the constraints of a given tension triangulation. In this case, we can approximate the energy E by a quadratic function of displacement by computing the Hessian. In our model we impose that vertex angles are given by the intrinsic tension triangulation, hence we cannot study how tensions respond to external forces. Further, due to the dominance of cortical tensions, the lowest-energy deformations of the tissue are isogonal. Hence, here, we only allow isogonal displacements, and we will project the Hessian onto the space of isogonal modes. The lowest eigenvectors of the isogonal Hessian will then correspond to the modes excited by external forcing.

The isogonal unit vectors convert the isogonal potentials into real-space displacement of vertices: the isogonal potential Θ_j at cell j contributes a term $\Theta_j \mathbf{I}_j^{jkl}$ to the displacement of vertex \mathbf{r}_{jkl} adjacent to j . The \mathbf{I}_j^{jkl} are defined by the action of isogonal modes Eq. (S7) and serve to project the Hessian onto the space of isogonal modes. Explicitly, $\mathbf{I}_j^{jkl} = \frac{1}{S_{jkl}} \mathbf{T}_{kl}$, where $S_{jkl} = \hat{\mathbf{T}}_{jk} \cdot \mathbf{T}_{kl}$ is the area of the tension triangle (jkl) . The isogonal Hessian reads:

$$\mathcal{H}_{il} = \sum_{(jk),(mn)} \mathbf{I}_i^{ijk} \frac{\partial^2 E(\{\mathbf{r}_{abc}\})}{\partial \mathbf{r}_{ijk} \partial \mathbf{r}_{lmn}} \mathbf{I}_l^{lmn} \quad (\text{S19})$$

Note that only the E_C term from Eq. 1 contributes to the isogonal Hessian, by virtue of the isogonal projection.

With the same code used for the tissue-scale simulations, we can numerically construct and diagonalize \mathcal{H}_{il} . There are 3 trivial 0-modes which correspond to two real-space translations and a globally constant isogonal parameter, which creates no cell displacement. This is in accordance with the results from above and the fact that the E only depends on differences in vertex positions. We find that the two lowest non-trivial modes are shear modes (quadratically varying isogonal potential Θ_i). They are shown for an example lattice in Fig. S13A. Finding shear modes is not unexpected since they minimize the variation in vertex displacement across the tissue, and the energy function E is convex (quadratic).

External forces, e.g. external shear, will mainly excite the lowest eigenmodes of the Hessian. The energy cost is determined by the Hessian eigenvalues, which therefore define the shear modulus. In the example shown in Fig. S13A the eigenvalues of the shear modes are 2 orders of magnitude smaller than the next eigenvalues. The highest eigenvalues correspond to isogonal deformations localized to a single quartet.

To compute a measure of resistance to shear deformations, the tissue-scale “isogonal shear modulus”, we consider a vertex displacement $h \cdot \delta \mathbf{r}_{ijk}$, $h > 0$ along one of the two lowest-energy shear eigenmodes of the isogonal Hessian. We then compute

$$\mu_{\text{tissue}} = \frac{\partial^2}{\partial s(h)^2} \sum_l E_{C,l}(\{\mathbf{r}_{ijk} + h \delta \mathbf{r}_{ijk}\}) \quad (\text{S20})$$

where $s(h)$ is the shear induced by the vertex displacement. In practice, we compute $s(h)$ by least-squares fit of a shear transformation to the displacement map $\mathbf{r}_{ijk} \mapsto \mathbf{r}_{ijk} + h \cdot \delta \mathbf{r}_{ijk}$. We then fit a parabola to the curve $(s(h), E_C(h))$ to extract the 2nd derivative. We can then investigate how the isogonal shear modulus depends on the cell-level shear modulus in the elastic energy. As expected,

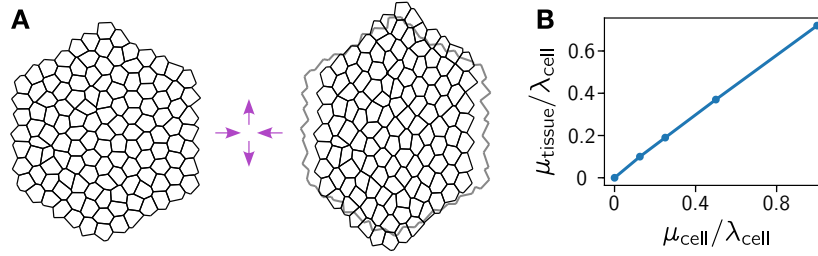


FIG. S13. **Cell-level shear modulus determines tissue level shear modulus.** **A** Large-scale tissue shear are the lowest energy isogonal modes. Reference configuration (minimum energy for a given tension triangulation, left) and deformed configuration (right, outline shows reference configuration), deformed according to the isogonal Hessian eigenvector of one of the two lowest eigenvalues in an example tissue patch. **B** Tissue level “isogonal shear modulus” (see Eq. (S20) for a definition) is proportional to cell level shear modulus. Tissue level isogonal shear modulus vs cell-level shear modulus for the tissue patch shown in A.

we find that the two are proportional (Fig. S13B), showing that the tissue as a whole is solid, in the sense of a non-vanishing shear modulus. We note that a proper investigation of the tissue-scale shear modulus will require addressing the question of how tensions change when external forces are applied, and is hence beyond the scope of the paper.

4. MODEL DETAILS AND SIMULATION METHODS

In the following, we explain the simulations presented in the paper and provide the modeling and implementation details. These comprise the mean-field calculation of the dynamics of the distribution of vertex angles, the symmetric lattice of a single intercalating quartet (shown in the companion paper [17]), and the tissue-scale simulation of a disordered epithelial tissue comprising both active and passive regions. All code used to create and analyse the simulations is available on GitHub https://github.com/nikolas-claussen/CE_simulation_public.

4.1. Positive feedback tension dynamics and single-vertex simulation

We begin by describing the intrinsic tension dynamics of a single tension triangle. This is the basis for the single-triangle simulation in Fig. 5, where we show the dynamics of the distribution of vertex angles predicted by a positive tension feedback model. Under this model, the edge tensions \tilde{T}_α , $\alpha = 1-3$, at a vertex evolve according to:

$$\tau_T \dot{\tilde{T}}_\alpha = T_\alpha^n - \frac{1}{3} \sum_\beta \tilde{T}_\beta^n$$

where $n > 1$ and τ_T is a time scale converting simulation time into minutes. Note that we fix the overall tension scale by the constraint that the triangle perimeter $P = \sum_\alpha \tilde{T}_\alpha$ is fixed (corresponding to a finite total myosin pool). This simplified the analysis of saturating positive feedback below, and is consistent with the single-quartet simulations in the companion paper. Fixing the triangle area A instead does not significantly affect the results for the single triangle simulations. The feedback exponent was taken as $n = 4$ as in Ref. [17]. Different values give very similar results, so

no systematic optimization was performed. We note that since the tension constraint $P = \text{const.}$ or $A = \text{const.}$ only affects the overall triangle size, and the trajectories in LTC space (but not their speed) are independent of it.

We integrated the tension dynamics using a 4th order Runge-Kutta method as implemented in the SciPy software package [72], using as initial conditions the vertex angles in the experimental data at time $t = 5$ min (the vertex angles from the data were temporally smoothed with a window of 2 min to reduce noise). From our simulation, we computed the LTC parameter to compare the marginals with the experimental data.

Dynamics in the LTC space. To find the trajectories in the LTC space, we integrated Eq. (5). A change of variables from side length to the LTC space yields the flow shown in Fig. 5A. To model the effect of intercalations, which remove highly obtuse tension triangles from the distribution, we stopped integration once the maximum relative tension increased over $T_{\text{rel}} = 1.56$, the median of the relative tension at the moment of a T1 observed in the tissue-scale simulations with isogonal stretching (as well as in the experimental data). These “collapse” triangles were removed from the simulation ensemble.

Fit of the tension timescale to experimental data. To determine the tension timescale τ_T , we compute the dynamics of the relative tension (the ratio of the edge tension to that of the adjacent edges) for all edges that undergo a T1 transition and align them temporally based on the time the T1 process occurs. This leads an average $T_{\text{rel}}(t)$ that can be compared to the time traces from the experimental data reported in the companion paper [17] to fit τ_T . Because the tension dynamics in the tissue-scale simulations is affected by tension balancing (see below), while the single-triangle and single-quartet simulations are not, we fit τ_T separately for the two classes of simulations. Note that we fit the tension timescale to a microscopic process, the T1 transition, and the resulting time course for macroscopic observables (tissue extension, LTC distribution) matches the experimental data without additional adjustment.

4.2. Tension dynamics post intercalation: Myosin handover and passive tension

In the single-triangle simulations, we only consider dynamics up to the moment of intercalation. At this point, the tension triangulation is modified topologically: the edge corresponding to the collapsed interfaces is replaced by one corresponding to the new interface (triangulation “flip”). To complete our model, we must specify the initial conditions of this new edge.

As explained in the companion paper, we propose a myosin handover mechanism to explain the extension of the new interface post intercalation. A interface with cortical tension T is comprised of the adherens-junctional actomyosin cortex of the two adjacent cells, which are coupled mechanically via adherens junctions. Under force balance, the total tension T has to be constant along the cortex, but the individual tensions on either side can be non-uniform, as the resulting traction forces are exchanged via adherens junctions. In the following, we assume as a first order approximation that the level of active tension (i.e. myosin concentration) varies linearly along an interface (similar calculations have been performed in Ref. [73] to calculate interfacial shear stress). This allows us to geometrically obtain the myosin concentration at the individual cortices that will form the two juxtaposed sides of the new interface (see companion paper).

Consider a vertex, where interfaces $i = 0, 1, 2$ (with tensions T_0, T_1, T_2) meet, and let 0 be the interface about to collapse. For an illustration, see Ref. [17], Fig. 4). The three cells that meet at the vertex will be referred to by (01), (12), (21) (where e.g. (01) is the cell abutting interfaces 0 and 1). Let m_{01}, m_{12}, m_{21} be the motor molecule concentrations (in units of tension) at the vertex in the junctional cortices of the three cells. Then, the tensions are related to the motor molecule

concentrations as:

$$T_0 = m_{21} + m_{01}, \quad T_1 = m_{01} + m_{12}, \quad T_2 = m_{12} + m_{21}.$$

This uses the assumption of myosin continuity at vertices, and the fact that the tension on an interface is the sum of the tensions of the two cortices that make it up. The motor molecule concentration on the cortex belonging to the new interfaces, post collapse, will be equal to m_{12} . Solving for this in terms of the tensions:

$$m_{12} = \frac{T_1 + T_2 - T_0}{2}$$

The new interface consists of two cortices, coming from the two vertices of the collapsed interface. Let the tensions at the two triangles be T_0, T_1, T_2 and T_0, T'_1, T'_2 . Let T_a be the active tension on the new interface immediately after the T1. It is the equal to

$$T_a = \frac{(T_1 + T_2 - T_0) + (T'_1 + T'_2 - T_0)}{2} \quad (\text{S21})$$

Note however that the total tension T_n on the new interface is not necessary equal to T_a . The total tension is defined geometrically from the angles at the new interface (or, equivalently, the tension triangulation vertices). Indeed, generally, $T_n > T_a$, i.e. the active tension on the new interface is not enough to balance the tension due to the adjacent edges. As explained in the companion paper, we introduce a passive tension T_p on the new edge which balances this deficit

$$T_p = T_n - T_a = T_n - (m_{12} + m'_{12})$$

For example, if a perfectly symmetric quartet collapses when the vertex angle facing the collapsing edge is 90° , $T_1 = T_2 = T'_1 = T'_2 = 1$ and $T_0 = T_n = \sqrt{2}$. Therefore, $T_{a,n} = 2 - \sqrt{2} \approx 0.6$ and $T_{p,n} = \sqrt{2} - (2 - \sqrt{2}) \approx 0.8$. Note that by the triangle inequality, for any convex quadrilateral with perimeter P and diagonals D_1, D_2 , one has $P/2 \leq D_1 + D_2 \leq P$. Applying this to the quadrilateral formed by the two tension triangles at the collapsing interface, we get $T_{a,n} \geq 0$ and $T_{p,n} \geq 0$: the handover formula always results in positive active and passive tensions. Further, the “handover” mechanism robustly generates irreversible T1s: if a interface were to collapse back after a T1, the newly formed interface would inherit high myosin levels and therefore be likely to collapse again.

The passive tension subsequently relaxes visco-elastically with rate τ_p^{-1} : $\dot{T}_p = -\tau_p^{-1}T_p$. Combining this with the feedback equation, the evolution of the total tension is

$$\dot{T} = \tau_T^{-1} \left(T^n - \frac{1}{3} \sum_{\beta} \tilde{T}_{\beta}^n \right) - \tau_p^{-1} T_p \quad (\text{S22})$$

where we assumed that the positive feedback only operates on the active tension. The relaxation time scale was chosen at $\tau_p = \tau_T/4$, which fits the observed decay of tension post T1. If the tension relaxation rate τ_p^{-1} is too low, then positive tension feedback leads to a reversal of active T1s, and the T1 gets stuck at the 4-fold vertex configuration.

4.3. Cell shape elasticity

As explained in the main text, in our model, tension dynamics translate into tissue dynamics via force balance which we implement by minimizing the energy function Eq. (1). Here, we explain our

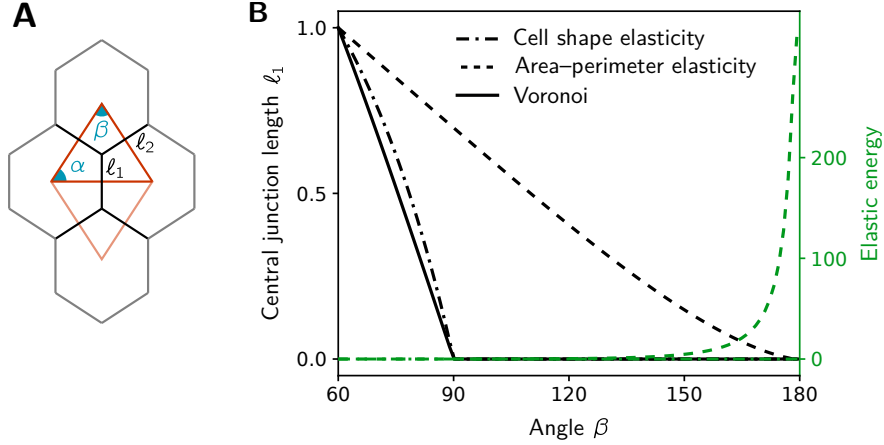


FIG. S14. Absence of energy barrier to intercalations **A** Length of the central interface in a quartet for a prescribed isosceles tension triangle parametrized by the angle β (the isosceles property implies $\alpha = (\pi - \beta)/2$). **B** The solid line shows the interface length in the Voronoi tessellation ℓ_{ref} (cf. Eq. (10)). The interface length obtained by minimizing elastic energy Eq. (3) with isotropic target shape (dot-dashed line) closely follows the Voronoi length and vanishes at the same critical angle. By contrast, minimizing the “area-perimeter” energy of the vertex-model $E_{\text{cell}} \sim (A - A_0)^2 + (P - P_0)^2$ in the solid phase, $P_0/\sqrt{A_0} < 3.81$, gives a interface length (dashed black line) that vanishes only for $\beta \rightarrow \pi$ and the energy diverges in this limit (dashed green line).

choice of the term representing cell-shape elasticity, E_C . We use an elastic energy based on the cell shape tensor

$$S_C = \sum_i \frac{\mathbf{e}_i \otimes \mathbf{e}_i}{|\mathbf{e}_i|}$$

where i runs over the edges of the cell \mathcal{C} , and \mathbf{e}_i is the vector pointing from one vertex of the interface to the other. Note that in this shape tensor, each edge contributes linearly in length to the cell shape. This means that artificially subdividing an edge has no effect on the cell shape tensor. This makes sense if we assume that the elasticity we aim to model using S resides in the cell interior (incompressibility, microtubules, intermediate filaments, nucleus). The shape tensor can also be defined using vectors from the cell centroid to its vertices (in the lattice, the two definitions are equivalent). An alternative definition of the elastic energy using $\tilde{S}_C = \sum_i \mathbf{e}_i \otimes \mathbf{e}_i$ instead gives broadly similar results (although interface collapse happens more abruptly, because of the higher order non-linearity).

We assign a reference shape S_0 and define the cell elastic energy via

$$E_C = \lambda[\text{Tr}(S_C - S_0)]^2 + \mu\text{Tr}[(S_C - S_0)^2] \quad (\text{S23})$$

with bulk modulus λ and shear modulus μ . The reference shape S_0 controls the isogonal mode. An isotropic $S_0 \propto \text{Id}$ favours equilateral hexagons. We used a shear/bulk ration of $\mu/\lambda = 1$ for all “active” cells in the simulations. Because of the separation of scales between cortical tensions and elastic energy baked into the model, the absolute values of λ, μ are irrelevant.

Strikingly, when the cell array is a regular lattice (see Fig. 1G and single-quartet simulations shown in the companion paper [17]), the “shape strain” $S_C - S_0$ can always be relaxed to 0 by choice

of the edge lengths, and the energy $E_C = 0$ throughout. This can already be seen from a degree-of-freedom count (three ℓ_i for the three independent components of $S_C - S_0$). The elastic energy therefore acts only on the isogonal modes (i.e. $\partial_{\phi_i} E_C|_{\ell_i=\text{minimizers}} = 0$) and there is no energy barrier for intercalations. Consequently, there is no need for noise to drive intercalations in our model. By contrast, for the widely-used area-perimeter elastic energy $E = (A - A_0)^2 + (P - P_0)^2$ (where A, P are the cell area and perimeter, and A_0, P_0 their target values) [29], there exists an energy barrier, and the inner interface ℓ_0 only collapses when $\beta \rightarrow \pi$ (see Fig. S14B). Note that the area-perimeter energy is a special case because of the geometric incompatibility of area and perimeter constraints when $P_0/\sqrt{A_0} < 3.72$. For $P_0/\sqrt{A_0} > 3.72$ cell shape is underdetermined (floppy) and the shear modulus vanishes. Recall that we have shown that a finite shear modulus is required to translate tension dynamics into tissue-level convergent extension (see Fig. 8G). The area-perimeter energy in the fluid regime is therefore not suitable to model convergent extension driven by internal tension dynamics.

Combining area elasticity with shear elasticity based on the shape tensor, $E = (A - A_0)^2 + \mu \text{Tr}[(S_C - S_0)^2]$, (or perimeter elasticity with cell shape bulk elasticity) leads to similar results as Eq. (3). Note also that because of the degree-of-freedom count, the system is under-specified if the shear modulus is 0, foreshadowing the fact that without shear modulus, no convergence-extension takes place. Indeed, in the case of the symmetric lattice, the degrees of freedom are the three vertex angles, determined by the tensions, and the three interface lengths, independent of the angles. Fixing the cell area still leaves freedom to change the interface lengths. More generally, we have shown above and illustrated in Fig. 1 that isogonal modes allow for area-preserving shear transformations.

4.4. Tissue scale simulation

Using the components of the single-quartet simulation, we now describe a simulation of an arbitrary, disordered tissue patch. The key assumption are again adiabatic force balance and cortical tension dominance: the tissue geometry is found by solving for force balance, by first finding the angles from the cortical tensions and then the isogonal mode by minimizing cell elastic energy. The key quantity is the tension triangulation whose dynamics determines the tissue dynamics.

Conceptually, there is one main novel element: since the tension triangulation is now disordered and comprises many heterogeneous tension triangles, an additional mechanism is required to ensure the tension triangles fit together to a global triangulation. Further, the higher computational load requires different numerical methods.

Data structure. We model a piece of epithelial tissue by a polygonal tiling of the plane, polygons corresponding to cells. Two cells are neighbors if they share an edge (this implies that the cell adjacency graph is a triangulation).

Following the idea of the dual tension triangulation introduced in the main text, a polygonal tiling is represented by a triangular mesh, in which cells are represented by vertices, cell edges by triangulation edges, and cell vertices by triangulation faces. Vertices, edges, and faces have the following attributes which are used for time evolution:

- Vertices: dual coordinates, the x, y coordinates of the vertex in the tension triangulation which will be denoted \mathbf{t}_i , and the reference shape g_0 for the shape-tensor elastic energy.
- Edges: the active and passive tensions on an edge.
- Faces: primal coordinates, the x, y coordinates of the vertex in the cell tessellation corresponding to the face, denoted \mathbf{r}_{ijk} .

Given the dual coordinates of two adjacent vertices $\mathbf{t}_i, \mathbf{t}_j$, the tension on the edge connecting cells i, j is $T_{ij} = |\mathbf{t}_i - \mathbf{t}_j|$. The dual coordinates encode a configuration of balanced cortical tensions.

Note that the primal (cell) and dual (tension) coordinates live in different spaces, and the overall scale of the tension coordinates is irrelevant.

The mesh is implemented in object oriented python, using a half-edge mesh data structure [74]. A half-edge mesh consists of vertices, faces, and, for each edge, two oriented half-edges. A half-edges stores a reference to the `next` half-edge on the counter-clockwise oriented face it belongs to, and a reference to its `twin`, the half-edge with opposite orientation on the adjacent face. This structure defines an orientation for every triangular face and makes mesh traversal (e.g. get all vertices of a cell) and mesh modification (e.g. intercalations) very convenient.

Overview. Due to the assumption of adiabatic force balance, the tissue geometry is determined by the instantaneous tensions. The dynamics is therefore determined by the change in the tension triangulation (due to positive feedback). In detail, the time evolution in our simulation is done in three steps:

1. Local Euler step: For each triangular face, update the active tensions according to positive tension feedback, and the passive tensions and the rest shape according to viscous relaxation.
2. Triangulation flattening: Optimize the dual vertex positions so that the lengths of each half-edge is as close as possible to its internally stored tension. This ensures global tension balance.
3. Cell shape optimization: Optimize the primal vertex positions to minimize the shape-tensor based elastic energy, while constraining the angles by the dual triangulation.
4. Topological modifications: Check if any primal edge has collapsed and carry out intercalations if necessary, re-initializing the active and passive tensions on the new edge.

The next sections describe them in detail. Fig. S15 provides a summary of the simulation workflow. The most complicated and time-consuming of them is the cell shape optimization. Overall, a simulation of convergent extension of ~ 1000 cells takes approx. 15 minutes on a current-generation laptop.

Note that the workflow of our simulations differs somewhat from the more common used dissipative dynamics, in which cell geometry is updated dynamically according to the ODE $\gamma \partial_t \mathbf{r}_{ijk} = -\frac{\partial E}{\partial \mathbf{r}_{ijk}}$. The dual separation of scales (fast relaxation and dominance of cortical tensions), mean that a direct implementation of dissipative dynamics is numerically challenging. The elastic energy minimization can be seen as a relaxational Euler step with an adaptive step size.

Relaxation via fast dissipative dynamics is a viable approach that could indeed be used as an alternative numerical relaxation method. However, as the theory of fast variable elimination in the context of multiscale dynamics is well established [75], we do not expect a different scheme to affect our results to an important degree. The key “ingredient” of our model is not how exactly the elastic energy is relaxed, but how active tensions are regulated.

Triangulation dynamics. For each mesh half-edge, we store the total intrinsic and passive tensions $\tilde{T}_{aij}, T_{p,ij}$. We collect the total and passive tensions from all half-edges ij belonging to a triangular face $I_{ijk} = \{(ij), (jk), (ki)\}$ and carry out an explicit Euler step with step size $\sim 10^{-3}$ according to the following dynamics:

$$\tau_T \partial_t \tilde{T}_{ij} = \tilde{T}_{ij}^n - k_{\text{cutoff}} \tilde{T}_{ij}^{n+1} - \frac{1}{3} \sum_{\alpha \in I_{ijk}} (\tilde{T}_{\alpha}^n - k_{\text{cutoff}} \tilde{T}_{\alpha}^{n+1}) - \frac{\tau_T}{\tau_p} T_{p,ij} \quad (\text{S24})$$

$$\tau_p \partial_t T_{p,ij} = -T_{p,ij} \quad (\text{S25})$$

The cutoff parameter k_{cutoff} stops runaway positive feedback at values $T > 1/k_{\text{cutoff}}$. It is not strictly necessary since runaway feedback is cut short by intercalations, but helpful for long-time simulations, were rarely, run-away tension cable configurations can occur which can blow up numerically. We

Initial condition creation

1. Place tension vertices \mathbf{t}_i (e.g. by sampling from a hard-disk process).
2. Compute Delaunay triangulation of tension vertices.
3. Apply shear transformation to determine initial anisotropy:
 $\mathbf{t}_i \mapsto \text{diag}(\sqrt{1+s}, 1/\sqrt{1+s}) \mathbf{t}_i$.
4. Initialize intrinsic tensions $\tilde{T}_{ij} = |\mathbf{t}_i - \mathbf{t}_j|$ and $T_{p,ij} = 0$.
5. Initialize cell vertices \mathbf{r}_{ijk} as Voronoi dual of the Delaunay triangulation.

Time stepping

Choose time-step size dt . For $i = 1, \dots, N_{\text{steps}}$ do:

1. Update intrinsic tensions (positive feedback Euler step):
 $\tilde{T}_{ij} \mapsto \tilde{T}_{ij} + f(\tilde{T}_{ij}, \dots)dt$. f is the feedback RHS.
2. Update tension triangulation vertices (least-squares fit to intrinsic tensions):
 $\mathbf{t}_i \mapsto \text{argmin}_{\frac{1}{2N_{\text{edges}}}} \sum_{ij} (|\mathbf{t}_i - \mathbf{t}_j| - \tilde{T}_{ij})^2 + \frac{1}{2N_{\text{tri}}} \sum_{ijk} \text{Pen}(A_{ijk}, A_0)$
3. Update intrinsic tensions (flatness feedback Euler step):
 $\tilde{T}_{ij} \mapsto \tilde{T}_{ij} - \tau_{\text{balance}}^{-1} (|\mathbf{t}_i - \mathbf{t}_j| - \tilde{T}_{ij})dt$
4. Update cell vertices by angle-constrained energy minimization:
 $\mathbf{r}_{ijk} \mapsto \text{argmin}_{\frac{1}{2N_{\text{tri}}}} \sum_{ij} T_{ij} \bar{\ell} (1 - \hat{n}_{ij} \cdot \mathbf{r}_{ij}) + \frac{\epsilon}{2N_{\text{cells}}} \sum_i E_{c,i}(S_i)$
5. Update topology: flip all edges of length $\ell_{ij} < \ell_{\min}$, update passive tensions $T_{p,ij}$ and intrinsic tensions \tilde{T}_{ij} in flipped edges.
6. Log: save topology, tension vertices, cell vertices, and T1-transitions.

FIG. S15. Simulation work flow showing a brief summary of the simulation code.

chose $1/k_{\text{cutoff}} = 5\bar{T}$ where \bar{T} is the overall tension scale, so that it has almost no effect in normal tension configurations. We chose the feedback parameter $n = 4$ and the relaxation rate $\tau_p = \tau_T/4$, the same used in the single-quartet and single-triangle simulations.

So far, the time evolution of tensions is purely autonomous (i.e. each tension triangle is independent from all others) and completely analogous to the single-quartet simulation. In the single-quartet simulation, all tension triangles are equal by symmetry and periodicity, and thus tile the plane as a triangulation by construction. In general, this is no longer guaranteed. Even if one starts with a flat tension triangulation, the autonomous time evolution Eq. (S25) will result in a set of tension triangles that cannot fit together to a flat triangulation. The triangulation will develop curvature [12], i.e. “crumple” out of plane. This means that we have to add an additional ingredient to enforce triangulation planarity.

We enforce planarity as follows. The set of all balanced tension triangulations is parameterized by the dual vertex positions \mathbf{t}_i . We therefore seek the balanced tension configuration that approximates the intrinsic tensions as closely as possible by minimizing the following elastic energy:

$$E_{\text{tri}} = \frac{1}{2N_{\text{edges}}} \sum_{ij} (|\mathbf{t}_i - \mathbf{t}_j| - \tilde{T}_{ij})^2 + \frac{1}{2N_{\text{triangles}}} \sum_{ijk} \text{Pen}(A_{ijk}, A_0) \quad (\text{S26})$$

Since the simulation is based on half-edges, the per-edge intrinsic tension \tilde{T}_{ij} is the average of the

tensions of the two half-edges (which can be thought of as the two cellular cortices coupled in a cell-cell interface). The second term, $\text{Pen}(A, A_0)$ is a penalty term on the triangle areas A (calculated from the vertex positions \mathbf{t}_i). It fixes the overall tension scale (which is arbitrary due to force balance) and ensures the triangulation is well behaved numerically. It contains two terms:

$$\text{Pen}(A, A_0) = \gamma_{\text{tri}} \left(100 \cdot (\max\{0, \frac{A_0}{4} - A\})^2 + \frac{1}{2}(A - A_0)^2 \right) \quad (\text{S27})$$

Here, A_0 is an arbitrary reference area fixing the overall tension scale. Because the triangular mesh is oriented, the area A_{ijk} is signed, with negative signs corresponding to un-physical “flipped” configurations. These, and degenerate triangles, are penalized by the first term. The second term is a soft potential fixing the overall tension scale and preventing isotropic growth. The penalty strength γ was chosen at 10^{-3} , so that the area penalty represents a small correction to the length-term.

In the simulation, we first carry out an explicit Euler step for the intrinsic tensions, and then “flatten the triangulation”, i.e. find the dual vertex positions by minimizing Eq. (S26). This determines the extrinsic tensions $T_{ij} = \|\mathbf{t}_i - \mathbf{t}_j\|$. Finally, we relax the intrinsic tensions to force balance with rate τ_{balance} ,

$$\frac{d\tilde{T}_{ij}}{dt} = -\tau_{\text{balance}}^{-1}(\tilde{T}_{ij} - T_{ij}) \quad (\text{S28})$$

In order to ensure numerical stability even for large τ_T , we use the exact solution of Eq. (S28) numerically, instead of carrying out an explicit Euler step.

The triangulation-flattening prescription can be thought of as modelling, indirectly, known feedback loops which lead to a convergence to balanced tension, such as strain-rate feedback [13], which has been demonstrated experimentally [14]. The rate $\tau_{\text{balance}}^{-1}$ determines the speed of these feedback loops. The influence of the value of $\tau_{\text{balance}}^{-1}$ is studied in Fig. S8. In principle, strain rate feedback requires movement of cell vertices to sense tension imbalance and then bring tensions back to a balanced state. We neglect this vertex motion, since we assume balance is restored rapidly. Directly modelling of strain rate feedback requires going beyond the separation between tension- and real-space-dynamics that is the basis of our model here and is therefore beyond the scope of this paper. Further, the triangulation-flattening prescription is the most parsimonious generalization of the local tension feedback dynamics employed in the single-quartet simulation to a disordered tissue patch.

The complete tension dynamics that is implemented in the simulation therefore comprises three terms in addition to the dynamics shown in the main text Eq. (5): (1) Numerical cutoff of positive feedback at very high tensions (2) Passive tension dynamics post T1 (3) Relaxation of tensions to force equilibrium:

$$\partial_t \tilde{T}_{ij} = \tau_T^{-1} \left(\tilde{T}_{ij}^n - k_{\text{cutoff}} \tilde{T}_{ij}^{n+1} - \frac{1}{3} \sum_{\alpha \in I_{ijk}} (\tilde{T}_{\alpha}^n - k_{\text{cutoff}} \tilde{T}_{\alpha}^{n+1}) \right) \quad (\text{S29})$$

$$- \tau_p^{-1} T_{p,ij} - \tau_{\text{balance}}^{-1} (\tilde{T}_{ij} - T_{ij}) \quad (\text{S30})$$

We find that our simulations are robust to different choices of the tension dynamics parameters $\tau_p, \tau_{\text{balance}}, k_{\text{cutoff}}$, as demonstrated in Fig. S8. We can, for instance, decrease the balancing time by 40 \times without affecting the qualitative behavior.

Cell shape dynamics. Above, we have described the dynamics of the tension triangulation. After an Euler step to update the tensions has been taken, we calculate the real space cell tessellation (i.e. the positions of the cell vertices) by minimizing the cell-shape elastic energy while constraining the angles by the tension triangulation. In the case of a single quartet of identical cells, we could

explicitly parameterize the cell shape by interface lengths and angles, and optimize only with respect to the former. In the disordered case, it is more convenient to enforce the angle constraint via a (strong) energy penalty. It would also be possible to instead directly optimize the per-cell isogonal potentials Θ_i with respect to the Voronoi reference, obviating the need for a penalty.

The elastic energy to minimize therefore has two terms – the cell elastic energy Eq. (3) calculated from cell shape tensor S_C Eq. (S23) and reference shape S_0 , and the angle penalty, which corresponds to the cortical tension energy term:

$$E = \frac{1}{2N_{\text{edges}}} \sum_{ij} T_{ij} \bar{\ell} (1 - \hat{n}_{ij} \cdot \hat{\mathbf{r}}_{ij}) + \frac{\varepsilon}{N_{\text{cells}}} \sum_i E_{C,i} \quad (\text{S31})$$

Here, \hat{n}_{ij} is the unit normal of the tension edge, $\hat{\mathbf{r}}_{ij}$ the unit tangent vector of the primal edge, and $\bar{\ell}$ is the average interface length, to ensure the term has the correct dimensions of energy. The small parameter ε (we use $\varepsilon \sim 10^{-3} \lambda^{-1}$) represents the fact that the cell shape energy is assumed to be much weaker than the cortical tensions. If desired, one can replace or modify the cell shape elastic energy E_C in Eq. (S31) by another energy, e.g. the common area-perimeter elasticity.

In Eq. (S31), we use a different term than $T_{ij} \ell_{ij}$ to represent angle constraint due to cortical tensions. When determining the vertex positions \mathbf{r}_{ijk} , we minimize the cell shape elastic energy under the constraint of fixed angles, as given by the tension triangulation (so in a sense, we minimize the energy not with respect to the complete vertex positions, but with respect to the isogonal modes only). The tensions are externally imposed parameters and not functions of the vertex positions, like in a spring network. Eq. (S31) does not represent the physical energy, but merely the way we numerically enforce the angle constraints.

We use the alternative energy term $T_{ij}(1 - \hat{n}_{ij} \cdot \hat{\mathbf{r}}_{ij})$ for two numerical reasons. (1) compared to $T_{ij} \ell_{ij}$, it does not require a pressure term $p \sum_i A_i$ to avoid global constriction; otherwise, we would have to solve a discrete Poisson equation to determine p . (2) it avoids potential convergence issues when minimizing the elastic energies in the presence of very short junctions, which occur before and after T1-transitions. However, if the overall area is fixed, both forms of the energy lead to the same family of ground states, namely states where the vertex angles are complementary to those of the tension triangulation. The energy term $T_{ij}(1 - \hat{n}_{ij} \cdot \hat{\mathbf{r}}_{ij})$ was explicitly constructed to ensure this. Away from the ground state, the two energies differ; however, this is immaterial since we work in the regime where the tension constraints are always satisfied exactly.

We can also rewrite

$$T_{ij}(1 - \hat{n}_{ij} \cdot \hat{\mathbf{r}}_{ij}) = \frac{T_{ij}}{2} \|\hat{\mathbf{r}}_{ij} - \hat{n}_{ij}\|^2 = \frac{1}{2} \|\mathbf{T}_{ij} - R(\frac{\pi}{2}) \mathbf{t}_{ij}\|^2 \quad (\text{S32})$$

where \mathbf{T}_{ij} is the real-space tension vector, $R(\frac{\pi}{2})$ a 90° rotation matrix, and $\mathbf{t}_{ij} = \mathbf{t}_i - \mathbf{t}_j$ the dual tension vector, defined by the tension vertices. This shows that minimization of the $\sum_{ij} T_{ij}(1 - \hat{n}_{ij} \cdot \hat{\mathbf{r}}_{ij})$ energy enforces that the tensions in the cell array match those prescribed by the tension triangulation.

After carrying out a local Euler step and updating the dual vertex positions by “triangulation flattening”, we find the primal vertex positions by minimizing the elastic energy Eq. (S31).

Topological modifications. After each time-step we check whether any edge has collapsed. We call an edge collapsed if its length is $< 10\%$ of the overall length scale (mean edge length at simulation start). If this occurs, we carry out an intercalation (flip the corresponding edge in the triangulation) and set the active and passive tensions on the new edge as described above.

Edges that underwent a T1 transition in the last 20 simulation time steps (corresponding to 2.5 minutes) are excluded from edge collapse so as to prevent the immediate re-collapse of newly formed junctions. Instead of this hard-coded criterion, one could also calculate the strain rate of junctions of short length and exclude extending junctions, as shown by the time traces of junction length in Fig. 8B.

Automatic differentiation and numerical optimization. The simulation requires solving two optimization problems, one for the triangulation Eq. (S26) and one for the real-space shape Eq. (S31). To solve an optimization problem efficiently, it is crucial to know the gradient of the objective function. We use the python library JAX [76] to automatically differentiate our energy functions, allowing easy, rapid and bug-free calculation of the Jacobians. We further use JAX’s just-in-time functionality to accelerate our python code. Gradient-based optimization requires the objective function to be at least once differentiable. To ensure this, we mollify functions as required; for example, the Euclidean norm $\sqrt{x^2 + y^2} \rightarrow \sqrt{x^2 + y^2 + \varepsilon^2}$, $\varepsilon \sim 10^{-3}$ to ensure differentiability when computing the lengths of very short edges.

With these tools, the energies can be efficiently minimized using `scipy`’s conjugate-gradient optimizer. With a relative tolerance of 10^{-5} , a shape optimization step for ~ 1000 cells takes ~ 10 s on a laptop. Using the half-edge data structure described above, and JAX-based automatic differentiation, we can also easily construct the isogonal Hessian \mathcal{H}_{ij} analyzed in Fig. S13.

Creation of initial conditions. Finally, we need to specify the simulation the initial conditions. Note that because the cell vertex positions are computed from the tension triangulation, in our initial condition we specify only the tension triangulation.

We consider two types of initial conditions, using either a regular lattice or a random point process to choose the tension vertices. In the former case, we chose rectangular patches of a regular triangular lattice, with i.i.d. Gaussian noise added to the vertex positions. The amplitude of the noise was chosen so that $\text{std}(T_{ij}) = 0.1 \text{ mean}(T_{ij})$. The influence of the Gaussian noise standard deviation is shown in Fig. S8. A triangular lattice corresponds to a hexagonal lattice of cells. Indeed, locally, the *Drosophila* embryo at the onset of GBE looks like it is composed out of (noisy) hexagonal lattice patches, as shown in Fig. S1. This lattice is subjected to a small initial strain to create an a initial tension anisotropy, as described in the main text.

To investigate the effect of disorder, we also create initial conditions using a hard disk process. This randomly samples 2d-points (the eventual vertices in tension space) under the constraint that no two points are closer than $2r$ where r is the “hard disk” radius. Instead of r , we use the normalized hard disk packing fraction $\rho \in [0, 1]$, which is maximal for a hexagonal lattice. At $\rho \sim 0.72$, the hard disk process undergoes a phase transition that destroys the lattice order. The limit $\rho = 0$ corresponds to a Poisson point process. To sample from a hard disk point process, we use the event-chain Monte Carlo algorithm of Ref. [31], with code based on that provided with Ref. [32]. Note that with other algorithms such as sequential deposition or standard Monte Carlo it is either impossible or prohibitively slow to sample at arbitrary values of ρ .

To create a tension triangulation, we then compute the Delaunay triangulation of this point set (we further refine the initial condition by removing the edge of this tension triangulation, where the Delaunay algorithm can create very long tension edges). This triangulation is stretched uniformly to set up the initial anisotropy of tension. Cell numbers and initial aspect ratios were also chosen identically in the simulations that make up the phase diagram of Fig. 3.

Boundary conditions, tissue patterning, and isogonal stretching. For the first half of the work, Figs. 2-5, we use a tissue made of identical cells with free boundary conditions. We now specify the boundary conditions, and the division of the tissue into active and passive patches of the simulations for Figs 7-8.

We use appropriate boundary conditions to mimic the geometry of the *Drosophila* lateral ectoderm. We consider a initially rectangular tissue patch with height $>$ width. The top/bottom edges correspond to the dorsal pole, the middle to the ventral region, and the left/right sides to the anterior/posterior edges of the lateral ectoderm. To simulate the cylindrical geometry of the *Drosophila* trunk, the top/bottom boundary are given slip-wall boundary conditions, i.e. the cells on the boundary are pinned along the y -axis and free to move along the x -axis. The left/right boundaries are free. Boundary conditions are numerically implemented by a confining potential which penalizes deviation of the x or y coordinate of the cell centroids designated to be boundary

cells from the location of the slip wall. This allows for flexible implementation of various boundaries and geometries. We can also chose different boundary conditions. We can also add slip walls on the left/right boundaries to model the experiments carried out in Ref. [8], where GBE was blocked by cauterization of the ventral tissue close to the posterior pole.

Next, we designate active and passive regions in the tissue. In the active region, tensions evolve in time according to excitable tension feedback Eq. (S25). In the passive regions, tensions are governed by homeostasis (see below), and cells are softer. To simulate a wild type embryo, we chose the size of the passive patch to be approximately 40% of the embryo circumference (the exact value does not have an important influence). To mimic an embryo without modulation of activity along the DV axis (e.g. a *TollRM9* mutant), all cells along the embryo were taken to be active. The cells at the very tissue boundary are always passive for reasons of numerical stability. Otherwise edges on the boundary could undergo a T1, which leads to an invalid state.

We can take model a situation where the cells in simulated tissue are initially stretched isogonally. This can be encoded by stretching the tissue using the slip wall boundary conditions; instead, we set the cell reference shape S_0 to an anisotropic matrix, as discussed above in the SI. For the simulations of the Fig. 7 and 7, we set the initial stretching to 0.

Dynamics of tensions and cell shapes in passive cells. To model the cells in passive tissue regions in our simulations, we must prescribe their tension dynamics and their cell elasticity. Regarding the tension dynamics, we assume that it is governed by tension homeostasis. This means that the intrinsic tensions \tilde{T}_{ij} in the passive region behave as:

$$\frac{d\tilde{T}_{ij}}{dt} = -\tau_h^{-1}(\tilde{T}_{ij} - \tilde{T}_{ij,0}) \quad (\text{S33})$$

where τ_h is the homeostasis timescale, and $\tilde{T}_{ij,0}$ is the tension on the edge at the beginning of the simulation. For newly generated edges after a passive T1, we generate a random reference value $\tilde{T}_{ij,0} \approx 1$. One can also set $\tilde{T}_{ij,0} \equiv 1$ for all passive cells, in which case the passive tissue relaxes to a hexagonal lattice. The speed of homeostasis τ_h has no strong influence on the simulations, but must be large enough so that tensions relax after a passive T1 process, before a second passive T1 process takes place. In our simulations, we always set $\tau_h = \tau_p$, the speed of passive tension relaxation in the active tissue.

Regarding cell shape dynamics, we model the passive tissue as very soft. In particular, we assume that their shear modulus is very low: $\mu_p = 0.2\mu_a$, $\lambda_p = 0.2\lambda_a$ where the subscripts a and b refer to active and passive cells, respectively. Further, we use a lower value of the angle-constraint penalty $1/\varepsilon$ than in the active region: $1/\varepsilon_p = 1/(200\varepsilon_a) = 5$. This accounts for the fact that in the passive region, the elastic moduli are much lower (so $1/\varepsilon_p$ must be decreased to keep the ratio constant), as well as for the fact that in the passive region, we expect weaker tension. Tension is still the dominant force and the cell array angles match the angles prescribed by the triangulation to within $\sim 2^\circ$. However, we find that small deviations from the triangulation are important to facilitate passive T1s.

Simulation statistics and computing resources

For each measurement show in the figures of this paper, by default, we pooled or averaged 3 simulation runs with identical parameters, but different random seeds for the creation of the initial tension triangulation. The phase diagram Fig. 3A shows the average of 6 simulation runs each. The trajectories in Fig. 7 as well as the interface length and orientation statistics in Fig. 8 were computed from a single simulation.

Unless specified otherwise, we simulated cell arrays with $N_{\text{cells}} \approx 10^3$ cells (the exact number could vary slightly due to randomness in the hard disk point process). Simulations of saturating feedback

in Fig. 5 were performed with $N_{\text{cells}} \approx 350$ cells, and simulations in Figs. 7-8 had $N_{\text{cells}} \approx 750$ cells. Simulation edges were always excluded from analysis. For the single-triangle simulation in Fig. 5, we simulated 4×10^3 individual triangles from the initial condition of the full numerical simulations. When showing time traces, we smoothed the T1-rate and aspect ratio time series with a Gaussian kernel of width $10dt$ where $dt = \tau_T/200$ is the simulation time step. Numerical parameters were adjusted so that elastic energy minimization and triangulation flattening converged for all simulations and all time points.

Simulations were carried out on a Supermicro workstation with 64 Intel Xeon Gold 6326 cores and 256GB of RAM. However, individual simulations (rather than parameter scans and phase diagrams) can be run without problem on a consumer grade laptop.

Model parameters and their effects

As a summary, Table I gives a list of all the parameters of the tissue-scale model displayed in this work, as well as their default values. Fig. S8 shows analyses of simulations where several of the parameters are varied, confirming that the qualitative behavior of the model is largely independent of the exact parameter values.

Model parameter	Symbol	Default value	Parameter effect, comments
Tension time scale	τ_T	25 min	Fitted to experimental T1 tension dynamics.
Feedback exponent	n	4	Must be > 0 to produce flow. Weak effect on net CE.
Tension balancing	τ_{balance}	$\tau_T/200$	Must be $\ll \tau_T$. Higher values lead to a higher rate of disoriented T1s.
Passive tension relaxation	τ_p	$\tau_T/6$	No strong effect. Must be sufficiently small $< \tau_T/2$ to create irreversible T1s.
Elasticity coefficients	$\lambda, \mu, \lambda_a, \mu_a$	1	No strong effect. Must be > 0
Passive region shear moduli	μ_p, λ_p	0.2	Higher shear resistance of passive tissue lowers net amount of CE.
Initial condition parameters			
Average tension	\bar{T}	1	
Average edge length	ℓ_0	$1/\sqrt{3}$	Set to match the Voronoi dual of the tension triangulation
Initial anisotropy	$ \langle\sqrt{2}\tilde{Q}\rangle $	0.2	Higher values increase net CE.
Tension vertex hard disk packing fraction	ρ	$0.45 - 0.9$	Higher values increase net CE.
Gaussian noise in initial tensions (standard deviation)		$0.1 \bar{T}$	Weak effect on net CE, as long as noise is sufficiently weak to not affect triangulation topology.
Cell reference shape	S_0	$3\ell_0 \mathbb{I}$	Anisotropic S_0 increases bridge bias by shifting T1 threshold.
Number of cells	N_{cells}	$\approx 10^3$	Number can vary due to random sampling. For “germ band” simulations we used $N_{\text{cells}} = 750$.
Numerical parameters			
Tension feedback cutoff	k_{cutoff}	$0.3\bar{T}$	
Triangulation area penalty	γ_{tri}	0.01	
Angle constraint penalty	$1/\varepsilon$	10^3	In the passive region, we use $1/\varepsilon = 5$ to account for the reduced cortical tensions there.
Boundary condition penalty		5×10^3	
Time step	dt	$5 \times 10^{-3} \tau_T$	
Edge length to trigger collapse		$0.1 \ell_0$	

TABLE I. Parameters of tissue scale simulation. A value in the second-to-last column indicates a “default” value which was used in all simulations except otherwise indicated. \bar{T} is the overall tension scale (average edge tension at initial condition), and ℓ_0 the overall length scale (average edge length at initial condition). Net CE denotes the amount of convergent extension as tissue flow saturates.

5. MOVIE CAPTIONS

Movie 1: Tissue shape change by dynamics tension constraints. Implementation of our model for a symmetric, regular cell array, characterized by one angle ϕ , determined by the tensions T_0, T_1 , and two lengths, ℓ_0 and ℓ_1 , parametrizing the soft isogonal modes. The contour plot shows the cell shape energy E_C in the incompressible limit where ℓ_1 is determined uniquely by ℓ_0 and ϕ . Relaxation of the sub-dominant cell shape energy E_C is constrained to the isogonal subspace (white line) determined by tension force balance. For the critical tension ratio $T_0/T_1 = \sqrt{2}$, constraining the angle to $\phi_c = \pi/2$ (black dashed line), the interface length minimizing E_C vanishes (red half-disk).

Movie 2: Simulations comparing ordered and disordered initial cell packings. The total extend of tissue shape change depends on the initial degree of order in the cell packing (cf. Fig. 2). Starting from an hexagonal packing, cell rearrangements are initially well-coordinated leading to coherent tissue flow. As order is lost, tissue flow stalls. The number of cells and the initial tension anisotropy, as well as all other parameters, are the same for both simulations. The simulations were carried out with free boundary conditions. Top row shows the cell arrays, colored by cell coordination number (hexagons=white), bottom row the underlying tension triangulation.

Movie 3: Simulations comparing saturating and winner-takes-all tension feedback. Comparison of saturating (left) and winner-takes-all (right) tension feedback (cf. Fig. 5). Both simulations were initialized identical initial conditions (an ordered cell array with 20% tension anisotropy). All other parameters are the same for both simulations. Top row shows the cell arrays, colored by cell coordination number (hexagons=white), bottom row the underlying tension triangulation. Saturating feedback leads to little large scale shape change and creates tension cables.

Movie 4: Simulation combining active and passive tissue regions. The embryo is modeled by a rectangular tissue patch with slip walls on the top and bottom edge, mimicking the embryo's cylindrical geometry (cf. Fig. 7). The active and passive tissue regions, indicated by color and shading of the edges (color/solid=active), correspond to the germ band and the amnioserosa, respectively. Left: Cell tessellation with black dots indicating the cells along the slip wall (restricted to move along horizontally along the “AP axis”). Right: underlying tension triangulation. The tension triangulation is initialized with the experimentally observed initial tension anisotropy which breaks rotational symmetry and aligns the tissue extension along the “AP axis”. Colored dots follow a selected subset cells to highlight rearrangements.

Movie 5: Simulation of convergent extension without cell rigidity and without DV modulation of activity. Simulation of tissue scale model of convergent extension in an embryo-like geometry for a control and two “mutant” configurations, corresponding Fig. 8. Left: “Control”, as in Movie 3. Middle: Active tissue with vanishing shear modulus $\mu_a = 0$. Right: No DV modulation, i.e. no soft, passive region. All other parameters are identical. Top shows cell array, bottom underlying tension triangulation. Active and passive tissue regions are indicated by color and shading of the edges (color/solid=active). In all three conditions, active T1s drive elongation of the tension triangulation, while the convergent extension of the cell array only occurs for the “control” condition.